2012

Formulation and Solution of Electromagnetic Integral Equations Using Constraint-Based Helmholtz Decompositions

Jin Cheng
University of Kentucky, jincheng_ivy@yahoo.com.cn

STUDENT AGREEMENT:

I represent that my thesis or dissertation and abstract are my original work. Proper attribution has been given to all outside sources. I understand that I am solely responsible for obtaining any needed copyright permissions. I have obtained and attached hereto needed written permission statements(s) from the owner(s) of each third-party copyrighted matter to be included in my work, allowing electronic distribution (if such use is not permitted by the fair use doctrine).

I hereby grant to The University of Kentucky and its agents the non-exclusive license to archive and make accessible my work in whole or in part in all forms of media, now or hereafter known. I agree that the document mentioned above may be made available immediately for worldwide access unless a preapproved embargo applies.

I retain all other ownership rights to the copyright of my work. I also retain the right to use in future works (such as articles or books) all or part of my work. I understand that I am free to register the copyright to my work.

REVIEW, APPROVAL AND ACCEPTANCE

The document mentioned above has been reviewed and accepted by the student's advisor, on behalf of the advisory committee, and by the Director of Graduate Studies (DGS), on behalf of the program; we verify that this is the final, approved version of the student's dissertation including all changes required by the advisory committee. The undersigned agree to abide by the statements above.

Jin Cheng, Student

Dr. Robert J. Adams, Major Professor

Dr. Zhi Chen, Director of Graduate Studies

FORMULATION AND SOLUTION OF ELECTROMAGNETIC INTEGRAL EQUATIONS USING CONSTRAINT-BASED HELMHOLTZ DECOMPOSITIONS

DISSERTATION

A dissertation submitted in partial fulfillment of the
requirements for the degree of Doctor of Philosophy in the
College of Engineering
at the University of Kentucky

By
Jin Cheng
Lexington, Kentucky

Director: Dr. Robert J. Adams, Associate Professor of
Electrical and Computer Engineering
Lexington, Kentucky

2012

ABSTRACT OF DISSERTATION

FORMULATION AND SOLUTION OF ELECTROMAGNETIC INTEGRAL EQUATIONS USING CONSTRAINT-BASED HELMHOLTZ DECOMPOSITIONS

This dissertation develops surface integral equations using constraint-based Helmholtz decompositions for electromagnetic modeling. This new approach is applied to the electric field integral equation (EFIE), and it incorporates a Helmholtz decomposition (HD) of the current. For this reason, the new formulation is referred to as the EFIE-hd. The HD of the current is accomplished herein via appropriate surface integral constraints, and leads to a stable linear system. This strategy provides accurate solutions for the electric and magnetic fields at both high and low frequencies, it allows for the use of a locally corrected Nyström (LCN) discretization method for the resulting formulation, it is compatible with the local global solution framework, and it can be used with non-conformal meshes.

To address large-scale and complex electromagnetic problems, an overlapped localizing local-global (OL-LOGOS) factorization is used to factorize the system matrix obtained from an LCN discretization of the augmented EFIE (AEFIE). The OL-LOGOS algorithm provides good asymptotic performance and error control when used with the AEFIE. This application is used to demonstrate the importance of using a well-conditioned formulation to obtain efficient performance from the factorization algorithm.

KEYWORDS: Helmholtz decomposition, electric field integral equation, low-frequency, Nyström, local-global solution

Jin Cheng

Student's Signature

Dec 5, 2012

Date

FORMULATION AND SOLUTION OF ELECTROMAGNETIC INTEGRAL EQUATIONS USING CONSTRAINT-BASED HELMHOLTZ DECOMPOSITIONS

By

Jin Cheng

Robert J. Adams

Director of Dissertation

Zhi Chen

Director of Graduate Studies

Dec 5, 2012

ACKNOWLEDGEMENT

The journey of pursuing PhD degree as a graduate student is challenging yet rewarding. On this special journey, I am indebted to many people for their generous help and support.

First of all, I am deeply grateful to my advisor Dr. Robert J. Adams. He has been quite supportive not only by providing me a research assistantship over the past six and half years, but also guiding me through the whole process of research academically. I am so impressed by his enthusiasm in research and ability to come up with fascinating new ideas. He is quite energetic and active, which also positively influenced me a lot. Thanks to him, I had the opportunity to contribute to the development of the EFIE-hd formulation, which is challenging but exciting.

Furthermore, I am very thankful to Dr. Stephen D. Gedney, Dr. William T. Smith, Dr. Qiang Ye and Dr. Grzegorz W. Wasilkowski for their time serving on my committee. What's more, I have benefited greatly through their teachings on a variety of courses, such as CEM, EM, linear algebra and numerical analysis.

I would like to thank Dr. Gedney again. Through two years of taking his CEM courses, my coding skill was gradually built up as well as my knowledge in CEM. But the most rewarding part was the project reports. He corrected them line by line, from grammar errors to technique errors, as well as pointing out the merits, which not only helped me accumulating knowledge and ability, but also served as a source of encouragement and energy.

I would like to express my thanks to Dr. John C. Young. He has been very helpful in providing advice on the Nyström method and augmented formulations.

I have to thank my master advisor Dr. Zhenghui Xue. I have taken his class in Introduction to Microwave Circuits when I was a junior at college. He made the learning very fun and inspired me greatly. After that, I have decided to pursue my master degree on the direction of electromagnetics. As my master advisor, he gave me a lot of guidance and support, as well as encouraged me to study abroad.

I would like to give my special thanks to my colleagues at UK. They are Dr. Xin Xu, Dr. Yuan Xu, Dr. Zhiyong Zeng, Dr. Chong Luo, Mr. Xiande Cao and Mr. Jun Shik Choi. Through the countless discussions on the research with them, I have benefited greatly. Dr. Xin Xu has provided me tremendous help during my time at UK. He is always there to answer my questions and gives me insightful suggestions. He is also a very kind friend to me. Dr. Yuan Xu also gave me many helpful guidance and suggestions on my research and generously allowed me to use his codes.

I must thank my friends for their kind support and encouragement. Wen Zhang and Zhiyin Jia are my best friends since childhood with whom I share my joy and pain. Whatever I am, they are always there to listen to me, comfort me and encourage me. My college roommate and good friend, Mona Chang is always honest and frank to point out my weak points, and she is a quite hard working and determined person. Through my relation with her, I have got precious experiences, perseverance in work and patience to overcome difficulties. It was a happy memory of having a road trip with her driving from Kentucky down to Florida in the summer of 2009. It was full of fun and uncountable meaningful conversations. Jennifer Edwards is a good friend and big sister to me. In front of her, I always feel very comfortable and free to express myself. She has a good taste in decorating and always gives me pleasant surprises in making delicious dessert and

beverages. Christy Brown is a very kind and graceful lady. I knew her when we both volunteered in Ronald McDonald Family Room. Around that time, probably from 2009 to 2010, I was filled with home sickness, uncertainty about the future and anxiety about my graduate study. She cared about me so much. She took me to a nice restaurant, or sent me beautiful cards with caring and encouraging words. She is a great source of energy for me to overcome the difficulties.

My Chinese friends in Lexington are very important to me too. We are far away from family, but we are family to each other here. I will always cherish the memories we spent time together.

Finally but most importantly, I would like to thank my whole family, especially my maternal grandmother, maternal grandfather, mom and stepfather for their unconditional love and constant support. Without you, I cannot accomplish this. You all are always a source of love and energy to me.

Table of Contents

List of Tables

List of Figures

Chapter 1 Introduction

1.1 Motivation

The development of fast and efficient full-wave solution methods for large, linear, time-harmonic electromagnetic problems requires two basic elements. One is stable, well-posed formulations that, upon discretization, provide controllably accurate solutions under a variety of conditions. Another requirement is a strategy for solving the resulting linear system in a manner that scales efficiently as the number of degrees of freedom (DOF) is increased.

In the following, we will consider primarily a surface integral equation (SIE) approach to the aforementioned problem. The SIE method is widely used for modeling electromagnetic field interactions with perfect conductors. The most appealing feature of the SIE is that it allows the underlying problem to be represented by meshing only the surfaces of the conductors. This reduces number of DOF compared to methods based on either volume integral equations or methods that rely on a partial differential equation.

There are two basic SIE representations for a conductor, the electric field integral equation (EFIE) and the magnetic field integral equation (MFIE). The EFIE provides accurate solutions for both open structures and structures with geometric singularities. However, it will break down at low frequency or with electrically small structures [1]. The MFIE is better conditioned than the EFIE, but it can be used only for closed geometries, and it is less accurate compared to the EFIE for geometric singularities [2]. However, the MFIE is still indispensable to form the combined field integral equation (CFIE) which is used to suppress interior spurious resonance [3]. In this work, surface integral equations using constraint-based Helmholtz decompositions (HD) are proposed

to resolve the low frequency breakdown problem of the EFIE. The new formulation is referred to as the EFIE-hd, because it relies on a Helmholtz decomposition (HD) of the current. As will be shown later, the EFIE-hd is frequency stable yet provides accurate solutions for the electric and magnetic fields at both high and low frequencies.

To address large-scale and complex electromagnetic problems using an integral equation based (IE-based) method, sparse iterative or direct solution methods are imperative. In this work, a sparse direct solution method based on the local-global solution (LOGOS) framework [4, 5] is used to factorize the resulting system matrix. It has been observed that it can provide efficient factorizations for several practical formulations. For electrically small objects, the complexity of the corresponding factorization has been found to range between approximately $O(N)$ and $O(N \log N)$ when N was increased via mesh refinement.

In this work, the locally corrected Nyström method (LCN) [6-9] is employed to discretize the EFIE-hd formulation. The LCN method is a point-based high-order method. This method has some advantages over Galerkin schemes. Only a single integration is required for evaluate near interactions, and single-point kernel evaluation suffice for the far interaction.

In summary, the purpose of this dissertation is to develop surface integral equations using constraint-based Helmholtz decompositions for electromagnetic modeling. This strategy provides accurate solutions for the electric and magnetic fields at both high and low frequencies, it allows for the use of the LCN discretization method for the resulting formulation, it is compatible with the LOGOS framework, and it can be used

with non-conformal meshes. To the best of our knowledge, no SIE-based approach to electromagnetic modeling provides these capabilities.

1.2 Review

In this section, various formulations aimed at addressing the low frequency breakdown problem of the EFIE are briefly reviewed. Iterative and direct solution methods are also reviewed.

1.2.1 The formulation

A well-known limitation of the EFIE is the fact that the formulation breaks down at low frequencies or with electrically small structures [1]. This breakdown occurs because the scalar potential contribution to the tangential electric field overwhelms the contribution from the vector potential at low frequencies or with electrically small structures during the numerical process. The scalar potential term has null space due to the divergence operator. It yields a poorly conditioned linear system when the EFIE is discretized at low frequencies. This issue will be further examined in Chapter 3.

A number of strategies have been developed to address this low frequency breakdown. These include approaches that rely on an approximate Helmholtz decomposition (HD) of the vector bases used to represent the current [1, 10, 11], approaches that rely on the self-stabilization properties of the EFIE integro-differential operator [12-14], and methods that introduce charge as an additional unknown [15-17].

While the aforementioned strategies are effective in many cases, they introduce additional complexities that make their application difficult in some circumstances. For example, if one is interested in using the (LCN) method to discretize the continuous formulation, then the use of methods that decompose the surface current into solenoidal

and nonsolenoidal spaces are not straightforward. It is similarly difficult to obtain an efficient LCN discretization of formulations that utilize the self-stabilization properties of the EFIE. Furthermore, both approaches (decomposed vector bases and self-stabilizing formulations) introduce an additional degree of non-locality into the problem formulation. In the former case, this can occur through the presence of global loops; in the latter case one encounters a product of integral operators. Both of these scenarios complicate the application of sparse solution methods that are based on the localization of the degree of freedom (DOF) in the problem (e.g., LOGOS solution framework).

Augmented formulations [15-17] avoid both of these limitations. They are amenable to both LCN discretization and localization-based factorizations [18, 19]. Unfortunately, formulations such as [18] are difficult to effectively extend for the case of non-PEC materials. This is related to the fact that the augmented formulation of [18] can yield incorrect results for the magnetic fields scattered from conducting bodies at low frequencies. These methods also fail when applied to non-conformal meshes.

The new formulation considered herein uses a constraint-based Helmholtz decomposition to overcome the limitations of these approaches.

1.2.2 The solution method

In the frequency domain, many simulation problems in electromagnetic analysis involve solving linear matrix equations of the form

$$\mathbf{Z}\mathbf{x} = \mathbf{F}^i, \tag{1.1}$$

where the matrix $\mathbf{Z}$ is referred to as the $N \times N$ system matrix. The vector $\mathbf{x}$ contains either the unknown field or current coefficients and $\mathbf{F}^i$ contains spatial samples of an impressed or incident source. The system indicated by (1.1) can be either obtained by

PDE based approaches or integral equation based (IE-based) methods [3]. In this dissertation we limit our attention to the surface integral equation (SIE) method. In this case, the system matrix $\mathbf{Z}$ is dense. Standard direct methods for solving the above linear equations have $O\left(N^3\right)$ CPU time complexity and $O\left(N^2\right)$ memory complexity. These costs are usually prohibitive for practical applications involving a large number of unknowns. Typically, such problems are solved either by sparse and fast iterative solution methods or sparse direct solution methods. One such representative iterative solver is the Fast Multipole Method (FMM) [20]. The FMM has been used to dramatically reduce the CPU complexity and the memory complexity associated with SIE methods. More recently, fast, direct solution methods have been investigated for IE based system matrices. Generally, the fast, direct solution strategy consists of developing efficient procedures for directly factoring one or more of the various compressed representations of the IE system matrix. The compressed representation of the system matrix used herein is based on an algebraic variant of the low-frequency version of the FMM.

1.3 Research Outline

Chapter 2 presents the LCN method, which is used to discretize the surface integral equation formulations. First, the conventional Nyström method is introduced. Next the LCN method is discussed in detail. The local correction of the LCN facilitates the treatment of the singular kernels that arise in electromagnetic operators. In addition, two sets of basis functions, polynomial complete basis functions and mixed-order basis functions are discussed and compared.

Chapter 3 provides the fundamental materials required in the development of the new formulation, which includes the derivation of the surface integral equations (SIE).

The LCN discretization of the SIE kernels is also discussed, especially focusing on the special treatment of the near interactions. Furthermore, the low frequency breakdown of the EFIE is analyzed comprehensively.

Chapter 4 provides the detailed derivation of the new EFIE-hd formulation, which is based on the electric field integral equation and incorporates a Helmholtz decomposition of the current. Several essential features are discussed, such as the Helmholtz decomposition of the current and the zero divergence constraints. The EFIE-hd formulation is first formulated for closed PEC geometries. The extension to open structures is also considered. Initial numerical examples are provided, and it is observed that the initial version of the EIFE-hd provides accurate solution at moderate frequencies. However the system still fails at low frequencies. This limitation is finally overcome through the inclusion of an additional constraint on the divergence of the EFIE and an appropriate, physically meaningful, scaling of the irrotational component of the current.

Chapter 5 considers a fast, direct numerical analysis method using overlapped localizing LOGOS modes for solving electromagnetic problems at low frequencies. The formulations used are the augmented EFIE (AEFIE) and augmented EIFE-G (AEFIE-G) formulations. These overcome the low-frequency breakdown inherent in the conventional EFIE through the use of the current continuity equation. Then the overlapping localized LOGOS (OL-LOGOS) framework is reviewed. The extension of the OL-LOGOS to an over-determined system obtained from the AEFIE and AEFIE-G formulation is presented and numerical results are provided [1][19].

[1] The application of the OL-LOGOS factorization to the EFIE-hd formulation is not considered in this dissertation. The work on the application of the OL-LOGOS factorization to the AEFIE and AEFIE-G is included to demonstrate the importance of using a well-conditioned formulation to obtain efficient performance from the factorization algorithm. Similar work using the EFIE-hd formulation will be considered elsewhere.

Chapter 6 concludes the work developed in this dissertation and identifies the future research directions based on this work.

Chapter 2 The Locally Corrected Nyström Method

The locally corrected Nyström (LCN) method [6-9] is a point-based high-order method, which is used to obtain numerical solutions of integral equations. Compared to low-order methods [21] (such as the method of moments (MoM) employing low-order basis and testing functions with Galerkin formulation), a high-order method has the ability to obtain high-order convergence rates with relatively small additional effort as well as control the rate of convergence.

The matrix fill of a high-order MoM (HO-MOM) with Galerkin formulation is time consuming, since it requires N^2 numerical double integrations, where N is the number of unknowns. Thus the LCN has a distinct advantage over HO-MOM with Galerkin formulation in that just a single kernel evaluation is required to fill most matrix elements (far interactions) and only $O(N)$ single integrations and some low-rank linear algebra to fill the other (near) interactions [7].

The conventional Nyström method is designed to handle regular kernels. Thus it cannot be used directly for integral equations with singular kernels such as those that arisie in electromagnetic analysis. In such situations, the high-order convergence advantage of the Nyström method is lost. Fortunately, by incorporating local correction in conventional Nyström method, the LCN [7] technique overcomes the problems associated with singular kernels. The essence of the local correction is to use specialized quadrature rules of the form introduced by Strain [22] to integrate the singular kernel to high order.

The remainder of this chapter is organized as follows. In Section 2.1, the conventional Nyström method is presented and followed by a discussion of the

differences with MoM. The LCN formulation is described in detail in Section 2.2, the connection between the LCN and a high-order method of moments (HO-MoM) solution with point-based discretization is also briefly introduced. Then Section 2.3 discusses basis functions and discretization required by local correction. Finally, Section 2.4 summarizes this chapter. The formulation and notation used in the follow introduction of the LCN method closely follows that used elsewhere [6, 8].

2.1 The Conventional Nyström Method

The basic idea of the Nyström method is that the problem domain (the surface of a perfect electric conductor (PEC) in this dissertation) is discretized into N patches, and the integral operator is replaced with a suitable quadrature rule (such as the Gauss-Legendre quadrature rules) over each patch [9]. The unknown quantity, which is usually the surface current density, is represented by its samples at the abscissa points of the underlying quadrature rule. The integral equation is then enforced at the same abscissa points, yielding a square linear system of equations. The solutions of this system are the samples of the current density. Consider the integral equation used to solve for a surface current density $J(\mathbf{r}')$ [6, 7],

$$\phi^i(\mathbf{r}) = \int_S K(\mathbf{r},\mathbf{r}')\, J(\mathbf{r}')\, ds', \tag{2.1}$$

where S represented a smooth surface, $\phi^i(\mathbf{r})$ is the known forcing vector evaluated at $\mathbf{r}$ on S, and $K(\mathbf{r},\mathbf{r}')$ is the kernel of the integral. The surface S is discretized into N_p curvilinear patches that represent the underlying surface to HO. Then the integral operator is replaced with a suitable quadrature rule. The right hand side (RHS) is also

sampled at the abscissa points, yielding a square linear system of equations, with the q_m^{th} row defined as

$$\phi^i\left(\mathbf{r}_{q_m}\right) = \sum_{p=1}^{N_P}\sum_{q=1}^{N_q} \omega_{q_p} K\left(\mathbf{r}_{q_m}, \mathbf{r}_{q_p}\right) J\left(\mathbf{r}_{q_p}\right), \tag{2.2}$$

where $\mathbf{r}_{q_p}$ and ω_{q_p} are the abscissas and weights on the p^{th} patch (source patch), and $\mathbf{r}_{q_m}$ is an abscissa point on the m^{th} patch (field patch). If $K\left(\mathbf{r},\mathbf{r}'\right)$ is regular and a high-order quadrature rule is used, then (2.2) will yield a high order approximation to the exact solution. However, most kernels arising in electromagnetic analysis are singular at vanishing distance between source point and field point, thus $K\left(\mathbf{r},\mathbf{r}'\right)$ is undefined when field point coincides with the source point ($\mathbf{r}=\mathbf{r}'$). To handle singular kernels, local corrections can be used. This procedure is described in detail in the next section.

It is useful to compare the well-known MoM approach with the Nyström method in terms of the meaning of the unknowns, the complexity of the respective procedures, and their computational costs [9]. First, the meanings of the unknowns of the two methods are different. In the MoM approach, the integral equation is discretized into a finite set of linear equations with finite number of unknowns. This is accomplished by first representing the surface current density as an expansion in a set of basis functions, and then taking the inner product of the integral equation with each member of a set of testing functions. The unknown coefficients of the expansion basis are finally determined by a numerical procedure such as matrix inversion and multiplication with the RHS. Once the unknown coefficients are solved, the surface current density at any point of the surface can be computed via the basis function expansion.

In contrast, for the Nyström method, the unknowns are the surface current density sampled at abscissa points of the underlying quadrature rule. In Section 2.2, it is demonstrated that a change of basis [6] can be used to connect the unknown of the MoM approach and the unknown of the Nyström method. Second, the Nyström method is simpler than the MoM method in implementation. There are two ways to improve the accuracy of either approach. The first is to refine the meshes (h-refinement), and the second is to use better representation of the surface current (p-refinement). To accomplish the p-refinement of the MoM approach, higher degree polynomials are used as basis functions, since surface current density is explicitly expanded by a set of basis functions, thereby increasing the computational amount for each entry of the system matrix. In the Nyström method, the accuracy of the representation of current is determined by the choice of the underlying quadrature rule. Therefore the p-refinement is realized by using a quadrature rule with more points, which does not change the computation amount for each entry of the system matrix. Third, as pointed earlier in this chapter, the MoM is more time consuming than the Nyström method during the matrix fill phase.

2.2 The Locally Corrected Nyström Method

The strategy of the LCN method to handle singular kernels is to use local corrections for the near interactions (in the vicinity of the kernel singularity), which employs the specialized quadrature rule to effectively corrects the underlying quadrature rule to integrate the singular kernel to high order. For far interactions where the kernel is smooth, the conventional Nyström indicated in (2.2) is used. The local corrections indicate that the “correction domain” is local to the field point. Therefore the LCN

method can be formulated for the same problem mentioned in section 2.1 but with singular kernel as [6]

$$\phi^i\left(\mathbf{r}_{q_m}\right)=\sum_{p\in far}\sum_{q=1}^{N_q}\omega_{q_p}K\left(\mathbf{r}_{q_m},\mathbf{r}_{q_p}\right)J\left(\mathbf{r}_{q_p}\right)+\sum_{p\in near}\sum_{q=1}^{N_q}\tilde{\omega}_{q_p(m)}J\left(\mathbf{r}_{q_p}\right), \tag{2.3}$$

where the notations were already illustrated in (2.2) except for $\tilde{\omega}_{q_p(m)}$, which are the weights of the specialized local quadrature rule for the singularity at $\mathbf{r}_{q_m}$. Note also that the abscissa points of the specialized quadrature rule are chosen to be the same as the underlying quadrature rule used to discretize the far interaction.

The procedure of determining $\tilde{\omega}_{q_p(m)}$ is provided below [6]. The weights $\tilde{\omega}_{q_p(m)}$ are obtained by placing a set of regular basis functions $F_k\left(\mathbf{r}\right)$ over the p^{th} patch, which typically are representative of those defining the underlying quadrature rule and then equating the quadrature rule to the moments,

$$\sum_{q=1}^{N_q}\tilde{\omega}_{q_p(m)}F_k\left(\mathbf{r}_{q_p}\right)=\int_{S_p}K\left(\mathbf{r}_{q_m},\mathbf{r}'\right)F_k\left(\mathbf{r}'\right)ds'. \tag{2.4}$$

Forcing this equality for $k=1,N_q$ yields the linear system of equations

$$\mathbf{L}_p\boldsymbol{\omega}=\boldsymbol{\kappa}_{q_m}, \tag{2.5}$$

where $\mathbf{L}_p$ is a matrix local to the p^{th} patch with entries $\left(\mathbf{L}_p\right)_{k,j}=F_k\left(\mathbf{r}_{j_p}\right)$, and the k^{th} element of vector $\boldsymbol{\kappa}_{q_m}$ is the right hand side of (2.4), which can be evaluated to desired precision using adaptive quadrature. The local quadrature weights $\tilde{\omega}_{q_p(m)}$ are the elements of the vector $\boldsymbol{\omega}$, which can be calculated from (2.5). By generating $\tilde{\omega}_{q_p(m)}$ in this fashion, the second part of the right hand side of (2.3) should produce the accurate near field for

any current density as long as that can be approximately well enough by the basis function expansion, which is denoted as $F_k(\mathbf{r})$ [9]. As we recall from the conventional Nyström method described in Section 2.1, the accuracy of the representation of current is determined by the choice of the underlying quadrature rule. Unlike the MoM method, the representation of the current in Nyström scheme is implicit, since it is not explicitly expressed in terms of a set of basis functions. However, the local correction requires a set of basis functions suitable for representing the current density, which suggests that the approximations in the generation of $\tilde{\omega}_{q_p(m)}$ are equivalent to the use of an explicit representation of the current density in terms of basis functions, thus the accuracy of the current approximation is limited to the degrees of freedom within the basis functions.

The procedure indicated by (2.3) to (2.5) yields a square matrix to solve for the current at the sampling points of the underlying quadrature rule. The contribution to the $q_m{}^{th}$ row from patches that are far enough from $\mathbf{r}_{q_m}$ is written in the operator form as

$$\mathbf{Z}_{q_m}^{far} = \left(\mathbf{k}_{q_m}\right)^T, \tag{2.6}$$

where superscript T indicates the transpose. The $q_p{}^{th}$ term of the row vector $\left(\mathbf{k}_{q_m}\right)^T$ is $\omega_{q_p} K\left(\mathbf{r}_{q_m}, \mathbf{r}_{q_p}\right)$. The contribution to the $q_m{}^{th}$ row from the near interaction can be written as the row vector,

$$\mathbf{Z}_{q_m}^{near} = \left[\left(\mathbf{L}_p\right)^{-1} \boldsymbol{\kappa}_{q_m}\right]^T. \tag{2.7}$$

It has been demonstrated in [6] that through a change of basis procedure, the HO-MOM with point-based discretization [23] can be projected into a form identical to that derived via the LCN scheme. Now consider again the integral equation in (2.1). Via the MoM

procedure, the surface current density $\mathbf{J}(\mathbf{r})$ is approximated over each patch by a basis function expansion,

$$J(\mathbf{r}) \approx \sum_{k=1}^{N_k} b_{k_p} F_k(\mathbf{r}), \tag{2.8}$$

where b_{k_p} are constant coefficients for the basis function expansion and $F_k(\mathbf{r})$ represent a set of smooth basis functions placed over the p^{th} patch that is complete to order N_k. The detailed derivation of this point-based HO-MoM is reported in [6, 23]. The final form is expressed as

$$\phi^i(\mathbf{r}_{q_m}) = \sum_{p=1}^{N_P} \sum_{k=1}^{N_k} b_{k_p} \int_{S_p} K(\mathbf{r}_{q_m}, \mathbf{r}') F_k(\mathbf{r}') ds', \tag{2.9}$$

where $\mathbf{r}_{q_m}$ is a quadrature abscissa point on the m^{th} patch (filed patch). The expression indicated by (2.9) looks like a MoM formulation with point matching. It is actually derived via an expansion of smooth test functions complete to order N_k. In the regions which are sufficiently far from the field point, the outer integral in (2.9) can be evaluated to HO via a fixed point quadrature rule. Then the contribution to the q_m^{th} row from patches that are sufficiently far from r_{q_m} is written as

$$\sum_{p \in far} \sum_{k=1}^{N_k} b_{k_p} \left[\sum_{q=1}^{N_k} \omega_{q_p} K(\mathbf{r}_{q_m}, \mathbf{r}_{q_p}) F_k(\mathbf{r}_{q_p}) \right], \tag{2.10}$$

where $\mathbf{r}_{q_p}$ and ω_{q_p} are the abscissa points and the weights of the $N_k -$ point quadrature rule, respectively. Equation (2.10) is written in the operator form as

$$\left(\mathbf{L}_p \mathbf{k}_{q_m}\right)^T \mathbf{b} = \left(\mathbf{k}_{q_m}\right)^T \left(\mathbf{L}_p\right)^T \mathbf{b}, \tag{2.11}$$

where the matrix $\mathbf{L}_p$ is defined in (2.4) and (2.5), the vector $\mathbf{k}_{q_m}$ is defined in (2.6), and the vector $\mathbf{b}$ contains coefficients of the basis functions indicated in (2.8). $J\left(\mathbf{r}_{q_p}\right)$ denotes the current density at the abscissa point $\mathbf{r}_{q_p}$. From the expansion in (2.8), $J\left(\mathbf{r}_{q_p}\right)$ is expressed as

$$J\left(\mathbf{r}_{q_p}\right) \approx \sum_{k=1}^{N_k} b_{k_p} F_k\left(\mathbf{r}_{q_p}\right). \tag{2.12}$$

Therefore the samples of the current density at the abscissa points of the p^{th} patch, denoted as $\mathbf{J}_p$, are given by

$$\mathbf{J}_p = \left(\mathbf{L}_p\right)^T \mathbf{b}, \tag{2.13}$$

Equation (2.13) indicates a transformation from coefficients of basis functions to the current density at the quadrature points, which is actually a change of basis. Thus in the operator form, the contribution to the q_m^{th} row from patches sufficiently far from $\mathbf{r}_{q_m}$ via the point-based HO-MOM is expressed as

$$\mathbf{Z}_{q_m}^{far} = \left(\mathbf{k}_{q_m}\right)^T. \tag{2.14}$$

This transformation can also be used for the near interaction calculation. The integral in (2.9) must be evaluated via adaptive quadrature to the desired precision. In the operator form, this is written as

$$\left(\boldsymbol{\kappa}_{q_m}\right)^T \mathbf{b}, \tag{2.15}$$

where $\boldsymbol{\kappa}_{q_m}$ is defined in (2.4) and (2.5). The inverse relation of (2.13) is given by

$$\mathbf{b} = \left[\left(\mathbf{L}_p\right)^T\right]^{-1} \mathbf{J}_p. \tag{2.16}$$

Then (2.15) is rewritten as

$$\left(\boldsymbol{\kappa}_{q_m}\right)^T \left[\left(\mathbf{L}_p\right)^{-1}\right]^T \mathbf{J}_p = \left[\left(\mathbf{L}_p\right)^{-1} \boldsymbol{\kappa}_{q_m}\right]^T \mathbf{J}_p \tag{2.17}$$

The contribution to the $q_m^{\,th}$ row from the near interaction can be written as

$$\mathbf{Z}_{q_m}^{near} = \left[\left(\mathbf{L}_p\right)^{-1} \boldsymbol{\kappa}_{q_m}\right]^T. \tag{2.18}$$

We observe that (2.14) and (2.18) are identical to (2.6) and (2.7), respectively. It follows that point-based HO-MOM scheme is equivalent to the LCN procedure.

2.3 Basis Functions and Discretization

The choice of basis functions should be consistent with the underlying quadrature rule [6]. For example, for smooth geometries, the basis functions are chosen to be Legendre polynomials, and the corresponding Gauss-Legendre quadrature rule is used. For a surface with edge singularities, for example, Jacobi polynomials would provide a much better representation of the singular behavior of the current, and a Gauss-Jacobi quadrature rule should be used.

In this dissertation, we restrict our attention to Legendre polynomials and the corresponding Gauss-Legendre quadrature rule. Polynomial complete basis functions and mixed-order basis functions are introduced in Section 2.3.1 and Section 2.3.2, respectively.

2.3.1 Polynomial complete basis functions

For current density on a PEC surface S, the basis functions should be tangential to the surface. The surface of the conductor is discretized using curvilinear patches that represent the surface to sufficient accuracy. The surface of the patch can be uniquely

represented by a two-dimensional curvilinear space $\left(u^1, u^2\right)$ .The unitary vectors are defined in [24] as

$$\mathbf{a}_i = \frac{\partial \mathbf{r}}{\partial u^i}, \qquad i = 1, 2, \tag{2.19}$$

which is tangential to the curve. The surface current density is expanded over each patch via a set of local vector basis functions. Then the vector basis functions on each patch take the form

$$\mathbf{J}_k^i \left(\mathbf{r}\right) = b_k^i \frac{F_k \left(\mathbf{r}\right)}{\sqrt{g}} \mathbf{a}_i, \qquad \left(i = 1, 2\right) \tag{2.20}$$

where $F_k \left(\mathbf{r}\right)$ are smooth functions placed on each patch, $\sqrt{g} = \mathbf{a}_1 \times \mathbf{a}_2 \cdot \mathbf{a}_n$, and $\mathbf{a}_n$ is the unit normal to S. The choice of $F_k \left(\mathbf{r}\right)$ in this dissertation is the product of Legendre polynomials for three dimensional surface scattering. Note that these functions are truncated at the cell boundaries. As a result the basis functions or the current density are generally discontinuous across cell boundaries. The use of Legendre polynomials makes local correction matrix $\mathbf{L}_p$ defined in (2.4) and (2.5) well-conditioned. If $\mathbf{L}_p$ is square, it is orthogonal and can be inverted simply by transposition.

Following the above notation, the polynomial-complete basis functions that are complete to order p, are expressed with local support in curvilinear coordinates as [8]

$$\mathbf{J}_i^{pc} \left(u^1, u^2\right) = \frac{b_i^{j,k} \mathbf{a}_i P_j \left(u^1\right) P_k \left(u^2\right)}{\sqrt{g}} \qquad \left(i = 1, 2;\ j, k = 0 \ldots p\right), \tag{2.21}$$

where $P_j \left(u\right)$ are j^{th} order Legendre polynomials, and $b_i^{j,k}$ are unknown constant coefficients. Therefore there are $2\left(p+1\right)^2$ degrees of freedom per patch for the surface

current density. Unfortunately, the use of a polynomial complete basis can lead to spurious solutions for geometries with edge singularities. This can be addressed through the introduction of the mixed-order basis [8, 25].

2.3.2 Mixed-order basis functions

The basis functions in (2.21) are used to approximate the electric surface current densities. However, many surface integral equations incorporate a contribution through the divergence of the current. In such cases, the electric charge density is implicitly modeled by the divergence of those basis functions. The electric surface charge density within each cell of the surface can be obtained by taking the divergence of the current, which is expressed [8]

$$\begin{aligned}\rho &= -\frac{1}{j\omega}\nabla_s \cdot \mathbf{J} \\ &= -\frac{1}{j\omega}\sum_{i=1}^{2}\frac{1}{\sqrt{g}}\frac{\partial}{\partial u^i}\left(\sqrt{g}\mathbf{a}^i \cdot \mathbf{J}_i^{pc}\right) \\ &= \frac{-\frac{1}{j\omega}\left[b_1^{j,k}\frac{\partial P_j\left(u^1\right)}{\partial u^1}P_k\left(u^2\right)+b_2^{j,k}P_j\left(u^1\right)\frac{\partial P_k\left(u^2\right)}{\partial u^2}\right]}{\sqrt{g}} \qquad \left(j,k=0...p\right).\end{aligned} \tag{2.22}$$

It is indicated in (2.22) that the electric charge density is represented to an incomplete polynomial order. This incompleteness can yield spurious charges in the solution space that can spoil the solution, especially for scatterers with edge singularities. However, this can be alleviated by the use of mixed-order basis functions.

Mixed basis functions are expressed as [8]

$$\mathbf{J}_1^{mo}\left(u^1,u^2\right)=\frac{b_1^{j,k}\mathbf{a}_1 P_j\left(u^1\right)P_k\left(u^2\right)}{\sqrt{g}} \qquad \left(j=0...p+1;k=0...p\right), \tag{2.23}$$

$$\mathbf{J}_2^{mo}\left(u^1,u^2\right)=\frac{b_2^{j,k}\mathbf{a}_2 P_j\left(u^1\right)P_k\left(u^2\right)}{\sqrt{g}}\qquad \left(j=0...p;k=0...p+1\right), \tag{2.24}$$

where $\mathbf{J}_1^{mo}\left(u^1,u^2\right)$ is polynomial complete to order $p+1$ along u^1 and to order p along u^2, whereas $\mathbf{J}_2^{mo}\left(u^1,u^2\right)$ is polynomial complete to order p along u^1 and to order $p+1$ along u^2. Then the corresponding electric surface charge density within in each cell is expressed as [8]

$$\begin{aligned}\rho &= -\frac{1}{j\omega}\nabla_s\cdot\mathbf{J}\\ &= -\frac{1}{j\omega}\sum_{i=1}^{2}\frac{1}{\sqrt{g}}\frac{\partial}{\partial u^i}\left(\sqrt{g}\mathbf{a}^i\cdot\mathbf{J}_i^{mo}\right)\\ &= \frac{-\frac{1}{j\omega}\left[b_1^{j,k}\frac{\partial P_j\left(u^1\right)}{\partial u^1}P_k\left(u^2\right)+b_2^{j,k}P_j\left(u^1\right)\frac{\partial P_k\left(u^2\right)}{\partial u^2}\right]}{\sqrt{g}},\end{aligned} \tag{2.25}$$

where, the range of j and k in the first term of the last line of (2.25) is the same as that of (2.23), whereas the range of j and k in the second term of the last line of (2.25) is the same as that of (2.24). It is indicated in (2.25) that the surface charge density is polynomial complete to order p. It is demonstrated in [8] that using mixed-order basis function improves the performance of the LCN method for both smooth scatterers and scatterers with edge singularities in terms of the solution accuracy and the condition number.

2.4 Summary

This chapter has presented the locally corrected Nyström method, which is a point-based high-order method. Compared to the conventional Nyström method, the LCN provides a high accuracy discretization of integral operators whose kernels have either

weak or strong singularities (such as most of the operators of interest in electromagnetic analysis) by incorporating local correction strategy. In addition, two different sets of basis functions are introduced for the local corrections. The first is polynomial complete basis function that represents the current completely to a specified order on each cell. This can lead to spurious solution for the scatterers with edge singularizes. However, this can be remedied by the use of the mixed order basis function that represents the charge density completely to a specified order. In the following chapters, the LCN method implemented with Gauss-Legendre quadrature rules and Legendre polynomials basis functions (either polynomial complete or mixed-order) will be used to discretize the surface integral operators that are encountered.

Chapter 3 Surface Integral Equations for a Perfect Electric Conductor

Surface integral equation methods (SIE) [3] are widely used for solving time-harmonic electromagnetic radiation and scattering problems from perfect electric conductors (PECs). The use of SIE for such problems provides several advantages relative to other alternatives. First, compared to PDE-based methods such as finite element method (FEM) [26], it incorporates the radiation condition exactly, leading to fewer approximations. Furthermore, it allows the underlying problems to be represented by meshing only the surfaces of the conductors.

There are two basic surface integral equations for PECs [3], the electric field integral equation (EFIE) and the magnetic field integral equation (MFIE). In the EFIE, the boundary condition is enforced on the tangential electric field, whereas in the MFIE, the boundary condition is enforced on the tangential magnetic field. The EFIE is formulated as a first-kind integral equation, since the unknown quantity appears only under the integral operator. The MFIE is formulated as a second-kind integral equation, since the unknown quantity appears both outside and under the integral operators (MFIE consists of a diagonal operator plus a compact operator). Therefore, the impedance matrix obtained from the MFIE is better conditioned than that from the EFIE. The conditioning of the underlying system matrix is a critical factor either for iterative solvers or for direct solution methods. In this sense, the MFIE should be more useful than the EFIE. But the fact is that the EFIE is useful for much wider range of applications than the MFIE, this is because the EFIE provides accurate solutions for both open structures and structures with geometric singularities. This is the case in spite of the fact that the EFIE possesses a well-

known limitation. The formulation breaks down at low frequencies (or, equivalently, when used with electrically small structures).

Both the EFIE and the MFIE suffer from the interior resonance (or irregular frequency) problem when used with closed structures. In this situation, the uniqueness of the solution of either the EFIE or the MFIE is not guaranteed at the interior resonance frequencies. One of the remedies of such problem is the combined field integral equation method (CFIE) [3], which is obtained from a linear combination of the EFIE and the MFIE. Although the CFIE is the linear combination of the EFIE and the MFIE, its system matrix is better conditioned than that from either the EFIE or the MFIE at such resonant frequencies. For this reason, it is a preferred choice for modeling closed conducting objects. But unfortunately, the low frequency breakdown inherent in the EFIE spoils the conditioning of the CFIE for fine discretization or at low frequencies, and the inaccuracy of the MFIE negatively affects the accuracy of the CFIE when used with geometrically singular structures.

For these reasons, much effort has been spent by many investigators to develop methods and/or formulations that remedy some of the aforementioned limitations of the standard formulations (CFIE, EFIE, MFIE). However existing strategies for addressing these difficulties have their own limitations. The purpose of this dissertation is to develop and demonstrate a new framework for resolving several of these (and related) limitations.

Before moving on to this new work, we spend the remainder of this chapter with a detailed discussion of the standard surface integral equations for PEC obstacles (the EFIE, the MFIE and the CFIE). The remainder of this chapter is organized as follows. Section 3.1 develops the EFIE, the MFIE and the CFIE using field expressions in terms of the

vector potentials. In Section 3.2, the locally corrected Nyström (LCN) [6] discretization of the SIE is demonstrated. In Section 3.3, the well-known low frequency breakdown inherent in the EFIE [1] is analyzed. Finally, Section 3.5 summarizes this chapter.

3.1 The SIE Formulations for Perfectly Electric Conducting Scatterers

The EFIE and the MFIE are derived by using the source-field relationships, the surface equivalence principle and the boundary conditions [3, 27]. We will start from Maxwell's equations and the boundary conditions.

Consider a homogeneous medium with impressed electric current density $\mathbf{J}$ and $\mathbf{M}$. The electromagnetic fields must satisfy Maxwell's equations [27] (an $e^{j\omega t}$ time dependence is assumed),

$$\nabla \times \mathbf{E} = -\mathbf{M} - j\omega\mu\mathbf{H}, \tag{3.1}$$

$$\nabla \times \mathbf{H} = \mathbf{J} + j\omega\varepsilon\mathbf{E}, \tag{3.2}$$

$$\nabla \cdot \mathbf{D} = \rho_e, \tag{3.3}$$

$$\nabla \cdot \mathbf{B} = \rho_m, \tag{3.4}$$

where $\mathbf{E}$ is electric field intensity, $\mathbf{H}$ is magnetic field intensity, $\mathbf{D} = \varepsilon\mathbf{E}$ is electric flux density, $\mathbf{B} = \mu\mathbf{H}$ is magnetic flux density, ρ_e is the electric charge density, ρ_m is the magnetic charge density, ε is electric permittivity, and μ is magnetic permeability, respectively. In addition to the four Maxwell's equations, there is another equation that relates the change of the current density and the charge density. It is referred to as the continuity equation [27]

$$\nabla \cdot \mathbf{J} = -j\omega\rho_e, \tag{3.5}$$

$$\nabla \cdot \mathbf{M} = -j\omega\rho_m. \tag{3.6}$$

At interfaces between media where there are discrete changes in the electrical parameters (such as ε and μ), the field vectors are also discontinuous and their behavior across the boundaries is governed by the boundary conditions [27]

$$\hat{\mathbf{n}} \times \left(\mathbf{E}_1 - \mathbf{E}_2 \right) \Big|_S = -\mathbf{M}_s, \tag{3.7}$$

$$\hat{\mathbf{n}} \times \left(\mathbf{H}_1 - \mathbf{H}_2 \right) \Big|_S = \mathbf{J}_s, \tag{3.8}$$

$$\hat{\mathbf{n}} \cdot \left(\mathbf{D}_1 - \mathbf{D}_2 \right) \Big|_S = \rho_{es}, \tag{3.9}$$

$$\hat{\mathbf{n}} \cdot \left(\mathbf{B}_1 - \mathbf{B}_2 \right) \Big|_S = \rho_{ms}, \tag{3.10}$$

where the subscripts 1 and 2 refer to the medium 1 and medium 2, respectively, $\hat{\mathbf{n}}$ is the unit normal vector to the boundary pointing from medium 2 to medium 1, and the subscript, S, indicates that the current and charge are on the surface. When medium 2 is a perfect electric conductor (PEC) which has infinite conductivity, the electric and magnetic field vectors satisfy the conditions [27]

$$\hat{\mathbf{n}} \times \mathbf{E} \Big|_S = 0, \tag{3.11}$$

$$\hat{\mathbf{n}} \times \mathbf{H} \Big|_S = \mathbf{J}_s, \tag{3.12}$$

$$\hat{\mathbf{n}} \cdot \mathbf{D} \Big|_S = \rho_{es}, \tag{3.13}$$

$$\hat{\mathbf{n}} \cdot \mathbf{B} \Big|_S = 0. \tag{3.14}$$

It is observed that there is a duality that exists in Maxwell's equations describing the complementary fields and sources. Table 3.1 summarizes the duality relationships.

By using Maxwell's equations, the source-field relationships are derived next. In a source free region, equation (3.4) indicates that $\mathbf{H}$ is solenoidal and thus can be written as the curl of another vector,

$$\mathbf{H} = \nabla \times \mathbf{A}, \tag{3.15}$$

where $\mathbf{A}$ is referred to as the magnetic vector potential and is an arbitrary vector. Then substituting (3.15) into (3.1) yields

$$\nabla \times \mathbf{E} = -j\omega\mu \nabla \times \mathbf{A} \Rightarrow \nabla \times \left(\mathbf{E} + j\omega\mu \mathbf{A}\right) = 0 \tag{3.16}$$

It follows that

$$\mathbf{E} = -j\omega\mu \mathbf{A} - \nabla\Phi. \tag{3.17}$$

We will refer to Φ as the electric scalar potential and Φ is an arbitrary scalar that is a function of position. Taking the curl of both sides of (3.15) and applying the vector identity $\nabla \times \nabla \times \mathbf{A} = \nabla\left(\nabla \cdot \mathbf{A}\right) - \nabla^2 \mathbf{A}$ yields

$$\nabla \times \mathbf{H} = \nabla\left(\nabla \cdot \mathbf{A}\right) - \nabla^2 \mathbf{A}. \tag{3.18}$$

Then substituting (3.18) into (3.2) leads to

$$\nabla\left(\nabla \cdot \mathbf{A}\right) - \nabla^2 \mathbf{A} = \mathbf{J} + j\omega\varepsilon \mathbf{E}. \tag{3.19}$$

Substituting (3.17) into (3.19) reduces it to

$$\nabla^2 \mathbf{A} + k^2 \mathbf{A} = -\mathbf{J} + \nabla\left(\nabla \cdot \mathbf{A}\right) + j\omega\varepsilon\nabla\Phi, \tag{3.20}$$

where $k^2 = \omega^2 \mu\varepsilon$.

The Helmholtz Theorem indicates that to uniquely define the vector field $\mathbf{A}$, the divergence of $\mathbf{A}$ is required in addition to the curl of $\mathbf{A}$ shown in (3.15). The Lorentz Gauge is used to simplify (3.20),

$$\nabla \cdot \mathbf{A} = -j\omega\varepsilon\Phi. \tag{3.21}$$

Then by substituting (3.21) into (3.20), (3.20) reduces to

$$\nabla^2 \mathbf{A} + k^2 \mathbf{A} = -\mathbf{J}, \tag{3.22}$$

where the fact $\nabla\left(-j\omega\varepsilon\Phi\right)=-j\omega\varepsilon\nabla\Phi$ is used for homogeneous medium. Equation (3.22) is a vector Helmholtz equation. The solution to it can be obtained by the convolution of $\mathbf{J}$ with the Green's function [3],

$$\mathbf{A}\left(\mathbf{r}\right)=\int_{V}\mathbf{J}\left(\mathbf{r}'\right)G\left(\mathbf{r},\mathbf{r}'\right)dv', \tag{3.23}$$

where $\mathbf{r}$ and $\mathbf{r}'$ are the field and source position vector, respectively, and $G\left(\mathbf{r},\mathbf{r}'\right)=\dfrac{e^{-jk\left|\mathbf{r}-\mathbf{r}'\right|}}{4\pi\left|\mathbf{r}-\mathbf{r}'\right|}$ is the three-dimensional Green's function.

The fields due to $\mathbf{J}$ are expressed as

$$\mathbf{E}=-j\omega\mu\mathbf{A}-\nabla\Phi=-j\omega\mu\mathbf{A}+\frac{1}{j\omega\varepsilon}\nabla\nabla\cdot\mathbf{A}, \tag{3.24}$$

$$\mathbf{H}=\nabla\times\mathbf{A}. \tag{3.25}$$

By duality relationships listed in Table 3.1, the fields due to the magnetic current density, $\mathbf{M}$, are written as

$$\mathbf{E}=-\nabla\times\mathbf{F}, \tag{3.26}$$

$$\mathbf{H}=-j\omega\varepsilon\mathbf{F}-\nabla\Phi_{m}=-j\omega\varepsilon\mathbf{F}+\frac{1}{j\omega\mu}\nabla\nabla\cdot\mathbf{F}, \tag{3.27}$$

where $\mathbf{F}$ is the electric vector potential, $\Phi_{m}=\dfrac{1}{-j\omega\mu}\nabla\cdot\mathbf{F}$ is referred to as the magnetic scalar potential. By duality, $\mathbf{F}$ is expressed as [3]

$$\mathbf{F}\left(\mathbf{r}\right)=\int_{V}\mathbf{M}\left(\mathbf{r}'\right)G\left(\mathbf{r},\mathbf{r}'\right)dv'. \tag{3.28}$$

Thus for arbitrary impressed electric and magnetic current sources, the fields can be expressed as

$$\mathbf{E} = -j\omega\mu\mathbf{A} + \frac{1}{j\omega\varepsilon}\nabla\nabla\cdot\mathbf{A} - \nabla\times\mathbf{F}, \tag{3.29}$$

$$\mathbf{H} = \nabla\times\mathbf{A} - j\omega\varepsilon\mathbf{F} + \frac{1}{j\omega\mu}\nabla\nabla\cdot\mathbf{F}, \tag{3.30}$$

where $\mathbf{A}$ and $\mathbf{F}$ are indicated in (3.23) and (3.28), respectively.

Next, the EFIE and MFIE on the perfect electric conductor (PEC) surface are derived from the equivalence principal and the boundary conditions on the PEC surface [3]. Figure 3.1 shows a PEC embedded in homogeneous medium characterized with ε_1 and μ_1 illustrated by an incident electromagnetic wave with the electric field $\mathbf{E}^i$ and the magnetic field $\mathbf{H}^i$. Figure 3.2 depicts the equivalent problems. In the equivalent problem, the PEC scatterer is replaced by a homogeneous medium with the same constitutive parameters as the exterior region and the fields in the interior region are set to be zero. The equivalent source $\mathbf{J}_s$ is placed along the surface of the PEC scatterer, which will produce the correct scattered fields in the exterior region. Then we can describe this scattering problem as

$$\mathbf{E}^t = \mathbf{E}^i + \mathbf{E}^s \tag{3.31}$$

$$\mathbf{H}^t = \mathbf{H}^i + \mathbf{H}^s \tag{3.32}$$

where, $\mathbf{E}^i$ and $\mathbf{H}^i$ denote the incident fields which are produced by the primary source in the absence of the scatterer; $\mathbf{E}^s$ and $\mathbf{H}^s$ denote the scattered fields which are produced by the equivalent sources, $\mathbf{J}_s$ in this case. Thus the original fields (total fields) in the presence of the scatterer are the superposition of the incident fields and the scattered fields, which are denoted as $\mathbf{E}^t$ and $\mathbf{H}^t$.

The EFIE is derived by enforcing the zero tangential electric field boundary condition of a PEC scatterer indicated in (3.11)

$$\hat{\mathbf{n}} \times \mathbf{E}^t \big|_S = 0. \tag{3.33}$$

where $\hat{\mathbf{n}}$ is the outward normal vector to the surface, S, which bounds the conductor. Then the EFIE can be written as

$$\hat{\mathbf{n}} \times \left(\mathbf{E}^i + \mathbf{E}^s \right) \big|_S = 0. \tag{3.34}$$

Using vector potentials to express $\mathbf{E}^s$ in terms of $\mathbf{J}_s$ indicated by (3.29), the EFIE can be more explicitly written as (cf.(3.23))

$$\begin{aligned} -\hat{\mathbf{n}} \times \mathbf{E}^i(\mathbf{r}) &= -\hat{\mathbf{n}} \times j\omega\mu \mathbf{A}(\mathbf{r}) + \hat{\mathbf{n}} \times \frac{1}{j\omega\varepsilon} \nabla\nabla \cdot \mathbf{A}(\mathbf{r}) \\ &= -j\omega\mu \hat{\mathbf{n}} \times \int_S \mathbf{J}_s(\mathbf{r}') G(\mathbf{r}, \mathbf{r}') ds' + \hat{\mathbf{n}} \frac{1}{j\omega\varepsilon} \times \nabla\nabla \cdot \int_S \mathbf{J}_s(\mathbf{r}') G(\mathbf{r}, \mathbf{r}') ds' \\ &= -jk\eta \hat{\mathbf{n}} \times \int_S \mathbf{J}_s(\mathbf{r}') G(\mathbf{r}, \mathbf{r}') ds' - j\frac{\eta}{k} \hat{\mathbf{n}} \times \nabla\nabla \cdot \int_S \mathbf{J}_s(\mathbf{r}') G(\mathbf{r}, \mathbf{r}') ds', \end{aligned} \tag{3.35}$$

where η is the impedance of the background medium, k is the wave number, $\mathbf{r} \in S$. Alternatively, the tangential component of the electric field can also be obtained by the dot product of a vector $\mathbf{t}$ that is tangential to the surface with $\mathbf{E}^t$, then the scalar form of the EFIE is expressed as

$$-\mathbf{t} \cdot \mathbf{E}^i(\mathbf{r}) = -jk\eta \mathbf{t} \cdot \int_S \mathbf{J}_s(\mathbf{r}') G(\mathbf{r}, \mathbf{r}') ds' - j\frac{\eta}{k} \mathbf{t} \cdot \nabla\nabla \cdot \int_S \mathbf{J}_s(\mathbf{r}') G(\mathbf{r}, \mathbf{r}') ds'. \tag{3.36}$$

The MFIE is derived by enforcing the tangential magnetic field boundary condition of a PEC scatterer indicated in (3.12)

$$\hat{\mathbf{n}} \times \left(\mathbf{H}^i + \mathbf{H}^s \right) \big|_{S^+} = \mathbf{J}_s, \tag{3.37}$$

where S^+ denotes the surface just outside the PEC surface. Similar as that for the EFIE, the MFIE is expressed through (3.23) and (3.30) as

$$\hat{\mathbf{n}}\times\mathbf{H}^i(\mathbf{r}) = \mathbf{J}_s - \hat{\mathbf{n}}\times\nabla\times\int_S \mathbf{J}_s(\mathbf{r}')G(\mathbf{r},\mathbf{r}')\,ds', \tag{3.38}$$

where $\mathbf{r}\in S^+$. Because $\mathbf{H}^s$ undergoes a jump discontinuity between the surface just outside the PEC surface and that just inside, the integral in (3.38) is dual valued, which must be evaluated via a principal value integral. After applying the principal value, it can be shown that

$$\hat{\mathbf{n}}\times\mathbf{H}^s(\mathbf{r}) = \frac{1}{2}\mathbf{J}_s + \hat{\mathbf{n}}\times\nabla\times\int_S \mathbf{J}_s(\mathbf{r}')G(\mathbf{r},\mathbf{r}')\,ds' \quad , \tag{3.39}$$

where, $\mathbf{r}\in S$, $\frac{1}{2}\mathbf{J}_s$ is the residual and $\int$ is the principal value. Then the MFIE becomes

$$\hat{\mathbf{n}}\times\mathbf{H}^i(\mathbf{r}) = \frac{1}{2}\mathbf{J}_s - \hat{\mathbf{n}}\times\nabla\times\int_S \mathbf{J}_s(\mathbf{r}')G(\mathbf{r},\mathbf{r}')\,ds' \quad , \tag{3.40}$$

Applying the vector identity $\nabla\times(\phi\mathbf{a}) = \nabla\phi\times\mathbf{a} + \phi\nabla\times\mathbf{a}$ and $\nabla\times\mathbf{J}_s(\mathbf{r}') = 0$, equation (3.40) is expressed as

$$\hat{\mathbf{n}}\times\mathbf{H}^i(\mathbf{r}) = \frac{1}{2}\mathbf{J}_s - \hat{\mathbf{n}}\times\int_S \nabla G(\mathbf{r},\mathbf{r}')\times\mathbf{J}_s(\mathbf{r}')\,ds' \quad . \tag{3.41}$$

It is noted that (3.41) is written in a vector form. It is more practical to write it in a scalar form. We can apply a dot product of a tangential vector **t** with both sides of (3.41), which leads to

$$\mathbf{t}\cdot\hat{\mathbf{n}}\times\mathbf{H}^i(\mathbf{r}) = \mathbf{t}\cdot\frac{1}{2}\mathbf{J}_s - \mathbf{t}\cdot\hat{\mathbf{n}}\times\int_S \nabla G(\mathbf{r},\mathbf{r}')\times\mathbf{J}_s(\mathbf{r}')\,ds' \quad . \tag{3.42}$$

Applying vector identity $\mathbf{a}\cdot(\mathbf{b}\times\mathbf{c})=\mathbf{c}\cdot(\mathbf{a}\times\mathbf{b})$, equation (3.42) can be further expressed as

$$\mathbf{t}\cdot\hat{\mathbf{n}}\times\mathbf{H}^{i}(\mathbf{r})=\mathbf{t}\cdot\frac{1}{2}\mathbf{J}_{s}-(\mathbf{t}\times\hat{\mathbf{n}})\cdot\oint_{S}\nabla G(\mathbf{r},\mathbf{r}')\times\mathbf{J}_{s}(\mathbf{r}')ds' \quad . \tag{3.43}$$

As pointed earlier in this chapter, the CFIE [3] is one way to eliminate interior resonance problems and is also better conditioned than either the EFIE or the MFIE. The CFIE is the weighted average of the EFIE and MFIE,

$$CFIE=\alpha EFIE+(1-\alpha)\eta MFIE, \qquad 0\le\alpha\le 1, \tag{3.44}$$

where α is a constant.

3.2 The LCN Implementation of the SIE Kernels

In this section, the LCN implementation for the EFIE and the MFIE are presented, especially focusing on the treatment to the hypersingular term. In particular, curvilinear quadrilateral patches will be used to represent the underlying PEC surfaces. The electric current density **J** on each patch will represented using a Legendre approximation for each vector component. The resulting global representation of $\mathbf{J}$ can be written as

$$\begin{aligned}\mathbf{J}(\mathbf{r})&=\sum_{p=1}^{N_p}\mathbf{J}_{p}(\mathbf{r})\\&=\sum_{p=1}^{N_p}\sum_{k=1}^{N_k}\mathbf{J}_{k_p}(\mathbf{r}),\end{aligned} \tag{3.45}$$

where $\mathbf{J}_{p}(\mathbf{r})$ indicates the polynomial representation of $\mathbf{J}(\mathbf{r})$ on p^{th} patch, and N_p is the number of quadrilateral patches in the mesh. In the local correction, $\mathbf{J}_{p}(\mathbf{r})$ is expanded using mixed-order basis functions, thus $\mathbf{J}_{k_p}(\mathbf{r})$ takes the form indicated in (2.23) and (2.24).

3.2.1 The EFIE

Consider the LCN implementation of the EFIE. A single-point kernel evaluation is required for all far interactions. In this regard it is important to recognize that, there is a divergence operator acting $\mathbf{J}(\mathbf{r}')G(\mathbf{r},\mathbf{r}')$, in the EFIE, which is not amenable to the single-point kernel evaluation. To accommodate a point-matching implementation, it is necessary to express the EFIE in an alternate form via the vector identity $\nabla\cdot(\phi\mathbf{a}) = \phi\nabla\cdot\mathbf{a} + \nabla\phi\cdot\mathbf{a}$ and $\nabla\cdot\mathbf{J}(\mathbf{r}') = 0$. It follows

$$\begin{aligned} -\mathbf{t}\cdot\mathbf{E}^i(\mathbf{r}) = &-jk\eta\mathbf{t}\cdot\int_S \mathbf{J}(\mathbf{r}')G(\mathbf{r},\mathbf{r}')\,ds' \\ &-j\frac{\eta}{k}\mathbf{t}\cdot\nabla\int_S \nabla G(\mathbf{r},\mathbf{r}')\mathbf{J}(\mathbf{r}')\,ds'. \end{aligned} \tag{3.46}$$

Next the Gauss-Legendre quadrature rule with weights ω_{q_p} and abscissas $\mathbf{r}_{q_p}$ is introduced on p^{th} patch to replace the integral in (3.46). The ${q_m}^{th}$ row from patches that are sufficiently far from the filed point $\mathbf{r}_{q_m}$ is expressed as

$$\begin{aligned} -\mathbf{a}_{j_{q_m}}\cdot\mathbf{E}^i(\mathbf{r}_{q_m}) = -j\frac{\eta}{k}\sum_{p\in far}\sum_{q=1}^{N_q}\Big[&\omega_{q_p}k^2\mathbf{a}_{j_{q_m}}\cdot\mathbf{J}(\mathbf{r}_{q_p})G(\mathbf{r}_{q_m},\mathbf{r}_{q_p}) \\ &+\omega_{q_p}\mathbf{a}_{j_{q_m}}\cdot\nabla\left(\nabla G(\mathbf{r}_{q_m},\mathbf{r}_{q_p})\cdot\mathbf{J}(\mathbf{r}_{q_p})\right)\Big], \end{aligned} \tag{3.47}$$

where, $\mathbf{a}_{j_{q_m}}$ is a unitary vector evaluated at $\mathbf{r}_{q_m}$; $\mathbf{J}(\mathbf{r}_{q_p}) = \dfrac{J(\mathbf{r}_{q_p})}{\sqrt{g(\mathbf{r}_{q_p})}}\mathbf{a}_i(\mathbf{r}_{q_p})$ indicated by (2.20), $J(\mathbf{r}_{q_p})$ is the unknown to be evaluated.

For the near interaction, just a single integration is required. It is observed that the first integral in (3.46) has a singularity of $O(1/R)$, which is evaluated to the controllable precision using Duffy transform [28] and adaptive quadrature, but the second term is

hypersingular when the source point is approaching the field point. A derivation of an amenable numerical expression is provided below. First, the current density is expanded with the basis functions indicated in (3.45), then the hypersingular term can be expressed as

$$\begin{aligned}
&\int_{S_p} \mathbf{a}_{j_{q_m}} \cdot \nabla \left(\nabla G\left(\mathbf{r}_{q_m}, \mathbf{r}'\right) \cdot \mathbf{J}_{k_p}\left(\mathbf{r}'\right) \right) ds' \\
&= -\int_{S_p} \left(\mathbf{a}_{j_{q_m}} \cdot \nabla \right) \left(\mathbf{J}_{k_p}\left(\mathbf{r}'\right) \cdot \nabla_s{}' \right) \left(G\left(\mathbf{r}_{q_m}, \mathbf{r}'\right) \right) ds' \\
&= -\int_{S_p} \left(\mathbf{J}_{k_p}\left(\mathbf{r}'\right) \cdot \nabla_s{}' \right) \left(\mathbf{a}_{j_{q_m}} \cdot \nabla \right) \left(G\left(\mathbf{r}_{q_m}, \mathbf{r}'\right) \right) ds',
\end{aligned} \tag{3.48}$$

where, $\nabla G\left(\mathbf{r}_{q_m}, \mathbf{r}'\right) = -\nabla' G\left(\mathbf{r}_{q_m}, \mathbf{r}'\right)$; $\nabla' G\left(\mathbf{r}_{q_m}, \mathbf{r}'\right) \cdot \mathbf{J}_{k_p}\left(\mathbf{r}'\right) = \nabla_s{}' G\left(\mathbf{r}_{q_m}, \mathbf{r}'\right) \cdot \mathbf{J}_{k_p}\left(\mathbf{r}'\right)$,since $\mathbf{J}_{k_p}\left(\mathbf{r}'\right)$ is tangential to the surface and $\nabla_s{}'$ is the tangential component of the gradient operator; the second line of (3.48) is obtained by the complementary nature of the operators $\left(\mathbf{J}_{k_p}\left(\mathbf{r}'\right) \cdot \nabla_s{}' \right) \left(\mathbf{a}_{j_{q_m}} \cdot \nabla \right)$. Then using vector identity $\nabla_s \cdot \left(\mathbf{a}\phi \right) = \nabla_s \phi \cdot \mathbf{a} + \phi \nabla_s \cdot \mathbf{a}$, (3.48) is written as

$$\begin{aligned}
&-\int_{S_p} \left(\mathbf{J}_{k_p}\left(\mathbf{r}'\right) \cdot \nabla_s{}' \right) \left(\mathbf{a}_{j_{q_m}} \cdot \nabla \right) \left(G\left(\mathbf{r}_{q_m}, \mathbf{r}'\right) \right) ds' \\
&= -\int_{S_p} \nabla_s{}' \cdot \left[\mathbf{J}_{k_p}\left(\mathbf{r}'\right) \left(\mathbf{a}_{j_{q_m}} \cdot \nabla \right) \left(G\left(\mathbf{r}_{q_m}, \mathbf{r}'\right) \right) \right] ds' \\
&+ \int_{S_p} \nabla_s{}' \cdot \mathbf{J}_{k_p}\left(\mathbf{r}'\right) \left(\mathbf{a}_{j_{q_m}} \cdot \nabla \right) \left(G\left(\mathbf{r}_{q_m}, \mathbf{r}'\right) \right) ds'.
\end{aligned} \tag{3.49}$$

The first term on the right hand side of (3.49) can be further expressed using the divergence theorem for open surfaces [7] as

$$
\begin{aligned}
&-\int_{S_p} \nabla_s' \cdot \left[\mathbf{J}_{k_p}(\mathbf{r}') \left(\mathbf{a}_{j_{q_m}} \cdot \nabla \right) \left(G\left(\mathbf{r}_{q_m}, \mathbf{r}' \right) \right) \right] ds' \\
&= -\oint_{C_p} \left(\hat{\mathbf{e}}_p' \cdot \mathbf{J}_{k_p}(\mathbf{r}') \right) \left(\mathbf{a}_{j_{q_m}} \cdot \nabla \right) \left(G\left(\mathbf{r}_{q_m}, \mathbf{r}' \right) \right) dl',
\end{aligned}
\tag{3.50}
$$

where C_p is the closed contour bounding S_p; $\hat{\mathbf{e}}_p'$ is used to indicate the unit outward normal vector to C_p, which is also tangential to S_p. The second term on the right hand side of (3.49) is written as

$$
\int_{S_p} \nabla_s' \cdot \mathbf{J}_{k_p}(\mathbf{r}') \left(\mathbf{a}_{j_{q_m}} \cdot \nabla \right) \left(G\left(\mathbf{r}_{q_m}, \mathbf{r}' \right) \right) ds' = \int_{S_p} \nabla G\left(\mathbf{r}_{q_m}, \mathbf{r}' \right) \cdot \left(\mathbf{a}_{j_{q_m}} \nabla_s' \cdot \mathbf{J}_{k_p}(\mathbf{r}') \right) ds', \tag{3.51}
$$

which still has a $O\left(1/R^2\right)$ singularity and is not yet numerically integrable. This can be overcome by introducing a tangential vector, $\mathbf{K}_{q_m}(\mathbf{r}')$, which is constructed to be equal to $\mathbf{a}_{j_{q_m}} \nabla_s' \cdot \mathbf{J}_{k_p}(\mathbf{r}')$ where the source point coincides with the field point (singular point), thus cancelling out one order of the singularity. Then with $\mathbf{K}_{q_m}(\mathbf{r}')$, (3.51) is further written as

$$
\begin{aligned}
&\int_{S_p} \nabla G\left(\mathbf{r}_{q_m}, \mathbf{r}' \right) \cdot \left(\mathbf{a}_{j_{q_m}} \nabla_s' \cdot \mathbf{J}_{k_p}(\mathbf{r}') \right) ds' \\
&= \int_{S_p} \nabla G\left(\mathbf{r}_{q_m}, \mathbf{r}' \right) \cdot \left(\mathbf{a}_{j_{q_m}} \nabla_s' \cdot \mathbf{J}_{k_p}(\mathbf{r}') - \mathbf{K}_{q_m}(\mathbf{r}') \right) ds' \\
&+ \int_{S_p} \nabla G\left(\mathbf{r}_{q_m}, \mathbf{r}' \right) \cdot \mathbf{K}_{q_m}(\mathbf{r}') ds'.
\end{aligned}
\tag{3.52}
$$

$\mathbf{K}_{q_m}(\mathbf{r}')$ is constructed as

$$
\mathbf{K}_{q_m}(\mathbf{r}') = \frac{\boldsymbol{\psi}_{q_m}(\mathbf{r}')}{\sqrt{g'}} \left[\sqrt{g} \nabla_s' \cdot \mathbf{J}_{k_p}(\mathbf{r}') \Big|_{\mathbf{r}'=\mathbf{r}_{q_m}} \right], \tag{3.53}
$$

Then $\boldsymbol{\psi}_{q_m}(\mathbf{r}')$ is defined by

$$\boldsymbol{\psi}_{q_m}\left(\mathbf{r}'\right)=\left(\mathbf{a}_{j_{q_m}}\cdot\mathbf{a}^1\right)\Big|_{\mathbf{r}'=\mathbf{r}_{q_m}}\mathbf{a}_1\left(\mathbf{r}'\right)+\left(\mathbf{a}_{j_{q_m}}\cdot\mathbf{a}^2\right)\Big|_{\mathbf{r}'=\mathbf{r}_{q_m}}\mathbf{a}_2\left(\mathbf{r}'\right). \tag{3.54}$$

Such that $\mathbf{K}_{q_m}\left(\mathbf{r}'\right)=\mathbf{a}_{j_{q_m}}\nabla_s{}'\cdot\mathbf{J}_{k_p}\left(\mathbf{r}'\right)$ at the singular point. Then the singularity in the first term on the right hand side of (3.52) is $O\left(1/R\right)$ now and can be integrated by using Duffy transform [28] and adaptive quadrature. The second term on the right hand side of (3.52) can be further expressed as

$$\begin{aligned}\int_{S_p}\nabla G\left(\mathbf{r}_{q_m},\mathbf{r}'\right)\cdot\mathbf{K}_{q_m}\left(\mathbf{r}'\right)ds'=&-\int_{S_p}\nabla_s'\cdot\left(G\left(\mathbf{r}_{q_m},\mathbf{r}'\right)\mathbf{K}_{q_m}\left(\mathbf{r}'\right)\right)ds'\\&+\int_{S_p}G\left(\mathbf{r}_{q_m},\mathbf{r}'\right)\nabla_s'\cdot\mathbf{K}_{q_m}\left(\mathbf{r}'\right)ds'\end{aligned} \tag{3.55}$$

From (3.53) to (3.54), it is obvious that $\nabla_s'\cdot\mathbf{K}_{q_m}\left(\mathbf{r}'\right)=0$. Then by using the open surface divergence theorem on the remaining part,

$$\int_{S_p}\nabla G\left(\mathbf{r}_{q_m},\mathbf{r}'\right)\cdot\mathbf{K}_{q_m}\left(\mathbf{r}'\right)ds'=-\oint_{C_p}\mathbf{e}'\cdot\mathbf{K}_{q_m}\left(\mathbf{r}'\right)G\left(\mathbf{r}_{q_m},\mathbf{r}'\right)dl'. \tag{3.56}$$

In summary, the hypersingular term can be rewritten as

$$\begin{aligned}&\int_{S_p}\mathbf{a}_{j_{q_m}}\cdot\nabla\left(\nabla G\left(\mathbf{r},\mathbf{r}'\right)\cdot\mathbf{J}_{k_p}\left(\mathbf{r}'\right)\right)ds'\\&=\int_{S_p}\nabla G\left(\mathbf{r}_{q_m},\mathbf{r}'\right)\cdot\left(\mathbf{a}_{j_{q_m}}\nabla_s{}'\cdot\mathbf{J}_{k_p}\left(\mathbf{r}'\right)-\mathbf{K}_{q_m}\left(\mathbf{r}'\right)\right)ds'\\&-\oint_{C_p}\left(\hat{\mathbf{e}}_p'\cdot\mathbf{J}_{k_p}\left(\mathbf{r}'\right)\right)\left(\mathbf{a}_{j_{q_m}}\cdot\nabla G\left(\mathbf{r},\mathbf{r}'\right)\right)dl'\\&-\oint_{C_p}\mathbf{e}'\cdot\mathbf{K}_{q_m}\left(\mathbf{r}'\right)G\left(\mathbf{r}_{q_m},\mathbf{r}'\right)dl'.\end{aligned} \tag{3.57}$$

The test points $\mathbf{r}_{q_m}$ are assumed to be inside of the patch and hence do not lie on the contour, thus the contour integrals are non-singular and can be evaluated by using

adaptive quadrature. The surface integral has $O(1/R)$ singularity, thus can be computed to controllable accuracy by the Duffy transform [28] and adaptive quadrature.

3.2.2 The MFIE

Consider the LCN implementation of the MFIE. For far interaction, the q_m^{th} row can be written as (cf.(3.43))

$$\begin{aligned}\mathbf{a}_{j_{q_m}} \cdot \left(\hat{\mathbf{n}}_{j_{q_m}} \times \mathbf{H}^i\left(\mathbf{r}_{q_m}\right)\right) &= \frac{1}{2}\mathbf{a}_{j_{q_m}} \cdot \mathbf{a}_i\left(\mathbf{r}_{q_p}\right)\frac{J\left(\mathbf{r}_{q_p}\right)}{\sqrt{g\left(\mathbf{r}_{q_p}\right)}} \\ &\quad -\left(\mathbf{a}_{j_{q_m}} \times \hat{\mathbf{n}}_{j_{q_m}}\right) \cdot \sum_{p\in far}\sum_{q=1}^{N_q} \omega_{q_p} \nabla G\left(\mathbf{r}_{q_m}, \mathbf{r}_{q_p}\right) \times \mathbf{a}_i\left(\mathbf{r}_{q_p}\right)\frac{J\left(\mathbf{r}_{q_p}\right)}{\sqrt{g\left(\mathbf{r}_{q_p}\right)}},\end{aligned} \tag{3.58}$$

where $\hat{\mathbf{n}}_{j_{q_m}}$ is the outward unit normal to the PEC surface evaluated at the field point $\mathbf{r}_{q_m}$.

For the near interaction, just a single integration is required. Rewrite the integral indicated by (3.43) as

$$\begin{aligned}&\left(\mathbf{t}\times\hat{\mathbf{n}}\right)\cdot\int_S \nabla G\left(\mathbf{r},\mathbf{r}'\right)\times\mathbf{J}_s\left(\mathbf{r}'\right)ds' \\ &= -\left(\mathbf{t}\times\hat{\mathbf{n}}\right)\cdot\int_S\left(\mathbf{J}_s\left(\mathbf{r}'\right)\times\hat{\mathbf{R}}\right)\left(\frac{\partial G\left(\mathbf{r},\mathbf{r}'\right)}{\partial R}\right)ds',\end{aligned} \tag{3.59}$$

where $\mathbf{R}=\mathbf{r}-\mathbf{r}'$, and $R=|\mathbf{R}|$, and $\hat{\mathbf{R}}=|\mathbf{R}|/R$. The term $\frac{\partial G\left(\mathbf{r},\mathbf{r}'\right)}{\partial R}$ has $O\left(1/R^2\right)$ singularity. Note also that, as $R\to 0$, the vector dot product $\left(\mathbf{t}\times\hat{\mathbf{n}}\right)\cdot\left(\mathbf{J}_s\left(\mathbf{r}'\right)\times\hat{\mathbf{R}}\right)\to 0$. It is because the first cross product is tangential to the surface and the second cross product is normal to the surface at the field point. Therefore this zero cancels out one of the poles. Therefore, the kernel indicated by (3.59) has $O(1/R)$ singularity. Then the integral can

be evaluated to the controllable precision using the Duffy transform and adaptive quadrature.

3.3 The Low Frequency Breakdown of the EFIE

A well-known limitation of the EFIE is the fact that the formulation breaks down at low frequencies [1]. The EFIE operator is the sum of a vector potential term that is directly proportional to the frequency and a scalar potential term that is inversely proportional to the frequency. Thus the breakdown occurs because the scalar potential contribution to the tangential electric field overwhelms the contribution from the vector potential at low frequencies. Since the scalar potential places no constraint on the rotational part of the current, this imbalance between the scalar and vector potentials yields a poorly conditioned linear system when the EFIE is discretized.

This breakdown is closely related to the natural Helmholtz decomposition of the current at low frequencies. In Maxwell's equations, the electric and magnetic fields decouple at zero frequency. Accordingly, the electric current $\mathbf{J}$, can be separated into rotational and irrotational components ,

$$\mathbf{J} = \mathbf{J}_R + \mathbf{J}_I, \tag{3.60}$$

where, the rotational component, $\mathbf{J}_R$, is divergence free and generates the magnetic field. The irrotational component $\mathbf{J}_I$ generates the electric field. The continuity equation can be expressed in terms of $\mathbf{J}_I$ as

$$\begin{aligned} -j\omega\rho_e &= \nabla_s \cdot \mathbf{J} \\ &= \nabla_s \cdot \left(\mathbf{J}_R + \mathbf{J}_I\right) \\ &= \nabla_s \cdot \mathbf{J}_I \end{aligned} \tag{3.61}$$

As the frequency is approaching zero, the electric charge density, ρ can be expressed as

$$\rho_e = \lim_{\omega \to 0} \frac{\nabla_s \cdot \mathbf{J}_I}{-j\omega} \tag{3.62}$$

It is observed from (3.62), to produce a physically finite charge as frequency vanishes, $\mathbf{J}_I$ must have a frequency scaling as $\mathbf{J}_I \sim O(\omega)$, whereas $\mathbf{J}_R$ has no such frequency scaling. Furthermore, $\mathbf{J}_R$ is in the null space of the hypersingular (i.e., scalar potential) operator of the EFIE. Therefore, the scalar potential contribution to the EFIE depends only on $\mathbf{J}_I$, whereas the contribution from the vector potential term depends on the total current $\mathbf{J}$. As stated previously, the vector potential part will be numerically lost at very low frequencies, therefore the electric current solved by the EFIE only constrains $\mathbf{J}_I$, which makes the system under-determined. Although small, the vector potential part is essential, since it will generate a non-zero magnetic field when the frequency tends to zero.

3.5 Summary

This chapter has introduced the surface integral equations, the EFIE, the MFIE and the CFIE and their LCN implementations. Their advantages and disadvantages were discussed, especially focusing on the low-frequency breakdown associated with the EFIE. A new strategy for addressing this limitation of the EFIE is provided in the next chapter.

Table 3.1 Principle of Duality

E	**H**
H	**–E**
J	**M**
M	**–J**
ρ_e	ρ_m
ρ_m	$-\rho_e$
ε	μ
μ	ε
A	**F**
F	**–A**

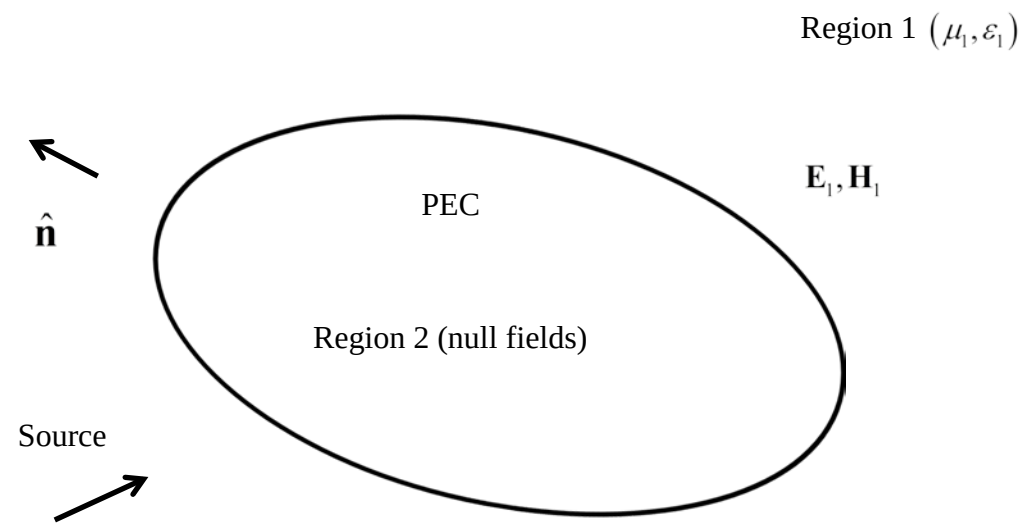

Figure 3.1 Original problem involving a PEC scatterer

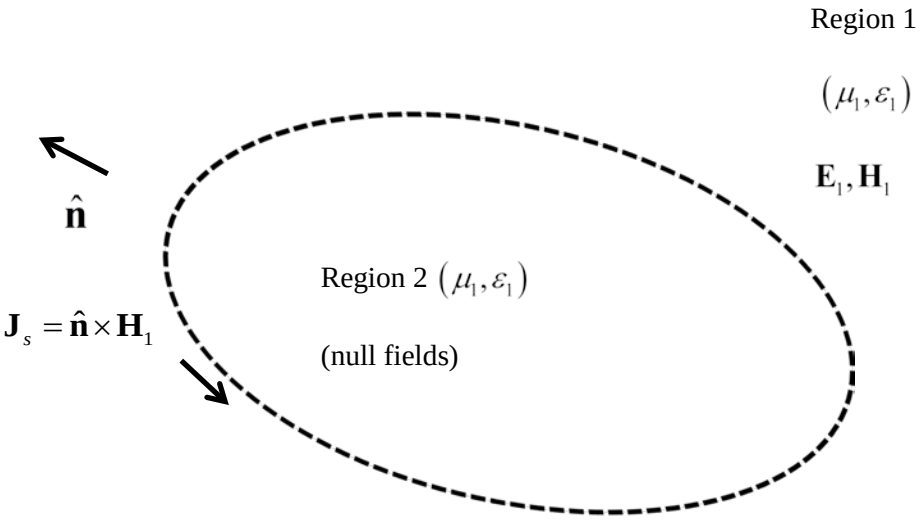

Figure 3.2 Equivalent exterior problem associated with Figure 3.1.

Chapter 4 EFIE-hd Formulation for a Conductor

A new approach to formulate electromagnetic scattering from perfect electric conductors (PEC) is presented in this chapter. This new approach is applied to the electric field integral equation (EFIE), and it incorporates a Helmholtz decomposition (HD) of the current. For this reason, the new formulation is referred to as the EFIE-hd. Unlike the stabilization methods cited in Chapter 1 [1, 10, 11], the HD of the current is accomplished herein via appropriate surface integral constraints, and leads to a stable linear system without having to introduce a HD of the tangential electric field.

For aforementioned reasons, the EFIE-hd enables the use of standard locally corrected Nyström (LCN) discretization methods for the resulting formulation. As with the augmented EFIE (AEFIE) of [18], the frequency stability of the EFIE-hd formulation is achieved without introducing additional non-locality into the problem formulation via either global basis functions or stabilizing global operators. Because of this, the EFIE-hd is amenable to localization-based factorizations [18, 19]. In contrast to the AEFIE, this is accomplished here without introducing charge as an unknown. The EFIE-hd also provides accurate solutions for both the near electric and magnetic fields in cases for which the AEFIE of [18] does not.

The remainder of this chapter is organized as follows. The basic EFIE-hd formulation is developed in Section 4.1, as well as its LCN discretization. Section 4.2 presents the low frequency version of the EFIE-hd (LF-EFIE-hd) formulation and its LCN implementation, since the initial EFIE-hd formulation fails at low frequencies. The numerical results are provided in Section 4.3. Finally section 4.4 concludes this chapter.

4.1 The Development of the EFIE-hd Formulation

4.1.1 The Helmholtz decomposition of the current

Consider the problem of electromagnetic scattering from a perfect electric conductor (PEC) embedded in a homogeneous medium. As discussed in Chapter 3, this problem can be formulated by enforcing the zero tangential electric field boundary condition on the PEC surface, which is referred to as the EFIE,

$$\begin{aligned}\mathbf{M}^i(\mathbf{r}) = &-jk\eta\hat{\mathbf{n}}\times\int_S \mathbf{J}(\mathbf{r}')G(\mathbf{r},\mathbf{r}')\,ds' \\ &-j\frac{\eta}{k}\hat{\mathbf{n}}\times\nabla\int_S\left(\nabla_s'\cdot\mathbf{J}(\mathbf{r}')\right)G(\mathbf{r},\mathbf{r}')\,ds',\end{aligned} \tag{4.1}$$

where $\mathbf{J}$ denotes the electric current density on the conductor, η is the impedance of the background medium, and $G(\mathbf{r},\mathbf{r}')$ is the Green's function of the homogeneous medium. The source term is related to the incident electric field, $\mathbf{E}^i(\mathbf{r})$, as

$$\mathbf{M}^i(\mathbf{r}) = -\hat{\mathbf{n}}\times\mathbf{E}^i(\mathbf{r}), \tag{4.2}$$

where $\hat{\mathbf{n}}$ is the outward normal vector to the surface, S, which bounds the conductor.

For the purposes of the following discussion, it is convenient to express the EFIE in terms of contributions from the vector and scalar potentials,

$$-\frac{1}{\eta}\mathbf{M}^i(\mathbf{r}) = jk\hat{\mathbf{n}}\times\mathbf{A}(\mathbf{J}) + \frac{j}{k}\hat{\mathbf{n}}\times\nabla\Phi(\mathbf{J}), \tag{4.3}$$

where

$$\mathbf{A}(\mathbf{J}) = \int_S \mathbf{J}(\mathbf{r}')G(\mathbf{r},\mathbf{r}')\,ds', \tag{4.4}$$

$$\nabla\Phi(\mathbf{J}) = \nabla\int_S\left(\nabla_s'\cdot\mathbf{J}(\mathbf{r}')\right)G(\mathbf{r},\mathbf{r}')\,ds'. \tag{4.5}$$

The Helmholtz decomposition (HD) of the current can be expressed as

$$\mathbf{J} = \mathbf{J}_R + \mathbf{J}_{I,} \tag{4.6}$$

where $\mathbf{J}_R$ is the rotational part of the current, and $\mathbf{J}_I$ is the irrotational part. The specific forms of these currents are [29],

$$\mathbf{J}_I = \nabla_s \varphi, \tag{4.7}$$

$$\mathbf{J}_R = \hat{\mathbf{n}} \times \nabla_s \psi, \tag{4.8}$$

where φ and ψ are scalar functions defined over the surface of scatterer [29].

Using the representation (4.6) in (4.3) provides

$$\left[jk\hat{\mathbf{n}} \times \mathbf{A} \quad jk\hat{\mathbf{n}} \times \mathbf{A} + \frac{j}{k}\hat{\mathbf{n}} \times \nabla\Phi \right] \begin{bmatrix} \mathbf{J}_R \\ \mathbf{J}_I \end{bmatrix} = -\frac{1}{\eta}\mathbf{M}^i(\mathbf{r}), \tag{4.9}$$

which was obtained by using the fact that [29],

$$\nabla_s \cdot \mathbf{J}_R = \nabla_s \cdot \left(\hat{\mathbf{n}} \times \nabla_s \psi \right) = 0. \tag{4.10}$$

Equation (4.9) may be solvable if discretized using a vector basis that facilitates an explicit HD of the DOF. However, if a standard Nyström basis is used for the currents, then (4.9) is not solvable because it is under-constrained. This occurs because a standard Nyström basis introduces both rotational and irrotational DOF for both $\mathbf{J}_R$ and $\mathbf{J}_I$. Additional constraints are therefore required to effectively distinguish between rotational and irrotaional currents in (4.9) when using basis functions that do not provide an explicit Helmholtz decomposition. For this reason, we next consider the imposition of global constraints on the spaces used for $\mathbf{J}_R$ and $\mathbf{J}_I$.

4.1.2 Zero divergence constraints

To develop the appropriate constraints for the rotational and irrotational current spaces, the Nyström discretization described in Chapter 2 is employed. In particular,

curvilinear quadrilateral patches are used to represent the underlying PEC surfaces. The currents $\mathbf{J}_R$ and $\mathbf{J}_I$ on each patch will be represented using a Legendre approximation for each vector component. The resulting global representation of $\mathbf{J}_R$ can be written as

$$\mathbf{J}_R = \sum_{p=1}^{N_p} \mathbf{J}_R^p, \tag{4.11}$$

where $\mathbf{J}_R^p$ indicates the polynomial representation of $\mathbf{J}_R$ on a given cell, and N_p is the number of quadrilateral patches in the mesh. A corresponding representation of $\mathbf{J}_I$ is

$$\mathbf{J}_I = \sum_{p=1}^{N_p} \mathbf{J}_I^p. \tag{4.12}$$

Given the general forms indicated by (4.7) and (4.8), the current should satisfy the following zero-divergence conditions (cf. (4.10)),

$$\nabla_s \cdot \mathbf{J}_R = 0, \tag{4.13}$$

$$\nabla_s \cdot \left(\hat{\mathbf{n}} \times \mathbf{J}_I\right) = 0. \tag{4.14}$$

Using (4.11) in (4.13) provides

$$\begin{aligned} \nabla_s \cdot \mathbf{J}_R &= \nabla_s \cdot \left(\sum_{p=1}^{N_p} \mathbf{J}_R^p \right) \\ &= \sum_{p=1}^{N_p} \left(\nabla_s^p \cdot \mathbf{J}_R^p \right) + \sum_{e=1}^{N_e} J_{R,diff}^e \left(\mathbf{l}\right) \delta\left(\mathbf{l} - \mathbf{r}\right) = 0. \end{aligned} \tag{4.15}$$

The first term on the last line of (4.15) indicates the divergence of the polynomial representation of the current within each patch. The second term is the contribution from any discontinuities of the current across patch boundaries. The scalar function $J_{R,diff}^e\left(\mathbf{l}\right)$ denotes the difference between the values of the currents normal to and on opposite sides of an edge, and N_e is the number of edges. The vector $\mathbf{l}$ is used to denote the vector

location of all edge points. In the case of two adjacent cells, this can be mathematically represented as

$$J^e_{R,diff}\left(\mathbf{l}\right) = \hat{\mathbf{e}}_1 \cdot \mathbf{J}^1_R\left(\mathbf{l}\right) + \hat{\mathbf{e}}_2 \cdot \mathbf{J}^2_R\left(\mathbf{l}\right), \tag{4.16}$$

where $\hat{\mathbf{e}}_1$ and $\hat{\mathbf{e}}_2$ are used to indicate the outward normal vectors emanating from the two cells at the point indicated by the vector $\mathbf{l}$. Similarly, $\mathbf{J}^1_R$ and $\mathbf{J}^2_R$ indicate the current on opposite sides of the edge at the point $\mathbf{l}$. (The treatment of open surfaces is discussed in Section 4.1.3.)

The constraint (4.15) is equivalent to the two separated conditions

$$\sum_{p=1}^{N_p}\left(\nabla^p_s \cdot \mathbf{J}^p_R\right) = 0, \tag{4.17}$$

$$\sum_{e=1}^{N_e} J^e_{R,diff}\left(\mathbf{l}\right) = 0, \tag{4.18}$$

where the delta-function has been dropped in (4.18).

To improve the conditioning of the final linear system, it is useful to convolve (4.17) with the Green's function,

$$\sum_{p=1}^{N_p}\int_{S_p} G\left(\mathbf{r},\mathbf{r}'\right)\left(\nabla'^p_s \cdot \mathbf{J}^p_R\left(\mathbf{r}'\right)\right) = 0. \tag{4.19}$$

For notational convenience, we will respectively represent (4.19) and (4.18) as

$$D_s\mathbf{J}_R = 0, \tag{4.20}$$

$$D_l\mathbf{J}_R = 0. \tag{4.21}$$

The definitions of D_s and D_l are apparent through a comparison of (4.20) with (4.19) and (4.21) with (4.18).

Conditions analogous to (4.20) and (4.21) can be developed from (4.14) when a similar, piecewise continuous representation is used for $\mathbf{J}_I$. From (4.12),

$$\hat{\mathbf{n}} \times \mathbf{J}_I = \sum_{p=1}^{N_p} \left(\hat{\mathbf{n}} \times \mathbf{J}_I^p \right). \tag{4.22}$$

Using this in (4.14) yields constraints similar to (4.19) and (4.18),

$$\sum_{p=1}^{N_p} \int_{S_p} G\left(\mathbf{r}, \mathbf{r}'\right) \left(\nabla_s'^p \cdot \left(\hat{\mathbf{n}} \times \mathbf{J}_I^p \left(\mathbf{r}' \right) \right) \right) = 0, \tag{4.23}$$

$$\sum_{e=1}^{N_e} J_{I,diff}^e \left(\mathbf{l} \right) = 0, \tag{4.24}$$

where,

$$J_{I,diff}^e \left(\mathbf{l} \right) = \hat{\mathbf{e}}_1 \cdot \left(\hat{\mathbf{n}} \times \mathbf{J}_I^1 \left(\mathbf{l} \right) \right) + \hat{\mathbf{e}}_2 \cdot \left(\hat{\mathbf{n}} \times \mathbf{J}_I^2 \left(\mathbf{l} \right) \right). \tag{4.25}$$

Equations (4.23) and (4.24) can be respectively expressed as

$$D_s \left(\hat{\mathbf{n}} \times \mathbf{J}_I \right) = 0, \tag{4.26}$$

$$D_l \left(\hat{\mathbf{n}} \times \mathbf{J}_I \right) = 0, \tag{4.27}$$

where operators D_s and D_l are identical to those defined above.

Combining (4.20) through (4.27) with (4.9) yields

$$\begin{bmatrix} D_s & \mathbf{0} \\ D_l & \mathbf{0} \\ \mathbf{0} & D_s\left(\hat{\mathbf{n}}\times\right) \\ \mathbf{0} & D_l\left(\hat{\mathbf{n}}\times\right) \\ jk\hat{\mathbf{n}}\times\mathbf{A} & \left(jk\hat{\mathbf{n}}\times\mathbf{A} + \dfrac{j}{k}\hat{\mathbf{n}}\times\nabla\Phi \right) \end{bmatrix} \begin{bmatrix} \mathbf{J}_R \\ \mathbf{J}_I \end{bmatrix} = -\frac{1}{\eta} \begin{bmatrix} \mathbf{0} \\ \mathbf{0} \\ \mathbf{0} \\ \mathbf{0} \\ \mathbf{M}^i \end{bmatrix}. \tag{4.28}$$

The formulation indicated by (4.28) is referred to as the EFIE-hd formulation for closed surfaces.

4.1.3 Modification for open surfaces

The extension of (4.28) to open structures can be accomplished through appropriate modifications of (4.16) for $\mathbf{J}_R$ and (4.25) for $\mathbf{J}_I$. Equation (4.16) reduces at an open edge to

$$J^e_{R,diff}\left(\mathbf{l}\right) = \hat{\mathbf{e}} \cdot \mathbf{J}_R\left(\mathbf{l}\right). \tag{4.29}$$

When used in (4.18), this effectively imposes the condition that the component of the rotational current that is normal to an edge of the open surface must vanish. Because the modification indicated by (4.29) is a straightforward specialization of (4.16) that, in practice, amounts to incorporating all rotational currents available at each edge, the condition indicated by (4.21) will be used without change for both open and closed surfaces (for an open edge, there is only one current and (4.16) naturally reduces to (4.29)).

In contrast, the form of D_l required in (4.27) is changed for an open surface. At an open edge, the constraint indicated by (4.25) is not used; the current $\hat{\mathbf{n}} \times \mathbf{J}_I$ is only constrained via (4.25) at internal mesh edges. We denote the modified form of (4.27) as

$$D_{l,I}\left(\hat{\mathbf{n}} \times \mathbf{J}_I\right) = 0. \tag{4.30}$$

The operator $D_{l,I}$ differs from D_l in that it imposes no constraints at open edges of the mesh. Using (4.30), the EFIE-hd for open surfaces is thus,

$$\begin{bmatrix} D_s & \mathbf{0} \\ D_l & \mathbf{0} \\ \mathbf{0} & D_s\left(\hat{\mathbf{n}}\times\right) \\ \mathbf{0} & D_{l,I}\left(\hat{\mathbf{n}}\times\right) \\ jk\hat{\mathbf{n}}\times\mathbf{A} & \left(jk\hat{\mathbf{n}}\times\mathbf{A} + \frac{j}{k}\hat{\mathbf{n}}\times\nabla\Phi\right) \end{bmatrix} \begin{bmatrix} \mathbf{J}_R \\ \mathbf{J}_I \end{bmatrix} = -\frac{1}{\eta} \begin{bmatrix} \mathbf{0} \\ \mathbf{0} \\ \mathbf{0} \\ \mathbf{0} \\ \mathbf{M}^i \end{bmatrix}. \tag{4.31}$$

The only change in (4.31) relative to (4.28) is the incorporation of $D_{l,I}$ rather than D_l in constraining $\hat{\mathbf{n}} \times \mathbf{J}_I$.

4.1.4 The LCN implementation of EFIE-hd

The formulations indicated by (4.28) and (4.31) are discretized using the locally corrected Nyström (LCN) method [6, 8] For local corrections, a mixed-order Legendre polynomial basis with order $p \times (p+1)$ is used for each of the tangential components of $\mathbf{J}_I$, and a $p \times p$ order representation is used for each tangential component of $\mathbf{J}_R$. The scalar ranges of the D_s operators were tested on a $(p+1) \times (p+1)$ grid of points on each patch. The edge operator D_l in (4.28) is tested at $(p+1)$ points along each edge of the mesh. For open geometries, $D_{l,I}$ of (4.31) is tested at $(p+1)$ points along all interior mesh edges; test points are not used on open edges. The last row of (4.28) is the EFIE, which is tested using the strategy discussed in Section 3.2.1.

The specified LCN discretization of (4.28) yields a system matrix that has the following row and column dimensions:

$$\begin{aligned} n_{cols} &= \left(2(q+1)q + 2q^2\right) N_p \\ &= 4q^2 N_p + 2qN_p \\ n_{rows} &= q^2 N_p + qN_e + q^2 N_p + qN_e + 2(q+1)qN_p \\ &= 4q^2 N_p + 2qN_p + 2qN_e \\ &= 4q^2 N_p + 6qN_p \end{aligned} \tag{4.32}$$

where $q = p+1$ is the number of quadrature points, and we have used the fact that the number of edges in a closed quadrilateral mesh is twice the number of patches

$\left(N_e = 2N_c\right)$. The number of rows $\left(n_{rows}\right)$ in (4.32) was obtained from the number of test points used for each equation in (4.28), as indicated above.

From (4.32) it is clear that the proposed LCN discretization of (4.28) yields an over-determined linear system $\left(n_{rows} > n_{cols}\right)$. A similar result is obtained from (4.31) for open structures. These over-determined linear systems are herein solved using an Hermitian complement strategy. In particular, let the matrix equation obtained from the LCN discretization of (4.28) or (4.31) be denoted

$$\mathbf{Zx} = \mathbf{F}, \tag{4.33}$$

where $\mathbf{Z}$ is the over-determined system matrix. This system is herein solved by performing an LU factorization of the following square system,

$$\mathbf{Z}^H\mathbf{Zx} = \mathbf{Z}^H\mathbf{F}, \tag{4.34}$$

where $\mathbf{Z}^H$ denotes the Hermitian conjugate of $\mathbf{Z}$.

It has previously been shown that sparse direct solution methods can also be used for non-square systems such as (4.33) [19], which will be described in the next chapter.

Not surprisingly, the EFIE-hd eventually breaks down as the frequency is lowered. As can be observed from (4.28), the contributions from the vector potential and the scalar potential are still imbalanced. At sufficiently low frequencies, the contribution of the vector potential to the EFIE is numerically negligible. This is problematic since the vector potential provides the primary constraints on the rotational current, $\mathbf{J}_R$. The next section outlines a strategy for addressing this low-frequency breakdown of the EFIE-hd.

4.2 The Low Frequency version of EFIE-hd

4.2.1 Formulation and matrix form

In order to solve the low-frequency breakdown of the aforementioned EFIE-hd formulation, the constraints provided by the vector potential can be more effectively incorporated by considering the divergence of the EFIE (4.3),

$$\begin{aligned} -\frac{1}{jk\eta}\nabla_s\cdot\mathbf{M}^i(\mathbf{r}) &= \nabla_s\cdot\left(\hat{\mathbf{n}}\times\mathbf{A}(\mathbf{J})\right)+\frac{1}{k^2}\nabla_s\cdot\left(\hat{\mathbf{n}}\times\nabla\Phi(\mathbf{J})\right) \\ &= \nabla_s\cdot\left(\hat{\mathbf{n}}\times\mathbf{A}(\mathbf{J})\right) \\ &= Q(\mathbf{J}), \end{aligned} \tag{4.35}$$

where we have again used (4.10). The operator Q is introduced in (4.35) for notational convenience,

$$Q(\mathbf{J}) = \nabla_s\cdot\left(\hat{\mathbf{n}}\times\mathbf{A}(\mathbf{J})\right). \tag{4.36}$$

Using (4.35) with (4.28) and scaling $\mathbf{J}_I$ with the wavenumber provides the following form of the EFIE-hd,

$$\begin{bmatrix} D_s & \mathbf{0} \\ D_l & \mathbf{0} \\ \mathbf{0} & D_s(\hat{\mathbf{n}}\times) \\ \mathbf{0} & D_l(\hat{\mathbf{n}}\times) \\ jk\hat{\mathbf{n}}\times\mathbf{A} & \left(-k^2\hat{\mathbf{n}}\times\mathbf{A}-\hat{\mathbf{n}}\times\nabla\Phi\right) \\ Q/(2\pi) & jkQ/(2\pi) \end{bmatrix} \begin{bmatrix} \mathbf{J}_R \\ \mathbf{J}_I \end{bmatrix} = -\frac{1}{jk\eta} \begin{bmatrix} \mathbf{0} \\ \mathbf{0} \\ \mathbf{0} \\ \mathbf{0} \\ jk\mathbf{M}^i \\ \frac{1}{2\pi}\nabla_s\cdot\mathbf{M}^i \end{bmatrix}. \tag{4.37}$$

An additional factor of $1/(2\pi)$ is included in the last row of the system in order to balance the norms of the operators and improve the conditioning of the resulting linear system. The corresponding formulation for open geometries is obtained by replacing D_l

with $D_{l,I}$ in the fourth row of (4.37) (cf.(4.31)). Equation (4.37) will be referred to as the low-frequency (LF) version of the EFIE-hd.

The scaling of the irrotational current introduced in (4.37) is motivated by the dual divergence constraints imposed on $\mathbf{J}_I$ and $\hat{\mathbf{n}} \times \mathbf{J}_I$. The divergence of $\mathbf{J}_I$ is indicated by the continuity equation [27],

$$\nabla_s \cdot \mathbf{J}_I = -j\omega\rho, \tag{4.38}$$

where ρ is the surface charge density. The divergence of $\hat{\mathbf{n}} \times \mathbf{J}_I$ is constrained in (4.37) as indicated by (4.14). Taken together, these conditions indicate that $|\mathbf{J}_I| \propto k$.

4.2.2 The LCN implementation of the LF EFIE-hd

The LF EFIE-hd indicated by (4.37) is discretized using the same locally corrected Nyström method described for open and closed geometries in Section 4.1.5. The newly introduced row obtained from (4.36) is tested on a scalar grid of $(p+1)\times(p+1)$ points on each quadrilateral patch, and the over-determined system is again solved using the method indicated by (4.34).

4.3 Numerical Examples

In this section, the frequency stability of LF EFIE is studied and the validity of EFIE-hd at high frequencies and LF EFIE-hd at both high frequencies and low frequencies are demonstrated.

4.3.1 Frequency stability of LF EFIE

For this study, a one-meter radius PEC sphere, a one-meter PEC cube, and a one-meter square PEC plate are used. The surface of the sphere, the cube and the square plate are discretized using 367, 150, 25 bilinear quadrilateral patches, respectively. The basis

order is $p=1$. As pointed out previously in this chapter, the EFIE-hd eventually breaks down as the frequency is lowered. This is indicated in Figure 4.1, which depicts the condition number of (4.28) as a function of frequency for the 1-meter radius PEC sphere. The condition number is observed to increase quadratically with the inverse of the frequency. The source of this behavior is evident from (4.28): contributions to (4.28) from the vector potential terms are proportional to frequency, whereas the contributions from the scalar potential term are proportional to the inverse of the frequency. Also in Figure 4.1, the condition number of the LF EFIE-hd is plotted versus frequency for the above three geometries. Unlike the EFIE-hd (4.28), the condition number of (4.37) is stable as the frequency is decreased. Note also that, in the case of the sphere, the condition number of the LF EFIE-hd (4.37) is somewhat higher than the condition of the EFIE-hd (4.28) at 100 MHz. This difference in the condition numbers obtained from the two formulations is primarily due to the scaling of $\mathbf{J}_I$ by the wavenumber in (4.37). That scaling is physically most appropriate at lower frequencies.

4.3.2 High frequencies

In this section, the validity of EFIE-hd as well as LF EFIE-hd at higher frequencies for deferent geometries is demonstrated.

The first example considers the problem of a $-\hat{\mathbf{z}}$ travelling plane wave (polarized along the $\hat{\mathbf{x}}$ direction) scattering from a one-meter radius, PEC sphere. The surface of the sphere is discretized using 367 bilinear quadrilateral cells, and the basis order is $p=1$. Figure 4.2 and Figure 4.3 show the scattering cross-sections of the sphere at frequencies of 50 and 300 MHz, respectively. The EFIE-hd and LF EFIE-hd solutions are in good agreement with both the analytical solution and the standard EFIE solution.

The cross-sections obtained for a one-meter cube at 50 MHz using the standard EFIE, the EFIE-hd (4.28) and the LF EFIE-hd (4.37) with $p=1$ are shown in Figure 4.4. Although not shown, similarly good agreement is observed at 300 MHz for this geometry.

Finally, consider the problem of scattering from the corner reflector illustrated in Figure 4.5. The excitation in this case is a plane wave incident from the $\theta=\pi/4, \varphi=\pi/4$ direction. The linearly polarized electric field points in $0.5\hat{\mathbf{x}}+0.5\hat{\mathbf{y}}-0.707\hat{\mathbf{z}}$ direction. The corner reflector is an open geometry, and it is necessary to use the EFIE-hd formulation indicated by (4.31) and the LF EFIE-hd formulation indicated by (4.37) replacing D_l with $D_{l,I}$ in the fourth row of (4.37) (cf.(4.31)). Figure 4.6 shows scattered cross-sections obtained at 50 MHz using the EFIE and EFIE-hd formulations with $p=1$ and $p=2$. The agreement between the two solutions is good, and both solutions appear to be converging to the same result as the order is increased. Figure 4.6 also shows the computed scattered cross-section obtained at 50 MHz using the LF EFIE-hd formulation with $p=1$, which agrees well with those computed using the standard EFIE and the EFIE-hd of (4.31). Although not shown, similarly good agreement is observed at 300 MHz for this geometry.

4.3.3 Low frequencies

Consider the near fields excited by a 1 Hz, $-\hat{\mathbf{z}}$ traveling plane wave polarized along the $\hat{\mathbf{x}}$ direction incident on a one-meter radius PEC sphere discretized with 367 bilinear quadrilaterals and basis order $p=1$. Figure 4.7 illustrates the $\varphi-$directed near electric and magnetic fields computing using the LF-EFIE-hd at a distance of 0.5 meters above the sphere. Also shown are the Mie series and AEFIE [18] solutions. Good agreement among all three formulations is obtained for the near electric field. Similarly

good agreement is observed between the Mie series and LF EFIE-hd solutions for the near magnetic field. Large errors are observed in the near magnetic field obtained from the AEFIE at this frequency. The latter errors might be corrected by using a perturbative strategy similar to that reported in [30]; this possibility is not investigated here.

Finally, Figure 4.8 displays the near electric and magnetic scattered fields computed using the AEFIE and LF EFIE-hd for the corner reflector of Figure 4.5. The excitation is a 1 Hz plane wave incident from the $\theta = \pi/4, \varphi = \pi/4$ direction. The linearly polarized electric field points in the $0.5\hat{\mathbf{x}} + 0.5\hat{\mathbf{y}} - 0.707\hat{\mathbf{z}}$ direction. Excellent agreement is again observed between the AEFIE and LF EFIE-hd solutions for the near electric field. As observed above for the PEC sphere, there is a large difference between the two solutions for the near magnetic field. While it appears that the AEFIE solution for $\left|\mathbf{H}_{\phi}^{s}\right|$ is inaccurate due to its large magnitude, the accuracy of the LF EFIE-hd solution is more difficult to evaluate in this case due to the lack of an analytical solution.

4.4 Summary

In this chapter, a new electric field-based formulation for scattering from perfect electric conductors, which is referred to as the EFIE-hd, is presented and developed in detail. The formulation provides stable and accurate solutions for the electric and magnetic fields at low frequencies through a Helmholtz decomposition of the surface current. Instead of relying on a topological decomposition of the basis into rotational and irrotational subspaces, the EFIE-hd incorporates appropriate global constraints to effectively enforce the desired decomposition on the independent vector basis spaces used for the rotational and irrotational currents. Furthermore, the new formulation does not rely on a HD of the tangential electric field.

By also incorporating a constraint on the divergence of the EFIE, it has been shown that the resulting system enables the application of a single LCN discretization strategy at all frequencies considered. The solutions obtained from the resulting over-determined system have been observed to be accurate for both open and closed geometries.

The EFIE-hd does not rely on charge to achieve frequency stability. However, it does approximately double the number of degrees of freedom used to represent the surface current when used with an LCN discretization. This is because there is no convenient method for topologically identifying rotational and irrotational subspaces when using a Nyström discretization. It may be possible to avoid this increase in the DOF by using a current representation that admits a topological decomposition, but this possibility has not been explored.

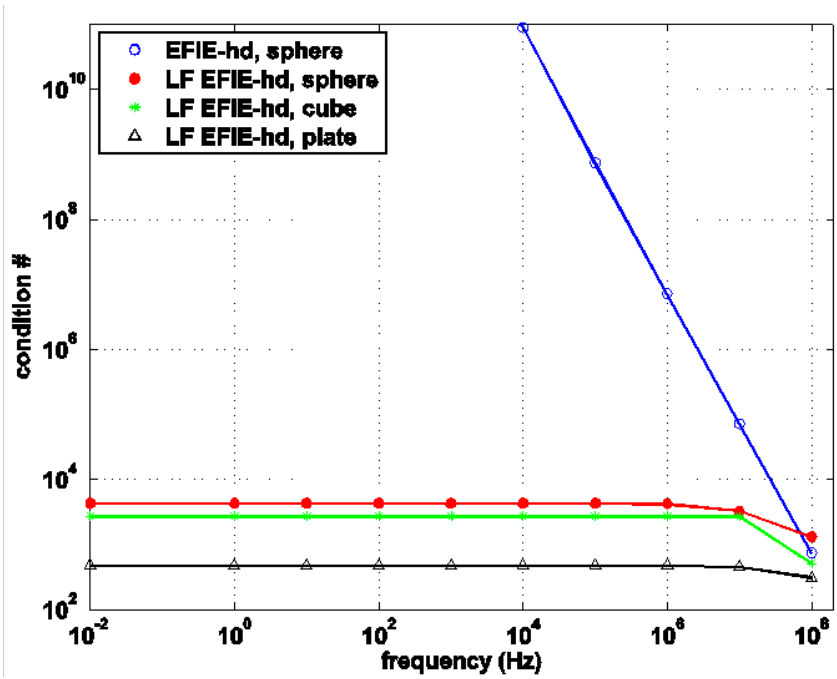

Figure 4.1 Condition number of matrix obtained from LCN discretization of EFIE-hd and LF EFIE-hd for several PEC geometries $(p=1)$.

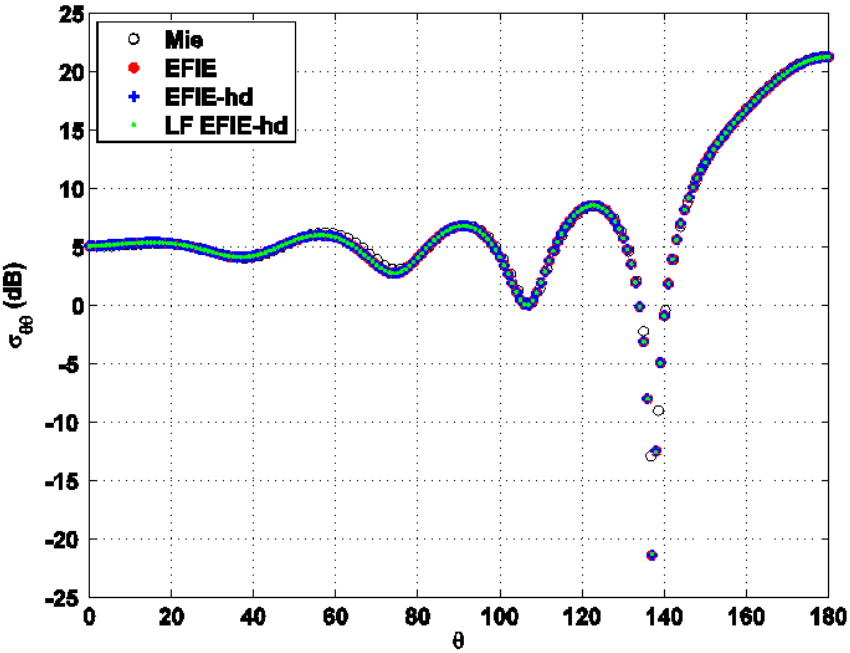

Figure 4.2 The cross-section at 300 MHz for plane wave scattering from a 1-meter radius PEC sphere $(\varphi=0)$.

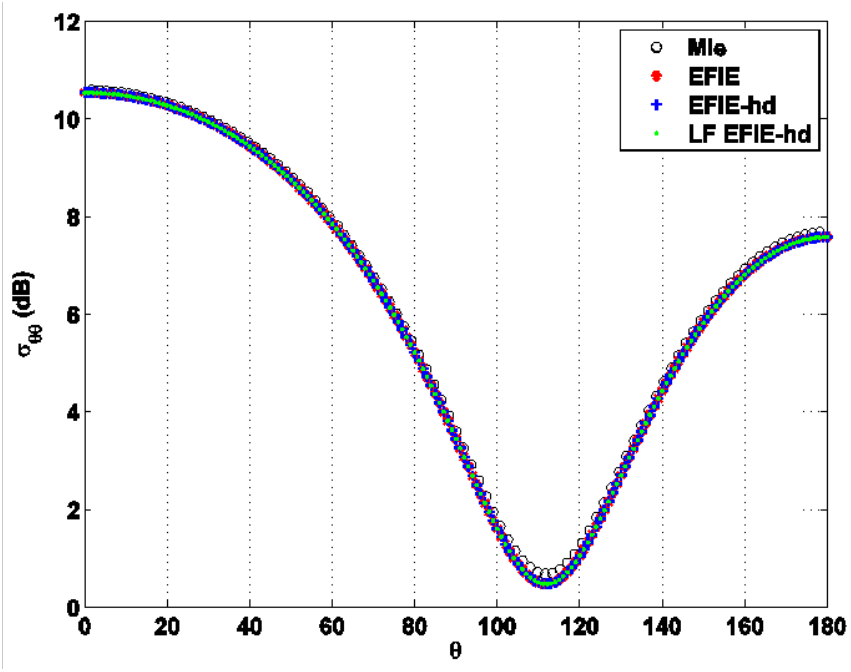

Figure 4.3 Same as Figure 4.2 at 50 MHz.

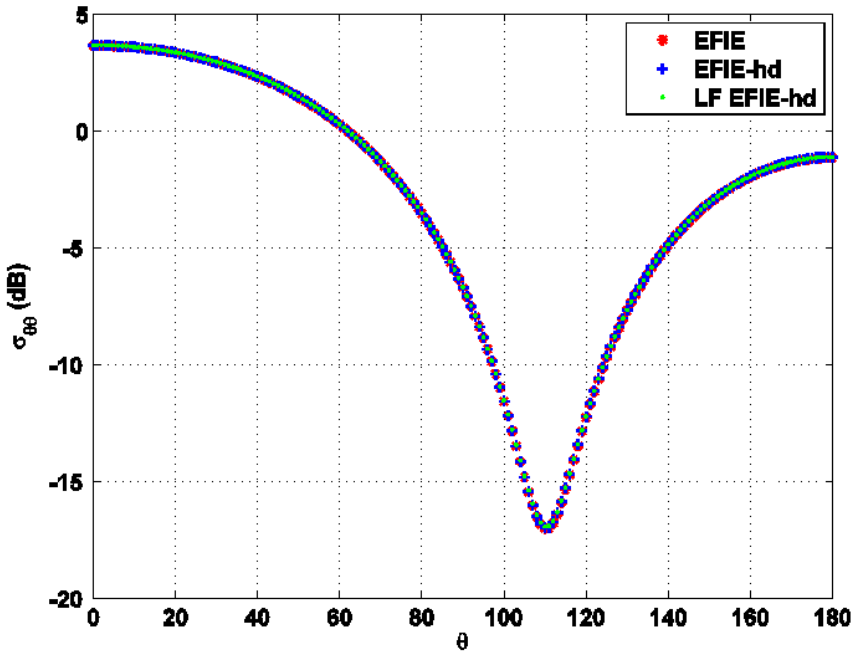

Figure 4.4 Cross-section at 50 MHz for plane wave scattering from a one-meter PEC cube $(\varphi = 0)$.

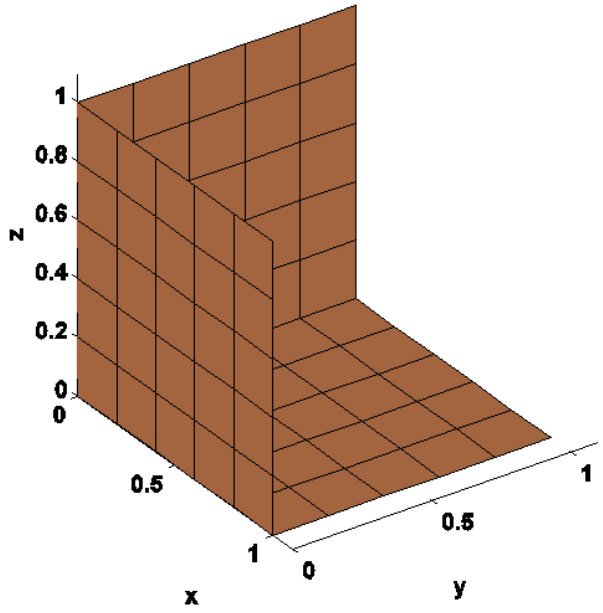

Figure 4.5 The corner reflector geometry is composed of three, 1-meter square plates and discretized using a uniform quadrilateral mesh.

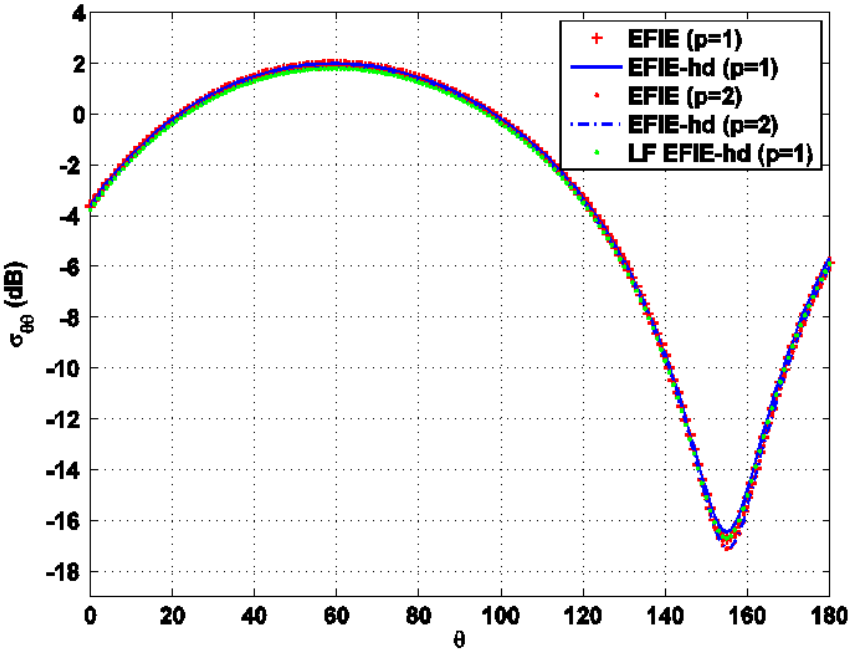

Figure 4.6 50 MHz cross-section for plane wave scattering form the corner reflector illustrated in Figure 4.5 $(\varphi = 0)$.

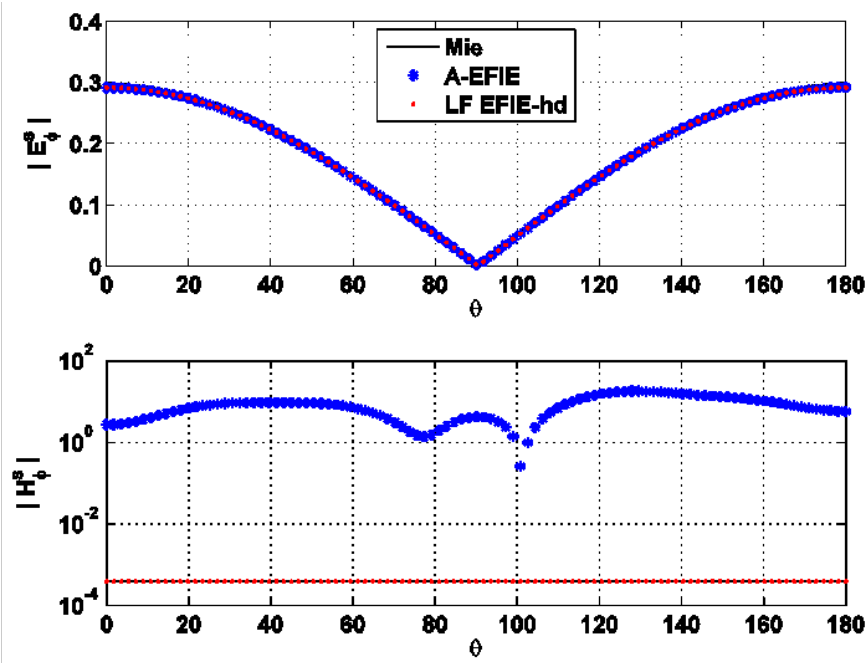

Figure 4.7 Scattered electric (top) and magnetic (bottom) fields computed using a Mie series, AEFIE and LF EFIE-hd formulations for 1 Hz plane wave scattering from 1-meter radius PEC sphere. The near fields are sampled 0.5 m above the PEC surface.

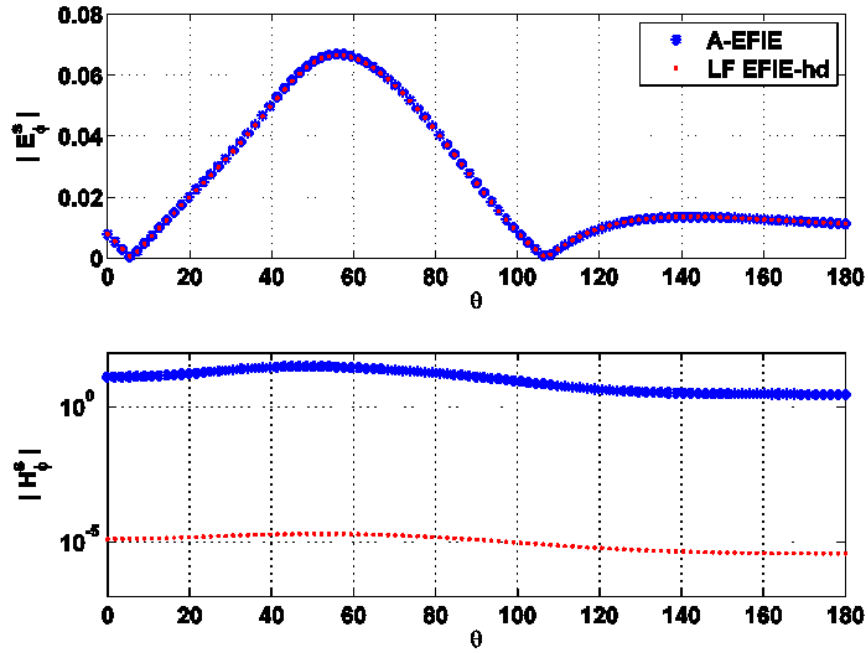

Figure 4.8 Near electric and magnetic scattered fields for 1 Hz plane wave excitation of the corner reflector of Figure 4.5. Fields are sampled on the semicircle of radius 2 m centered on the origin.

Chapter 5 Direct Solution Method Using Overlapped Localizing LOGOS Modes for AEFIE and AEFIE-G at Low Frequencies

In this chapter, a fast, direct numerical analysis method using overlapped localizing local-global modes (OL-LOGOS) [4, 5] is considered for solving electromagnetic problems at low frequencies. We focus on the importance of using well-conditioned formulations to obtain efficient numerical performance from the OL-LOGOS solution algorithm. The well-conditioned formulation that will be considered is the augmented EFIE(AEFIE) [18, 19]. The application of the OL-LOGOS algorithm to the EFIE-hd formulation developed in the previous chapter will not be treated in this dissertation.

The augmented electric field integral equation (AEFIE) with a locally corrected Nyström (LCN) discretization [18, 19] can partially overcome the low frequency breakdown problem inherent in the conventional EFIE. The AEFIE remains well conditioned at very low frequencies, and it provides accurate solutions for the electric field. However, the magnetic fields computed using the AEFIE are incorrect (see Figure 4.7 above), and it is difficult to effectively extend the well-conditioned nature of the AEFIE to non-PEC materials. The performance of the OL-LOGOS algorithm for the AEFIE is considered nevertheless as it provides a relevant formulation that is well-conditioned with respect to both frequency changes and mesh refinement. It thus provides a useful vehicle for exploring the performance of the OL-LOGOS algorithm.

The AEFIE is obtained by augmenting the conventional EFIE with the continuity equation and including charge as additional set of unknowns [16, 18]. In this way, the

contributions of the vector potential and the scalar potential terms are separated to remove the imbalance at low frequencies.

The LCN method is used to discretize the AEFIE formulation [18]. As pointed out in Chapter 2, the LCN method has several advantages. In addition to providing high order error convergence, the LCN scheme has a distinct advantage over Galerkin scheme in that only a single integration is required for the near interaction and just a single-point kernel evaluation is required for the far interaction. This feature speeds up the fill procedure in local-global solution (LOGOS) framework.

When using a Nyström scheme the current is represented in terms of Legendre polynomials in each patch of the mesh and is generally discontinues across cell boundaries. This discontinuity in the current gives rise to line charges on cell boundaries. Therefore, in the implementation of AEFIE with the LCN discretization, additional degrees of freedom for line charges are required, and a reduced version of the continuity equation is obtained for line charge along patch edges. It has been shown that the surface charge and line charge still satisfy charge neutrality constraints, which can be included as an additional row in the system matrix, thus yielding an over-determined system matrix. While the resulting AEFIE is frequency stable, it is not stable with respect to mesh refinement. An improved formulation is obtained by convolving the continuity equation on the surface with the Green's function. The resulting formulation is herein referred to as the AEFIE-G. It has been found that, with appropriate (diagonal) scaling. The AEFIE-G provides a formulation for low frequency field interactions with conducting structures that is stable with respect to both frequency and mesh refinement.

In order to solve large scale and complex electromagnetic problems, a LOGOS based fast direct solver [4, 5] is used to factor the AEFIE and AEFIE-G system matrices. In particular, the overlapped localizing LOGOS (OL-LOGOS) framework will be considered here. To solve the rank deficiency issue of the system matrix at low frequencies, the charge neutrality constraint can be explicitly enforced by reducing the number of unknowns [16]. However, this may result in poor local conditioning of the system matrix. Alternatively, the charge neutrality constraint can be added to the existing AEFIE or AEFIE-G matrix [19], yielding an over-determined system matrix (more rows than columns). As shown later in this chapter, it is straightforward to apply a LOGOS-based solver to the resulting over-determined system [19]. In particular, the additional row is carried along as an additional constraint, which is imposed at each step of the factorization.

The remainder of this chapter is organized as follows. In Section 5.1, the AEFIE and the AEFIE-G with LCN discretization are developed in detail. The conditioning of the underlying system matrix is also discussed. The LOGOS factorization is reviewed in Section 5.2, especially focusing on the OL-LOGOS scheme. The modification to the over-determined system is also provided. Numerical results are presented in Section 5.3. Finally conclusions are provided in Section 5.4.

5.1 The AEFIE and AEFIE-G formulation

5.1.1 Derivation from the regular EFIE

In deriving the AEFIE we begin with the EFIE for a PEC surface expressed as [3]

$$\mathbf{t}\cdot\mathbf{E}^i(\mathbf{r}) = jk\eta\mathbf{t}\cdot\int_S \mathbf{J}(\mathbf{r}')G(\mathbf{r},\mathbf{r}')ds' + j\frac{\eta}{k}\mathbf{t}\cdot\nabla\int_S\left(\nabla G(\mathbf{r},\mathbf{r}')\cdot\mathbf{J}(\mathbf{r}')\right)ds', \qquad (5.1)$$

where $G(\mathbf{r},\mathbf{r}')$ is the free-space Green's function, S is the surface of the underlying PEC object, $\mathbf{J}(\mathbf{r}')$ is the unknown surface current density, $\mathbf{E}^i(\mathbf{r})$ is the incident electric field, and $\mathbf{t}$ is the test vector tangential to S evaluated at the observation point $\mathbf{r}$, and $e^{j\omega t}$ is assumed. The surface S is discretized using general curvilinear quadrilateral patches. Since the current expanded in terms of Legendre polynomials is continuous within each patch, the integrals in (5.1) can be split into integrals over cells. Then by applying some vector identities and surface divergence theorem [7] to the integral over each patch, we obtain [18, 19]

$$\begin{aligned}\mathbf{t}\cdot\mathbf{E}^i(\mathbf{r}) = \eta\sum_{p=1}^{N_p}\Bigg[& \mathbf{t}\cdot\int_{S_p} jk\mathbf{J}(\mathbf{r}')G(\mathbf{r},\mathbf{r}')\,ds' \\ & +(j/k)\int_{S_p}\left(\mathbf{t}\cdot\nabla G(\mathbf{r},\mathbf{r}')\right)\left(\nabla_s'\cdot\mathbf{J}(\mathbf{r}')\right)ds' \\ & +(j/k)\oint_{C_p}\left(\mathbf{t}\cdot\nabla G(\mathbf{r},\mathbf{r}')\right)\left(-\hat{\mathbf{e}}'\cdot\mathbf{J}(\mathbf{r}')\right)dl'\Bigg],\end{aligned} \tag{5.2}$$

where C_p is the contour bounding a patch surface S_p, $\hat{\mathbf{e}}'$ is the outward unit vector normal to C_p tangential to S_p at the source point $\mathbf{r}'$. The last term of the right hand side of (5.2) is the contribution from the current discontinuities, since in a Nyström discretization, the normal continuity of the current is not explicitly enforced. This is rewritten as a summation over all edges in the mesh [18, 19]

$$(j/k)\sum_{e=1}^{N_e}\int_{l_e}\left(\mathbf{t}\cdot\nabla G(\mathbf{r},\mathbf{r}')\right)\left(-\hat{\mathbf{e}}_1'\cdot\mathbf{J}_1(\mathbf{r}')-\hat{\mathbf{e}}_2'\cdot\mathbf{J}_2(\mathbf{r}')\right)dl', \tag{5.3}$$

where N_e is the total number of edges in the mesh, l_e is an edge, $\hat{\mathbf{e}}_1'$ and $\hat{\mathbf{e}}_2'$ are the two outward unit vectors associated with the patches on either side of the edge l_e that are perpendicular to l_e and tangential to the surface of associated cell at the source point $\mathbf{r}'$.

The continuity equation on the patch surface yields

$$\nabla_s' \cdot \mathbf{J}(\mathbf{r}) = -j\omega q_s(\mathbf{r}), \tag{5.4}$$

And its reduced version on an edge is

$$-\hat{\mathbf{e}}_1 \cdot \mathbf{J}_1(\mathbf{r}) - \hat{\mathbf{e}}_2 \cdot \mathbf{J}_2(\mathbf{r}) = -j\omega q_s(\mathbf{r}). \tag{5.5}$$

The use of (5.3) to (5.5) in (5.2) leads to [18, 19]

$$\begin{aligned} \mathbf{t} \cdot \mathbf{E}^i(\mathbf{r}) = \eta \Bigg[& \mathbf{t} \cdot \sum_{p=1}^{N_p} \int_{S_p} jk\mathbf{J}(\mathbf{r}') G(\mathbf{r},\mathbf{r}') ds' \\ & + \sum_{p=1}^{N_p} \int_{S_p} \left(\mathbf{t} \cdot \nabla G(\mathbf{r},\mathbf{r}')\right) c q_s(\mathbf{r}') ds' \\ & + \sum_{e=1}^{N_e} \int_{l_e} \left(\mathbf{t} \cdot \nabla G(\mathbf{r},\mathbf{r}')\right) c q_l(\mathbf{r}') dl' \Bigg], \end{aligned} \tag{5.6}$$

where $q_s(\mathbf{r}')$ is the surface charge within patches, $q_l(\mathbf{r}')$ is the line charge on edges, and c is the speed of light. If $jk\mathbf{J}(\mathbf{r}')$, $cq_s(\mathbf{r}')$ and $cq_l(\mathbf{r}')$ are used as unknowns, it is recognized that there is no imbalance between vector and scalar potential terms in the EFIE. It also should be noted that on each connected conductor, the charge neutrality still holds for (5.4) and (5.5). For each connected surface [18]

$$\sum_{p=1}^{N_p} \int_{S_p} cq_s(\mathbf{r}') ds' - \sum_{e=1}^{N_e} \int_{l_e} cq_l(\mathbf{r}') dl' = 0. \tag{5.7}$$

The above charge neutrality constraint can be explicitly enforced by removing one column and one row from the system matrix indicates by (5.6) which corresponds to one

charge unknown. The selection of the redundant charge unknown is arbitrary, which may result in bad conditioning of the system matrix and will be shown later. Alternatively, this charge neutrality constraint is added to the existing AEFIE system matrix as an additional constraint, yielding an over-determined system matrix (more rows than columns). The EFIE augmented with continuity equations and charge neutrality constraint is represented as [19]

$$\begin{bmatrix} \mathbf{L}_A & \mathbf{L}_{q_s} & \mathbf{L}_{q_l} \\ \mathbf{D}_s & -k^2\mathbf{I} & \mathbf{0} \\ \mathbf{D}_l & \mathbf{0} & -k^2\mathbf{I} \\ \mathbf{0} & \mathbf{N}_{q_s} & \mathbf{N}_{q_l} \end{bmatrix} \begin{bmatrix} jk\mathbf{J} \\ c\mathbf{q}_s \\ c\mathbf{q}_l \end{bmatrix} = \frac{1}{\eta} \begin{bmatrix} \mathbf{V} \\ \mathbf{0} \\ \mathbf{0} \\ \mathbf{0} \end{bmatrix}. \tag{5.8}$$

The definition of the quantities in (5.8) are obvious from a comparison of (5.8) to (5.6), (5.4), (5.5) and (5.7). $\mathbf{D}_s$ and $\mathbf{D}_l$ are sparse.

The AEFIE-G is obtained by the convolution of (5.4) with the free space Green's function on each patch [19]

$$\int_{S_p} G(\mathbf{r},\mathbf{r}')\nabla_s' \cdot \mathbf{J}(\mathbf{r}')\, ds' = -\int_{S_p} G(\mathbf{r},\mathbf{r}')\, j\omega q_s(\mathbf{r})\, ds'. \tag{5.9}$$

The left-hand-side is not amenable to a single point kernel evaluation for far interaction due to the operation of ∇_s' on the unknown, $\mathbf{J}(\mathbf{r}')$. This is inconvenient for a Nyström implementation. Thus we further manipulate (5.9) using a vector identity and the surface divergence theorem. In this way, the left hand side can be expressed as

$$\begin{aligned} &\int_{S_p} G(\mathbf{r},\mathbf{r}')\nabla_s' \cdot \mathbf{J}(\mathbf{r}')\, ds' \\ &= \int_{S_p} \nabla_s' \cdot \left(G(\mathbf{r},\mathbf{r}')\mathbf{J}(\mathbf{r}')\right) ds' - \int_{S_p} \mathbf{J}(\mathbf{r}')\nabla_s' G(\mathbf{r},\mathbf{r}')\, ds' \\ &= \oint_{C_P} \left(\mathbf{e}' \cdot \mathbf{J}(\mathbf{r}')\right) G(\mathbf{r},\mathbf{r}')\, dl' - \int_{S_p} \mathbf{J}(\mathbf{r}')\nabla_s' G(\mathbf{r},\mathbf{r}')\, ds', \end{aligned} \tag{5.10}$$

where C_p is the contour bounding S_p, $\mathbf{e}'$ is the outward unit vector normal to C_p tangential to S_p. With $jk\mathbf{J}(\mathbf{r}')$, $cq_s(\mathbf{r}')$ and $cq_l(\mathbf{r}')$ as unknowns, equation (5.10) can be rewritten for the whole mesh as

$$\begin{aligned} 0 = &\sum_{p=1}^{N_p} \int_{S_p} \left(jk\mathbf{J}(\mathbf{r}') \right) \nabla_s' G(\mathbf{r},\mathbf{r}')\, ds' \\ &+ \sum_{p=1}^{N_p} \int_{S_p} k^2 \left(cq_s(\mathbf{r}') \right) G(\mathbf{r},\mathbf{r}')\, ds' \\ &+ \sum_{e=1}^{N_e} \int_{l_e} k^2 \left(cq_l(\mathbf{r}') \right) G(\mathbf{r},\mathbf{r}')\, ds'. \end{aligned} \tag{5.11}$$

Note also that there are no operators in front of the unknowns, which is convenient for a Nyström implementation. The matrix form of AEFIE-G can finally be written as

$$\begin{bmatrix} \mathbf{L}_A & \mathbf{L}_{q_s} & \mathbf{L}_{q_l} \\ \mathbf{D}_{s(G)} & \mathbf{L}_{q_s(G)} & \mathbf{L}_{q_L(G)} \\ \mathbf{D}_l & \mathbf{0} & -k^2\mathbf{I} \\ \mathbf{0} & \mathbf{N}_{q_s} & \mathbf{N}_{q_l} \end{bmatrix} \begin{bmatrix} jk\mathbf{J} \\ c\mathbf{q}_s \\ c\mathbf{q}_l \end{bmatrix} = \frac{1}{\eta} \begin{bmatrix} \mathbf{V} \\ \mathbf{0} \\ \mathbf{0} \\ \mathbf{0} \end{bmatrix}. \tag{5.12}$$

The definition of quantities of the second row of (5.12) is obvious from a comparison of (5.12) with (5.11). It is observed that (5.12) is more symmetric than (5.8).

5.1.2 The LCN implementation of AEFIE and AEFIE-G

The AEFIE and AEFIE-G are discretized using the LCN method [6, 8]. For the local corrections, a mixed-order Legendre polynomial basis with order $p \times (p+1)$ is used for each of the tangential components of $jk\mathbf{J}(\mathbf{r}')$, a polynomial complete Legendre polynomial basis with order $p \times p$ is used for the surface charges $c\mathbf{q}_s(\mathbf{r}')$ and a polynomial complete Legendre polynomial basis with order p is used to present the line charges $c\mathbf{q}_l$.

5.1.3 Discussion on frequency and mesh stability

Note that, elements in (5.8) and (5.12) depend on frequency through Green's function $G(\mathbf{r},\mathbf{r}')$. When frequency is very low, $G(\mathbf{r},\mathbf{r}')$ becomes a static Green's function $1/(4\pi|\mathbf{r}-\mathbf{r}'|)$ that is not depending on the frequency. Therefore, the AEFIE and AEFIE-G system matrix are frequency independent at low frequency. However, the condition numbers obtained from above formulations are still fairly large and the resulting system matrixes are unstable with mesh refinement at a fixed frequency. We next consider diagonal scaling to further reduce the condition number and to achieve mesh stability.

To investigate this mesh instability, a $1m\times 1m$ plate is studied with mesh refinement when the frequency is 1 Hz. The mesh is discretized using a uniform distribution of square cells arranged as 3×3, 9×9 and 16×16 arrays, respectively. Take AEFIE system matrix indicated by (5.8) for example, at very low frequencies, the matrix elements of $-k^2\mathbf{I}$ are quite small due to k^2. Thus we restrict our attention to studying how the singular values of the remaining nonzero matrix blocks scale with the mesh refinement. Figure 5.1 shows the singular value distribution of $\mathbf{L}_{q_s}$ with mesh refinement. From the top figure, it is observed that the distributions of the singular values of this block for the different meshes are widely apart from each other. If this matrix block is scaled by a constant, s_p equal to the area of the patch, i.e., $s_p\mathbf{L}_{q_s}$. In this case, since the plate is uniformly discretized, the areas of each individual cell for a fixed mesh are the same. Then the new singular value distributions for the various mesh resolutions exhibit much less variation, as shown in the bottom of Figure 5.1. Then the same numerical

experiments are carried out to other block matrices, similar conclusions are obtained. It is found that by appropriate scaling (diagonal scaling) in terms of corresponding area of the patch and length of the edge, the condition number of the system matrix is significantly reduced. Table 5.1 shows the condition number of the system matrix before and after scaling, and we refer this scaling strategy to as usual scaling. It should be noted that, in this case, the charge neutrality constraint is explicitly enforced to form a square system. Also from Table 5.1 we can see that the conditioning of the AEFIE-G system is better than that of the AEFIE system. Note also that, the condition numbers of both formulations are reduced significantly. However, the system is still unstable with mesh refinement, in that the condition number increases versus mesh refinement.

In the previous test, charge neutrality is enforced directly by reducing the number of unknowns, which is way too arbitrary and will result in bad conditioning of the system matrix. Instead, we stack the charge neutrality constraint as an additional row with AEFIE/AEFIE-G matrix to form an over-determined system matrix, then solve for the solution by the method of least squares. Table 5.2 shows the condition number of the square and over-determined AEFIE matrix with usual scaling for the $1m \times 1m$ plate example. Though improved, the formulation is still unstable with mesh refinement. Figure 5.2 and Figure 5.3 show the singular value distributions versus mesh refinement of AEFIE and AEFIE-G, respectively for the $1m \times 1m$ plate test case when the frequency is set to be 1 Hz. It is observed that as mesh is refined, there are more small drops of the singular values with the largest singular value almost unchanged for both formulations. Note also that, better conditioning is still obtained by AEFIE-G formulation. However after further scaling in terms of area of patch and length of edge for specific matrix

blocks on top of usual scaling, the small drops of singular values can be lifted a lot. Figure 5.4 and Figure 5.5 show the singular value distributions versus mesh refinement of AEFIE and AEFIE-G after further scaling. It is observed that mesh stable and small condition number system matrix can be obtained through this scaling strategy, and the AEFIE-G formulation is more stable than AEFIE.

5.2 The OL-LOGOS Framework

5.2.1 Review

Local-global solution (LOGOS) modes provide a computationally efficient framework for developing fast, direct solution methods for electromagnetic simulations [4]. The basic idea behind the solution framework consists in representing the system matrix and its inverses in an organized basis of local solutions that satisfy global constraints. These solutions are referred to as local-global solution (LOGOS) modes. An essential feature of this framework is that LOGOS modes provide a single basis within which both the system matrix and its inverse are sparse. When combined with other CEM technologies (e.g., compression methods for system matrix), this feature of the LOGOS basis can be used to develop fast direct solvers.

Integral equation (IE) based formulations are used to simulate the electromagnetic problems in frequency domain, which involves solving linear matrix equations of the form

$$\mathbf{Z}\mathbf{x} = \mathbf{F}^i, \tag{5.13}$$

where the matrix $\mathbf{Z}$ is the dense $N \times N$ system matrix. The vector $\mathbf{x}$ contains the unknown field or current coefficients, and $\mathbf{F}^i$ contains spatial samples of an impressed or incident source. Standard direct methods for solving the above linear equations have

$O\left(N^3\right)$ CPU time complexity and $O\left(N^2\right)$ memory complexity. The LOGOS framework can provide improved CPU and memory efficiencies. A brief review of the LOGOS solution method is provided below [4].

Let the domain (surface is used herein) where the underlying simulation domain is defined be denoted S. S is then decomposed into two non-overlapping pieces

$$S = S_1 + S_2 \tag{5.14}$$

S_1 and S_2 are referred to as "Region 1" and "Region 2", respectively. Above decomposition of S leads to an associated decomposition of (5.13)

$$\begin{bmatrix} \mathbf{Z}_{11} & \mathbf{Z}_{12} \\ \mathbf{Z}_{21} & \mathbf{Z}_{22} \end{bmatrix} \begin{bmatrix} \mathbf{x}_{1,m} \\ \mathbf{x}_{2,m} \end{bmatrix} = \begin{bmatrix} \mathbf{F}^i_{1,m} \\ \mathbf{F}^i_{2,m} \end{bmatrix}, \tag{5.15}$$

where $\mathbf{x}_{1,m}$ is the portion of $\mathbf{x}_m$ associated with Region 1, $\mathbf{x}_{2,m}$ is the portion associated with Region 2, $\mathbf{Z}_{12}$ indicated interactions from Region 2 to Region 1, etc. The integer subscript "m" on $\mathbf{x}_m$ and $\mathbf{F}^i_m$ is used to index the LOGOS modes. A single LOGOS mode is thus defined by an excitation/solution pair $\left(\mathbf{F}^i_m, \mathbf{x}_m\right)$.

The determination of LOGOS modes for which $\mathbf{x}_m$ has nonzero support only in Region 1 (i.e., $\mathbf{x}_{1,m} \neq 0, \mathbf{x}_{2,m} = 0$) is provided below. The local condition associated with these modes is

$$\mathbf{Z}_{11}\mathbf{x}_{1,m} = \mathbf{F}^i_{1,m}. \tag{5.16}$$

The global condition is

$$\mathbf{Z}_{21}\mathbf{x}_{1,m} = \mathbf{F}^i_{2,m}. \tag{5.17}$$

Combing (5.16) and (5.17) provides a local-global condition

$$\mathbf{Z}_{21}\mathbf{Z}_{11}^{-1}\mathbf{F}_{1,m}^{i}=\mathbf{F}_{2,m}^{i}, \tag{5.18}$$

which is satisfied by all LOGOS modes. The condition (5.18) can be used to determine LOGOS modes that have sources $\left(\mathbf{x}_m\right)$ only confined to Region 1, to $O\left(\varepsilon\right)$. However, the scattered field $\left(\mathbf{Z}\mathbf{x}_m\right)$ may or may not be confined to Region1. Up until this point, it is useful to introduce two classifications for LOGOS modes: localizing versus non-localizing, and overlapping versus non-overlapping.

The localizing LOGOS modes are required to develop efficient solvers for low- to mid- frequency problems where the maximum linear dimension of the scatterer is not large relative to the wavelength, whereas non-localizing modes are required to develop efficient factorizations at high frequencies. Localizing LOGOS modes are obtained by imposing (to order $-\varepsilon$) (5.18) for the case $\mathbf{F}_{2,m}^{i}=0$

$$\mathbf{Z}_{21}\mathbf{Z}_{11}^{-1}\mathbf{F}_{1,m}^{i}=0. \tag{5.19}$$

These LOGOS modes are denoted as "localizing" LOGOS modes because the field scattered from Region 1 to Region 2 is zero to order $-\varepsilon$ $\left(\mathbf{Z}_{21}\mathbf{x}_{1,m}\approx 0\right)$. Note also that, equation (5.19) is not a non-radiating condition, which only imposes the weaker condition that the desired sources in Region 1 do not radiate to observers in Region 2 (to order $-\varepsilon$). The localizing LOGOS modes determined from the constraint (5.19) may actually radiate strongly to spatial regions outside of Region 1 and Region 2. These localizing modes can be used to factor the system matrix $\mathbf{Z}$. The modes satisfying (5.18) which do not also satisfy (5.19) (to order $-\varepsilon$) are referred to as non-localizing LOGOS modes. A non-localizing LOGOS mode is a solution/excitation pair, $\left(\mathbf{F}_m,\mathbf{x}_m\right)$, in this situation, the source $\left(\mathbf{x}_m\right)$ is localized to a small region of a larger target, and the

excitation $\left(\mathbf{F}_m\right)$ is a global function, which is generally nonzero over the entire simulation domain. The localizing LOGOS modes determined from constraint (5.19) lead directly to sparse representations of $\mathbf{Z}$ and $\mathbf{Z}^{-1}$ (due to localization in both the domain and range of $\mathbf{Z}$), whereas the scattered fields $\left(\mathbf{Zx}\right)$ associated with non-localizing LOGOS modes are generally nonzero over the entire simulation domain. In this dissertation, the localizing LOGOS modes are used to factor the underlying system matrix.

The LOGOS modes, determined by the algebraic constraints (5.18) and (5.19), relies on the non-overlapping decomposition of the simulation domain indicated by (5.14). For this reason, the LOGOS modes determined using (5.19) are referred to as non-overlapping, localizing LOGOS (NL-LOGOS) modes. Overlapped LOGOS modes are determined by modifying (5.18) as follows:

$$\mathbf{Z}_{2n}\mathbf{Z}_{1n}^{\dagger}\mathbf{F}_{1,m}^{i}=\mathbf{F}_{2,m}^{i}, \tag{5.20}$$

where $\mathbf{Z}_{1n}\left(\mathbf{Z}_{2n}\right)$ is the corresponding system matrix block which maps from sources in Region 1 and its touching neighbor groups to scattered fields in Region 1 (Region 2). The symbol † indicates a pseudo-inverse. Overlapped LOGOS modes can be used to develop more efficient factorization methods for general electromagnetic applications in two and three dimensions, which will be used in this dissertation.

5.2.2 The OL-LOGOS procedure

The formulation and notation used in the following description of the OL-LOGOS procedure closely follows that used elsewhere [5] and Figure 5.6 and Figure 5.7 are cited also from reference [5]. Before proceeding to the discussion on the OL-LOGOS

factorization, it is convenient to introduce how this LOGOS framework works. Let us begin with the NL-LOGOS factorization.

The LOGOS factorization starts with the decomposition of a discretized geometry into a multilevel oct-tree in a manner similar to the fast multipole method (FMM) [20]. A thin, perfectly electric conducting (PEC) strip is used to illustrate the following discussion. The PEC strip is decomposed by a 3-level oct-tree which is shown in Figure 5.6(a) [5]. As it is shown, there are four non-empty groups at level-3, two non-empty groups at level-2 and one at level-1. The surface electric field integral equation (EFIE) is used to formulate the scattering problem associated with this thin PEC strip, which yields a square dense system matrix $\mathbf{Z}$ with either MoM or the LCN discretization, as shown in Figure 5.6(b) [5]. The matrix $\mathbf{Z}$ is partitioned according to the level-3 groups.

In a NL-LOGOS factorization, a sparse square matrix, $\mathbf{\Lambda}_3 = \left[\mathbf{\Lambda}_3^{(L)} \mathbf{\Lambda}_3^{(N)} \right]$, is used to denote the source modes at level-3, where $\mathbf{\Lambda}_3^{(L)}$ contains the localizing source modes and $\mathbf{\Lambda}_3^{(N)}$ contains the non-localizing source modes which are shown in Figure 5.6(b) [5]. The corresponding scattered fields are expressed as

$$\left[\mathbf{E}^{(L)} \quad \mathbf{E}^{(N)} \right] \approx \mathbf{Z} \left[\mathbf{\Lambda}_3^{(L)} \quad \mathbf{\Lambda}_3^{(N)} \right], \tag{5.21}$$

where $\mathbf{E}^{(L)}$ are the localized (block diagonal) fields. The approximation made in (5.21) is controlled by the factorization tolerance [31]. Figure 5.6(b) [5] shows the configuration of $\mathbf{E}^{(L)}$ and $\mathbf{E}^{(N)}$. Then a unitary projection matrix, $\mathbf{P}_3 = \left[\mathbf{P}_3^{(L)} \quad \mathbf{P}_3^{(N)} \right]$, is subsequently obtained by QR factorizations for every matrix block in $\mathbf{E}^{(L)}$ such that

$$\mathbf{E}^{(L)} = \mathbf{QR} = \left[\mathbf{Q}_1 \quad \mathbf{Q}_2 \right] \begin{bmatrix} \mathbf{R}_1 \\ \mathbf{0} \end{bmatrix}. \tag{5.22}$$

Then let $\mathbf{P}_3^{(L)} = \mathbf{Q}_1$ and $\mathbf{P}_3^{(N)} = \mathbf{Q}_2$. Matrix $\mathbf{P}_3^{(L)}$ has the same configuration as $\mathbf{E}^{(L)}$ and spans $\mathbf{E}^{(L)}$. Matrix $\mathbf{P}_3^{(N)}$ has the same configuration as $\mathbf{\Lambda}_3^{(N)}$ and is orthogonal to $\mathbf{Z}\mathbf{\Lambda}_3^{(L)}$. Thus the NL-LOGOS factorization of $\mathbf{Z}$ at level-3 can be expressed as

$$\mathbf{Z} = \mathbf{Z}_3 = \mathbf{P}_3 \hat{\mathbf{Z}}_3 \mathbf{\Lambda}_3^{-1}, \tag{5.23}$$

where,

$$\hat{\mathbf{Z}}_3 = \mathbf{P}_3^H \mathbf{Z}_3 \mathbf{\Lambda}_3 \approx \begin{bmatrix} \mathbf{I} & \left(\mathbf{P}_3^{(L)}\right)^H \mathbf{Z}_3 \mathbf{\Lambda}_3^{(N)} \\ \mathbf{0} & \left(\mathbf{P}_3^{(N)}\right)^H \mathbf{Z}_3 \mathbf{\Lambda}_3^{(N)} \end{bmatrix} = \begin{bmatrix} \mathbf{I} & \mathbf{Z}_3^{(LN)} \\ \mathbf{0} & \mathbf{Z}_3^{(NN)} \end{bmatrix}. \tag{5.24}$$

The inverse of $\mathbf{Z}$ then can be obtained as

$$\mathbf{Z}^{-1} = \mathbf{\Lambda}_3 \begin{bmatrix} \mathbf{I} & -\mathbf{Z}_3^{(LN)} \\ \mathbf{0} & \mathbf{I} \end{bmatrix} \begin{bmatrix} \mathbf{I} & \mathbf{0} \\ \mathbf{0} & \left(\mathbf{Z}_3^{(NN)}\right)^{-1} \end{bmatrix} \mathbf{P}_3^H. \tag{5.25}$$

$\left(\mathbf{Z}_3^{(NN)}\right)^{-1}$ can be represented similarly using a NL-LOGOS factorization at a coarser level. The error control of the NL-LOGOS factorization depends on the strict orthogonality between $\mathbf{\Lambda}_l^{(L)}$ and $\mathbf{\Lambda}_l^{(N)}$. Such orthogonality is difficult to achieve when OL-LOGOS factorization is used.

It can be seen from Figure 5.6(b) [5] that the NL-LOGOS source modes are confined to the same groups to which their radiated fields are localized. The OL-LOGOS are obtained by allowing the support of the source modes to spread into neighboring groups without changing the fact that the support of the (localized) radiated field is confined to a single group at a given level. This group is referred to as the "index group" of the source modes in the following discussion. For the same strip example, in the OL-LOGOS factorization, a sparse, square matrix, $\mathbf{\Lambda}_3 = \left[\mathbf{\Lambda}_3^{(L)} \mathbf{\Lambda}_3^{(N)}\right]$, indicates the overlapped

source modes at level-3 and its structure is shown in Figure 5.6(c) [5]. It can be seen the support of the source modes includes not just the index group but also all touching neighbors. Note also that, the matrix blocks $\mathbf{\Lambda}_3^{(N)}$, and $\mathbf{Z}_3\mathbf{\Lambda}_3^{(L)}$ for both NL-LOGOS and OL-LOGOS factorizations have the same non-overlapped configuration, which is required to facilitate the multilevel factorization. The OL-LOGOS modes are nonzero over an expanded domain. Therefore they cover all group boundaries at every level of the oct-tree. This strategy allows more DOFs to be included in the analysis, hence more localized modes to be found at finer levels of the tree. Consequently, coarser level factorizations are left with smaller matrices. However, the OL-LOGOS factorization just described above has been observed to suffer from significant overhead and poor error control in some cases. A new procedure has been presented in [5] that overcomes these limitations by using a so-called shifted-grid to define the overlapping LOGOS modes. Instead of covering all seams in the oct-tree at every level, the localizing functions used in the resulting factorization cover all tree seams after every four levels. It is observed that the resulting OL-LOGOS factorization provides both good error control and efficiency.

The OL-LOGOS factorization described in [5] requires shifted oct-tree groups at every level in addition to the original tree groups. The details of it can be found in the reference [5].

Figure 5.7 [5] shows the flow chart of the full OL-LOGOS factorization. Since the system matrix obtained from IE methods is usually dense, it is efficient to represent it by compression method. We use the multilevel simply sparse method (MLSSM) [32, 33], to prepare the system matrix, which is indicated in the first step in Figure 5.7 [5].

The structure of the MLSSM representation is written as the multilevel recursion formula,

$$\mathbf{Z}_l = \hat{\mathbf{Z}}_l + \mathbf{U}_l \mathbf{Z}_{l-1} \mathbf{V}_l^H, \quad \left(l = 2, \ldots, L\right), \tag{5.26}$$

where, $\hat{\mathbf{Z}}_l$ is the sparse matrix that contains all near-neighbor interactions at level $-l$ that were not represented at finer level of the tree. The matrices $\mathbf{U}_l$ and $\mathbf{V}_l$ are rectangular, orthonormal, block diagonal matrices that compress interactions between sources in far groups at level $-l$ of the tree. The original impedance matrix is obtained from (5.26) when $l = L$. The recursion procedure proceeds to level -2, since all interactions at level -2 are between near-neighbor groups. The details of the MLSSM method can be found in [32, 33]. For the following discussions we will focus on the OL-LOGOS procedure indicated on the right side of the flow chart. We again use the PEC strip shown in Figure 5.6 to illustrate this factorization procedure.

In step O-1, the normal NL-LOGOS factorization is used to reduce the computational load of computing the OL-LOGOS factorization. The result of the NL-LOGOS factorization can be obtained by combing (5.23) and (5.24),

$$\mathbf{Z}_3 \approx \mathbf{P}_3 \begin{bmatrix} \mathbf{I} & \mathbf{Z}_3^{(LN)} \\ \mathbf{0} & \mathbf{Z}_3^{(NN)} \end{bmatrix} \mathbf{\Lambda}_3^{-1}. \tag{5.27}$$

The second step, O-2, is finding the intermediate modes, the purpose of that is also to reduce the computational load of directly finding the OL-LOGOS mode. The intermediate modes are localized in the index group but radiate to the fields consist of both the index group and its touching neighbors. The intermediate modes are found by analyzing the matrix block, $\mathbf{Z}_3^{(NN)}$ of (5.27), which is partitioned according to level -3

groups. Let $\mathbf{\Lambda}_3^{(I)}$ be the matrix formed by the intermediate localizing modes, then the corresponding field $\mathbf{P}_3^{(I)}$ can be obtained by

$$\mathbf{P}_3^{(I)} \approx \mathbf{Z}_3^{(NN)} \mathbf{\Lambda}_3^{(I)}. \tag{5.28}$$

$\mathbf{\Lambda}_3^{(I)}$ has a block diagonal configuration, while $\mathbf{P}_3^{(I)}$ has the same block overlapping configuration as $\mathbf{\Lambda}_3^{(L)}$ in Figure 5.6(c) [5].

The third step, O-3, calculates the OL-LOGOS modes within the localized intermediate modes, $\mathbf{\Lambda}_3^{(I)}$, thus only $\mathbf{P}_3^{(I)}$ is analyzed. Now a shifted grid [5] is used. The nonzero support of the level-3 source modes is defined by the extent of the level-2 shifted groups. Therefore, the matrix blocks $\mathbf{P}_{1(3)}^{(I)}$, $\left[\mathbf{P}_{2(3)}^{(I)}, \mathbf{P}_{3(3)}^{(I)}\right]$ and $\mathbf{P}_{4(3)}^{(I)}$ are individually analyzed to find the OL-LOGOS modes to form $\tilde{\mathbf{\Lambda}}_3^{(L)}$ that denotes the localizing OL-LOGOS modes of all groups at level-3. (Note also that, the subscript $i(l)$ denotes group i at level $-l$, whereas a single subscript i denotes the level.)

Now take $\left[\mathbf{P}_{2(3)}^{(I)}, \mathbf{P}_{3(3)}^{(I)}\right]$ as an example. First, perform a QR factorization[34]

$$\left[\mathbf{P}_{2(3)}^{(I)}, \mathbf{P}_{3(3)}^{(I)}\right] = \mathbf{QR} = \begin{bmatrix} \mathbf{Q}_{x(3)} \\ \mathbf{Q}_{2(3)} \\ \mathbf{Q}_{3(3)} \\ \mathbf{Q}_{y(3)} \end{bmatrix} \mathbf{R}, \tag{5.29}$$

where $\mathbf{Q}_{2(3)}$ and $\mathbf{Q}_{3(3)}$ are the portions of $\mathbf{Q}$ that contain row DOFs in group 2 and 3, respectively, whereas $\mathbf{Q}_{x(3)}$ and $\mathbf{Q}_{y(3)}$ contains remaining DOFs. To find the OL-LOGOS modes radiating fields localized to group 2 of level-3, an SVD [34] is performed on the

block matrix $\mathbf{Q}_{2(3)}$ such that $\mathbf{Q}_{2(3)} = \mathbf{U}_{2(3)}\mathbf{S}_{2(3)}\mathbf{V}_{2(3)}^{H}$. The singular values $\mathbf{S}_{2(3)}$, indicate how much energy is concentrated in group 2 due to source modes $\mathbf{R}^{-1}\mathbf{V}_{2(3)}$ since

$$\left[\mathbf{P}_{2(3)}^{(I)}, \mathbf{P}_{3(3)}^{(I)}\right]\left(\mathbf{R}^{-1}\mathbf{V}_{2(3)}\right) = \mathbf{Q}\mathbf{V}_{2(3)}. \tag{5.30}$$

Since $\mathbf{Q}\mathbf{V}_{2(3)}$ is orthonormal, more energy concentrated in group 2 that means less energy is received by other parts. Once the appropriate cut-off threshold in $\mathbf{S}_{2(3)}$ is determined, the localizing modes to group 2 are given by $\tilde{\mathbf{\Lambda}}_{2(3)}^{(L)} = \mathbf{R}^{-1}\mathbf{V}_{2(3)}^{(L)}$, where $\mathbf{V}_{2(3)}^{(L)}$ contains the portion of the right singular vectors of $\mathbf{Q}_{2(3)}$ corresponding to the large (near unity) singular values that are retained.

Repeat the QR-SVD procedure described above for all the other groups at level 3. Once $\tilde{\mathbf{\Lambda}}_{3}^{(L)}$ is obtained, the final localizing OL-LOGOS modes at level-3 are given by

$$\overline{\mathbf{\Lambda}}_{3}^{(L)} = \mathbf{\Lambda}_{3}^{(I)}\tilde{\mathbf{\Lambda}}_{3}^{(L)}, \tag{5.31}$$

which has the configuration indicated by Figure 5.6(d).[5] The corresponding radiated fields by these modes are given by

$$\overline{\mathbf{E}}_{3}^{(L)} \approx \mathbf{Z}_{3}^{(NN)}\overline{\mathbf{\Lambda}}_{3}^{(L)} = \mathbf{Z}_{3}^{(NN)}\mathbf{\Lambda}_{3}^{(I)}\tilde{\mathbf{\Lambda}}_{3}^{(L)} = \mathbf{P}_{3}^{(I)}\tilde{\mathbf{\Lambda}}_{3}^{(L)}. \tag{5.32}$$

Then by QR factorization, the projection matrices, $\overline{\mathbf{P}}_{3}^{(L)}$ and $\overline{\mathbf{P}}_{3}^{(N)}$ can be found as

$$\overline{\mathbf{E}}_{3}^{(L)} = \mathbf{Q}\mathbf{R} = \left[\overline{\mathbf{P}}_{3}^{(L)} \quad \overline{\mathbf{P}}_{3}^{(N)}\right]\begin{bmatrix}\mathbf{R}^{(L)} \\ \mathbf{0}\end{bmatrix}. \tag{5.33}$$

To enable the multilevel factorization, the non-localizing modes, $\overline{\mathbf{\Lambda}}_{3}^{(N)}$, must be block diagonal. Ideally, they should also be orthogonal to matrix $\overline{\mathbf{\Lambda}}_{3}^{(L)}$. It cannot be achieved in most cases due to the overlapping nature of $\overline{\mathbf{\Lambda}}_{3}^{(L)}$. Thus the contribution to $\overline{\mathbf{\Lambda}}_{3}^{(N)}$ for a

given level-3 group is set to be the orthogonal complement of the corresponding section of $\overline{\mathbf{\Lambda}}_3^{(L)}$.

With the OL-LOGOS modes defined above, the OL-LOGOS factorization for level-3 can be given by

$$\mathbf{Z}_3^{(NN)} \approx \overline{\mathbf{P}}_3 \begin{bmatrix} \mathbf{I} & \overline{\mathbf{Z}}_3^{(LN)} \\ \mathbf{0} & \overline{\mathbf{Z}}_3^{(NN)} \end{bmatrix} \overline{\mathbf{\Lambda}}_3^{-1}. \tag{5.34}$$

Combining (5.27) and (5.34), the factorization at level-3 is expressed as

$$\mathbf{Z}_3 \approx \mathbf{P}_3 \begin{bmatrix} \mathbf{I} & \mathbf{Z}_3^{(LN)} \\ \mathbf{0} & \overline{\mathbf{P}}_3 \begin{bmatrix} \mathbf{I} & \overline{\mathbf{Z}}_3^{(LN)} \\ \mathbf{0} & \overline{\mathbf{Z}}_3^{(NN)} \end{bmatrix} \overline{\mathbf{\Lambda}}_3^{-1} \end{bmatrix} \mathbf{\Lambda}_3^{-1}, \tag{5.35}$$

where the over-bar notation indicates that factorization is carried on the shifted grid. A multilevel factorization for the square system $\mathbf{Z}$ is obtained by repeating the single-level factorization indicated by (5.35) for the sequence of square matrices $\overline{\mathbf{Z}}_l^{NN}$. At each level this yields an equation with the form indicated by (5.27), (5.34) and (5.35)

$$\begin{aligned} \overline{\mathbf{Z}}_{l+1}^{(NN)} &\approx \mathbf{P}_l \begin{bmatrix} \mathbf{I} & \mathbf{Z}_l^{(LN)} \\ \mathbf{0} & \mathbf{Z}_l^{(NN)} \end{bmatrix} \mathbf{\Lambda}_l^{-1} \\ &\approx \mathbf{P}_l \begin{bmatrix} \mathbf{I} & \mathbf{Z}_l^{(LN)} \\ \mathbf{0} & \overline{\mathbf{P}}_l \begin{bmatrix} \mathbf{I} & \overline{\mathbf{Z}}_l^{(LN)} \\ \mathbf{0} & \overline{\mathbf{Z}}_l^{(NN)} \end{bmatrix} \overline{\mathbf{\Lambda}}_l^{-1} \end{bmatrix} \mathbf{\Lambda}_l^{-1}, \end{aligned} \tag{5.36}$$

where $\overline{\mathbf{Z}}_{l+1}^{(NN)} \equiv \mathbf{Z}_l$. Indicated by Figure 5.7 [5], this OL-LOGOS factorization procedure is carried out from the finest level to level-3. At level-2 the NL-LOGOS factorization indicated by the first line of (5.36) is used.

5.2.3. The modification to the over-determined system

In this section, the OL-LOGOS factorization [5] described above is extended to handle over-determined systems. The charge neutrality constraint can be added to the existing AEFIE or AEFIE-G matrix [19], yielding an over-determined system matrix (more rows than columns). In particular, the additional row is carried along as an additional constraint, which is imposed at each step of the factorization. The corresponding modification of (5.36) is written as

$$\begin{aligned}\begin{bmatrix}\overline{\mathbf{Z}}_{l+1}^{(NN)}\\ \overline{\mathbf{Z}}_{n,l+1}^{(N)}\end{bmatrix} &\approx \begin{bmatrix}\mathbf{P}_l & \mathbf{0}\\ \mathbf{0} & 1\end{bmatrix}\begin{bmatrix}\mathbf{I} & \mathbf{Z}_l^{(LN)}\\ \mathbf{0} & \mathbf{Z}_l^{(NN)}\\ \mathbf{0} & \mathbf{Z}_{n,l}^{(N)}\end{bmatrix}\boldsymbol{\Lambda}_l^{-1}\\ &\approx \begin{bmatrix}\mathbf{P}_l & \mathbf{0}\\ \mathbf{0} & 1\end{bmatrix}\begin{bmatrix}\mathbf{I} & \mathbf{Z}_l^{(LN)}\\ \mathbf{0} & \begin{bmatrix}\overline{\mathbf{P}}_l & \mathbf{0}\\ \mathbf{0} & 1\end{bmatrix}\begin{bmatrix}\mathbf{I} & \overline{\mathbf{Z}}_l^{(LN)}\\ \mathbf{0} & \overline{\mathbf{Z}}_l^{(NN)}\\ \mathbf{0} & \overline{\mathbf{Z}}_{n,l}^{(N)}\end{bmatrix}\overline{\boldsymbol{\Lambda}}_l^{-1}\end{bmatrix}\boldsymbol{\Lambda}_l^{-1},\end{aligned} \tag{5.37}$$

where $\overline{\mathbf{Z}}_{n,l}^{(N)}$ indicate the additional charge neutrality row at the each step of the factorization.

5.3 Numerical Examples

5.3.1 Frequency and mesh stability

In this section, we will demonstrate that the AEFIE-G formulation is stable with respect to both frequency and mesh refinement [19].

As the first example, a PEC sphere with radius 0.5 m is tested to evaluate the frequency behavior of the AEFIE-G formulation. Figure 5.8 shows the condition number of the system matrix obtained from the AEIFE-G and the conventional EFIE versus frequency for a fixed mesh. It is observed that the condition number of AEFIE-G is

almost constant over the whole low frequency spectrum whereas the condition number of the conventional EFIE increases sharply as the frequency decreases, and it breaks down around 1 MHz. Note also that, the condition number of the EFIE appears to flatten near 0.1 MHz, which is due to numerical precision issues. This clearly demonstrates that the AEFIE-G formulation provides a frequency stable system matrix, which is free of the low-frequency breakdown problem inherent in the conventional EFIE.

Next, mesh refinement of a $1m \times 1m$ plate is studied at the frequency of 1 Hz. The mesh is discretized using a uniform distribution of square patches. Figure 5.9 shows that the original AEFIE-G is instable with mesh refinement and has relatively large condition number. With appropriate scaling in terms of patch area and edge length, the scaled AEFIE-G is stable with mesh refinement and has a much smaller condition number.

5.3.2 Computational cost and error

To evaluate the computational cost and the error of the OL-LOGOS factorization applied on the over-determined AEFIE-G system matrix, a PEC sphere with radius 1 m is tested with mesh refinement with the 1 Hz incident plane wave [19].

Figure 5.10 shows the factorization time for different factorization tolerances, ε_{fac}. An $O(N)$ factorization time complexity is observed for both tolerances 0.005 and 0.001. For tolerance 0.0001, the factorization time complexity is between $O(N)$ and $O(N \log N)$. Figure 5.11 shows the $O(N)$ memory usage for these three tolerances.

Figure 5.12 shows the residual error of the solution. It demonstrates that OL-LOGOS provides an error-controlled solution for AEFIE-G over several orders of magnitude for tolerance 0.001 and 0.0001. Figure 5.13 shows the relative Root-Mean-

Square (RMS) error of the near electric field as compared with the Mie series solution. The RMS error is calculated as

$$\varepsilon_{RMS} = \left\| E_{\theta}^{s} - E_{\theta(Mie)}^{s} \right\|_2 \Big/ \left\| E_{\theta(Mie)}^{s} \right\|_2 , \tag{5.38}$$

where E_{θ}^{s} is the near electric field scattering from a PEC sphere with radius 1 m and frequency 1 Hz for vertical polarization at distance 0.5 m above the PEC surface, and $E_{\theta(Mie)}^{s}$ is the corresponding Mie series solution. It can be seen that with mesh refinement, the near field obtained by AEFIE-G converges to the Mie series solution.

Figure 5.14 shows the DOF remaining at the root level. It shows that the number of DOF remains at the root level scales as $O\left(N^{0.33}\right)$. Since the OL-LOGOS factorization is formulation sensitive, strong singular kernels, such the EFIE, are more difficult to localize. Figure 5.14 demonstrates that the AEFIE-G formulation is a good candidate for the OL-LOGOS factorization, since it is well conditioned and stable with frequency and mesh refinement.

5.4 Summary

The local-global solution concept provides a useful framework for developing fast, direct solution methods for EM simulation. The AEFIE and AEFIE-G formulation are demonstrated to be frequency and mesh stable. The OL-LOGOS algorithm provides good asymptotic performance and error control when used with AEFIE-G. However, the drawback of the AEFIE/AEFIE-G is that it cannot provide correct near magnetic field at low frequency, which might be corrected by using a perturbative strategy reported in [30], this possibility is not investigated here.

Table 5.1 The condition number of system matrix before and after scaling

Mesh	AEFIE		AEFIE-G	
	Before	After	Before	After
3x3	2014	246	937	120
9x9	23135	751	23135	607
16x16	127070	4478	127070	2140

Table 5.2 The condition number of the square and the over-determined AEFIE system matrix

Mesh	square AEFIE matrix	Over-determined AEFIE matrix
9x9	751	282
16x16	4478	952
20x20	9009	1480

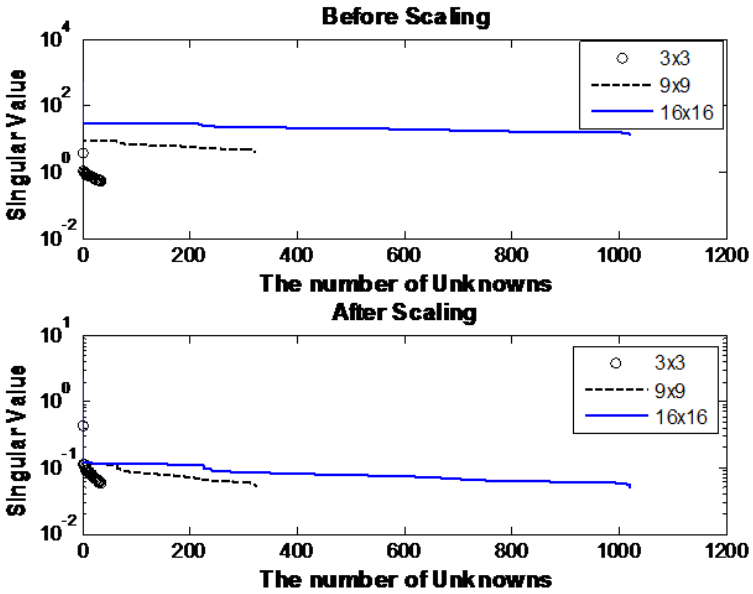

Figure 5.1 The singular value study with mesh refinement

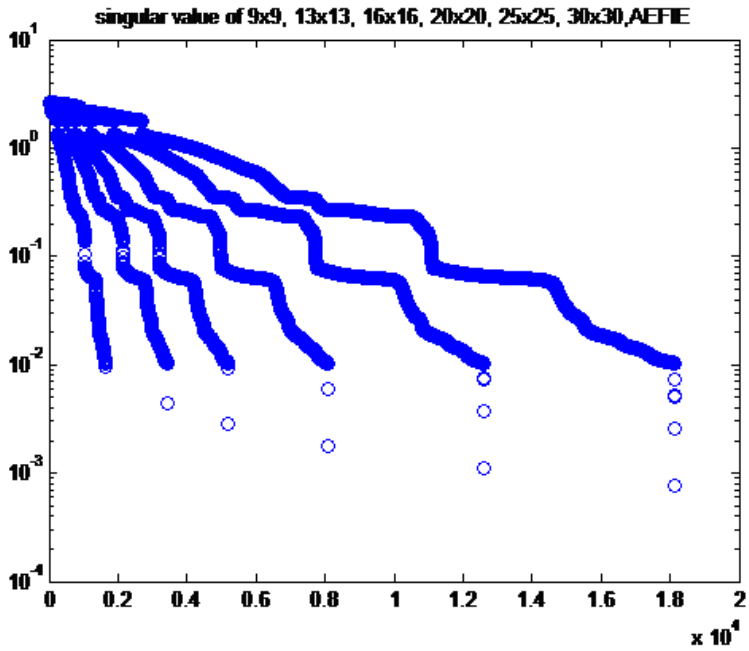

Figure 5.2 Singular value distributions of AEFIE with usual sacling

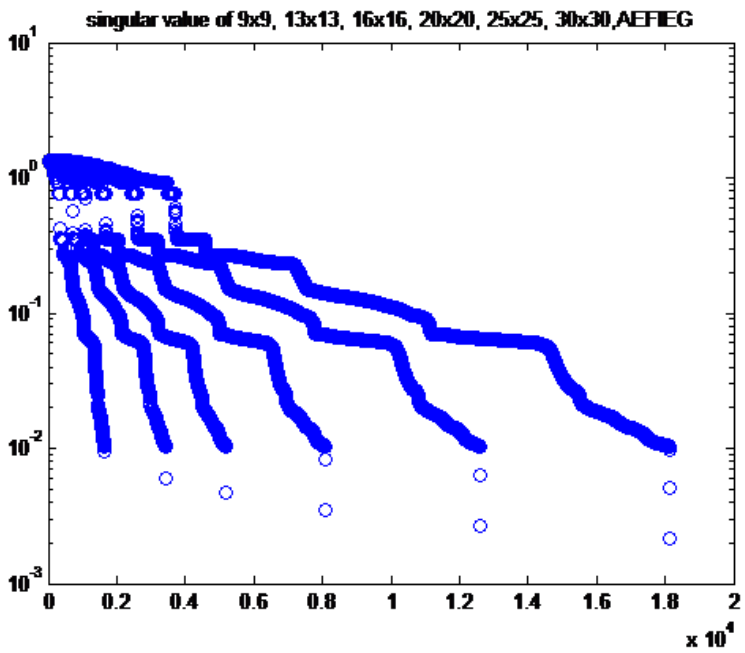

Figure 5.3 Singular value distributions of AEFIE-G with usual scaling

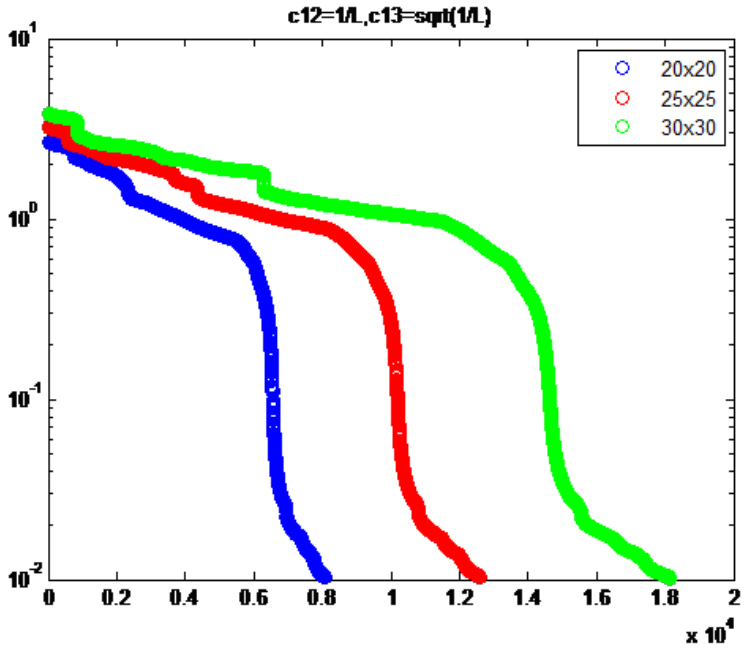

Figure 5.4 Singular value distribution of AEFIE with further scaling

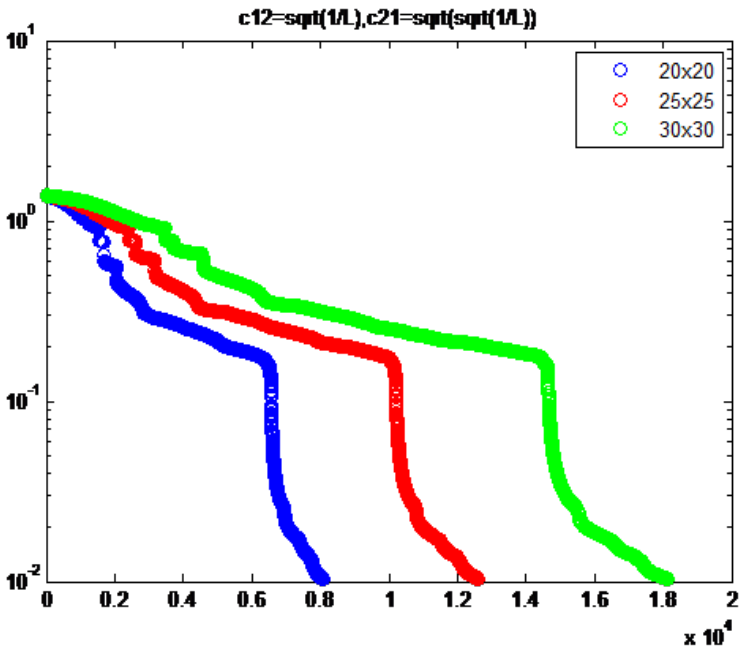

Figure 5.5 Singular value distribution of AEFIE-G with further scaling

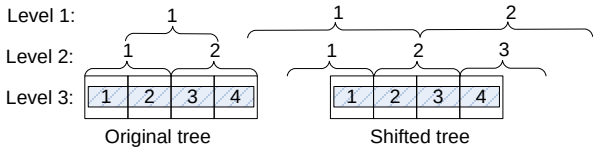

(a)

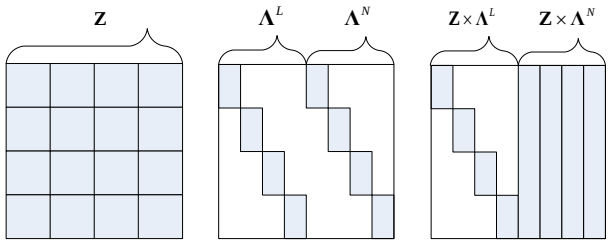

(b)

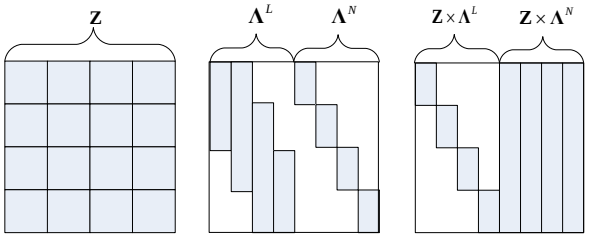

(c)

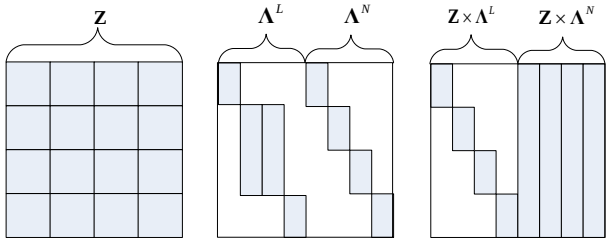

(d)

Figure 5.6 Structure of matrices of NL-LOGOS and OL-LOGOS source modes and their fields for a patch decomposed into 4 groups. (a) Patch decomposed into 4 groups. (b) $\mathbf{Z}$, $\mathbf{\Lambda}$ and $\mathbf{Z}\times\mathbf{\Lambda}$ for NL-LOGOS factorization. (c) $\mathbf{Z}$, $\mathbf{\Lambda}$ and $\mathbf{Z}\times\mathbf{\Lambda}$ for OL-LOGOS factorization. (d) $\mathbf{Z}$, $\mathbf{\Lambda}$ and $\mathbf{Z}\times\mathbf{\Lambda}$ OL-LOGOS factorization with shifted grid.

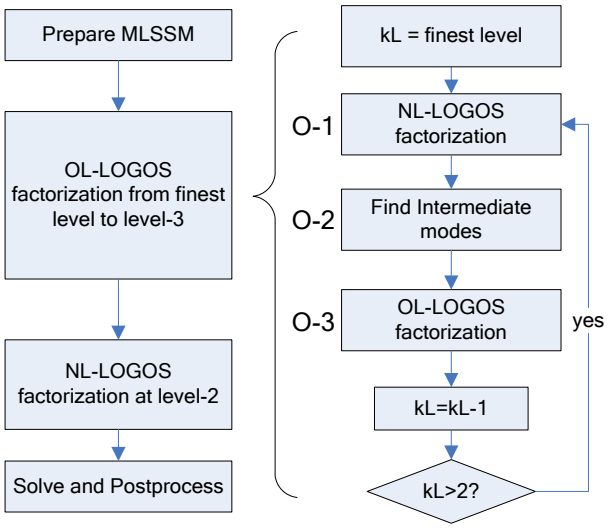

Figure 5.7 Flowchart for the OL-LOGOS factorization.

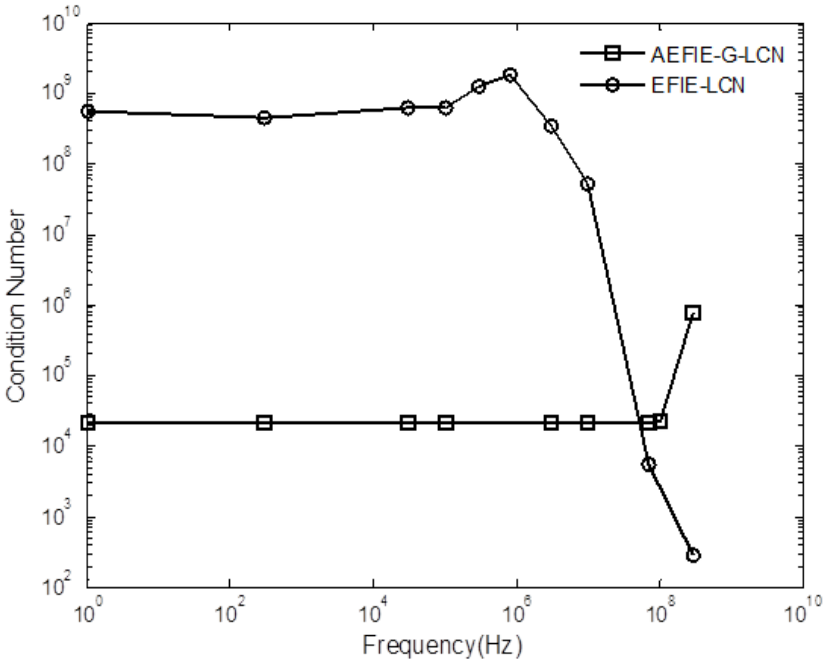

Figure 5.8 Condition numbers versus frequency for EFIE, AEFIE system matrices of a 0.5-m PEC sphere.

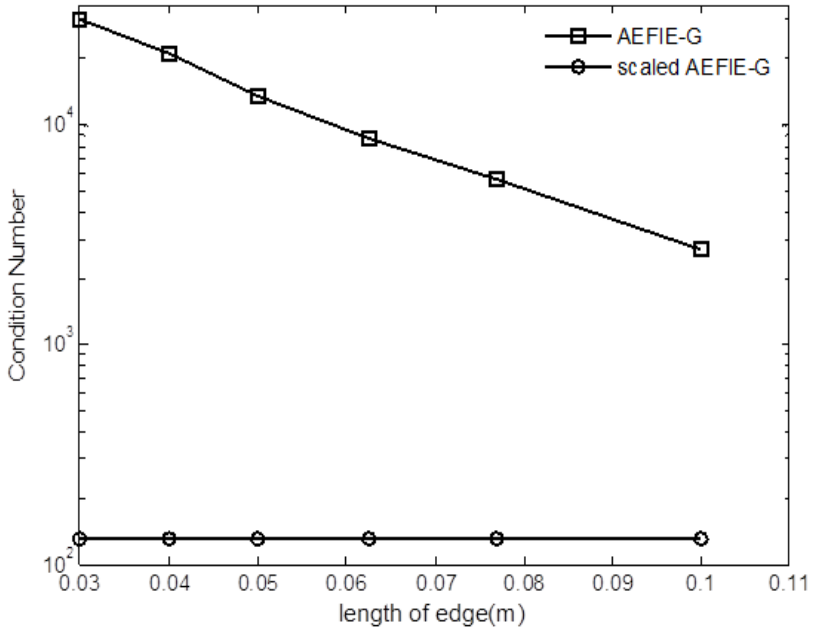

Figure 5.9 Condition numbers versus mesh refinement for AEFIE-G and scaled AEFIE-G matrices of 1-m PEC plate.

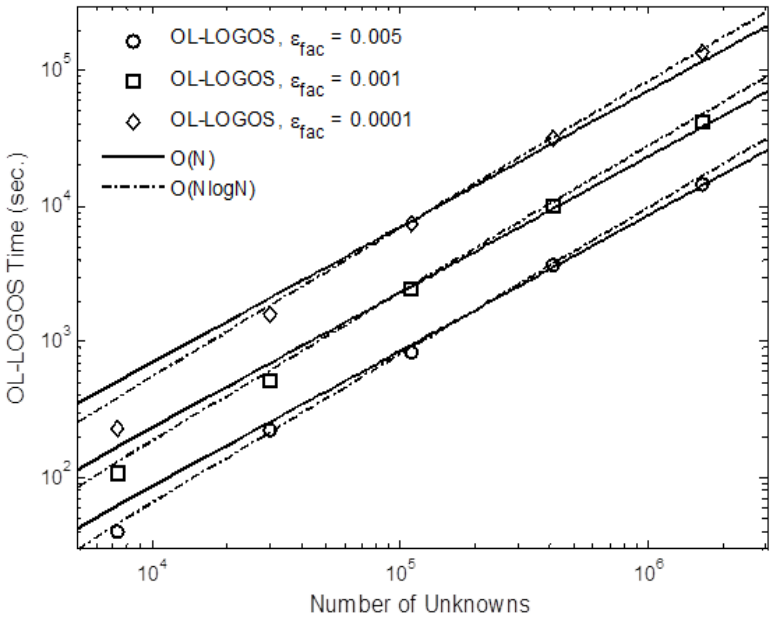

Figure 5.10 OL-LOGOS factorization time for the AEFIE-G formulation of a 1-m PEC sphere for 1 Hz plane wave excitation. Number of DOF increases via uniform mesh refinement.

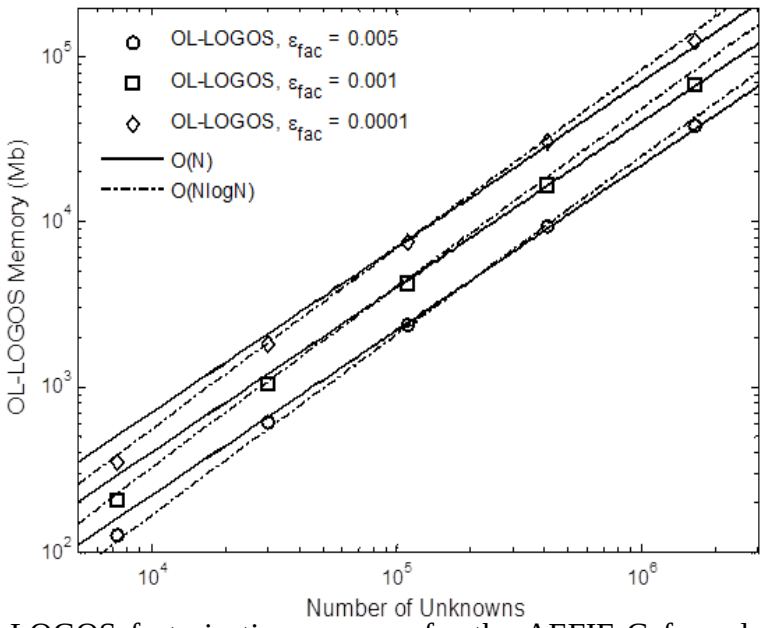

Figure 5.11 OL-LOGOS factorization memory for the AEFIE-G formulation of a 1-m PEC sphere for 1 Hz plane wave excitation. Number of DOF increases via uniform mesh refinement.

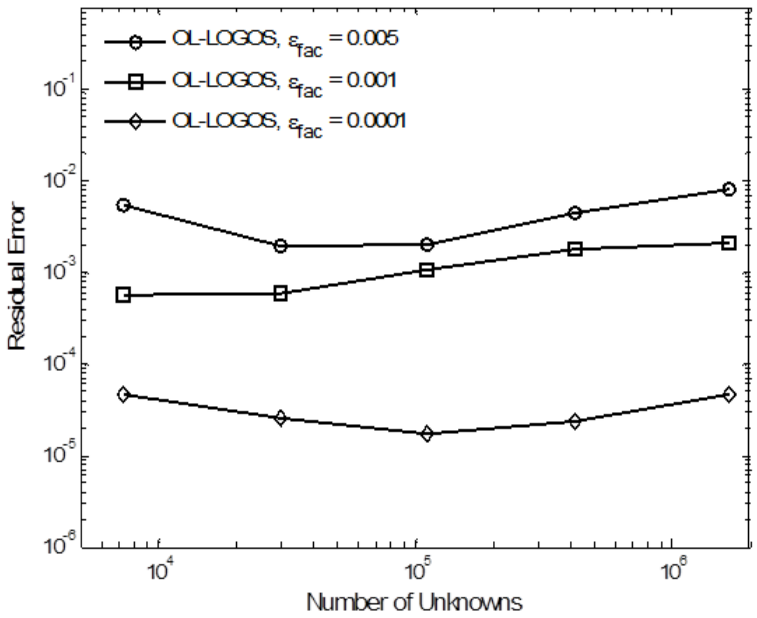

Figure 5.12 Residual error of OL-LOGOS factorization for the AEFIE-G formulation of a 1-m PEC sphere for 1 Hz plane wave excitation. Number of DOF increases via uniform mesh refinement.

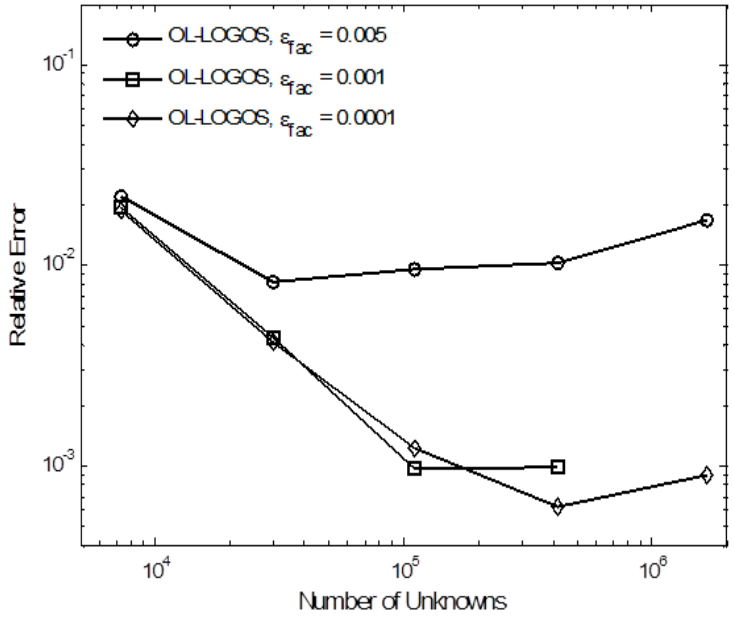

Figure 5.13 RMS Near-Field error of OL-LOGOS factorization for the AEFIE-G formulation of a 1-m PEC sphere for 1 Hz plane wave excitation. Number of DOF increases via uniform mesh refinement. The near electric fields are sampled 0.5 m above the PEC surface.

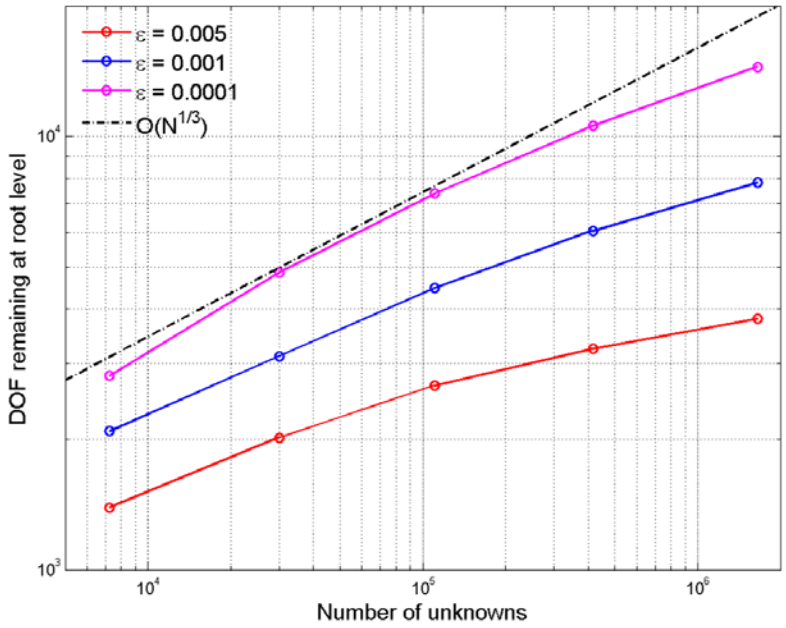

Figure 5.14 DOF remaining at root level of OL-LOGOS factorization for the AEFIE-G formulation of a 1-m PEC sphere for 1 Hz plane wave excitation. Number of DOF increases via uniform mesh refinement.

Chapter 6 Conclusions and Future Work

6.1 Conclusions

A new electric field integral equation (EFIE) based formulation that relies on the Helmholtz decomposition (HD) (EFIE-hd) of the current is proposed and developed. It has been demonstrated that the EFIE-hd is frequency stable and provides accurate solutions for the electric and magnetic fields at both high and low frequencies. It is also shown that this strategy allows for the use of the locally corrected Nyström (LCN) method for the resulting formulation. To the best of our knowledge, the EFIE-hd represents the first formulation of electromagnetic scattering from a PEC obstacle that provides accurate solutions for both the electric and magnetic fields without relying on either global basis functions or global stabilizing operators. For this reason, the EFIE-hd is compatible with both an LCN discretization and the OL-LOGOS factorization method.

While the ultimate goal of the efforts that is supporting this work lie in developing a sparse, direct solution of the EFIE-hd formulation, that goal is beyond the scope of this dissertation. We have instead used the AEFIE formulation to investigate the significance of using a well-conditioned formulation with the OL-LOGOS algorithm. The AEFIE-G is observed to be frequency and mesh stable, with the AEFIE-G exhibiting better conditioning than the AEFIE. It was observed that the overlapped localizing LOGOS (OL-LOGOS) factorization provides nearly optimal computational complexity when applied to this formulation.

6.2 New Contributions

The new work presented in this dissertation includes the following:

- A new electric field integral equation (EFIE) based formulation that relies on the Helmholtz decomposition (HD) (EFIE-hd) of the current is proposed and developed. It has been demonstrated that the EFIE-hd is frequency stable and provides accurate solutions for the electric and magnetic fields at both high and low frequencies.
- The well-conditioned augmented EFIE-G (AEFIE-G) formulation with appropriate diagonal scaling using the LCN method is developed. It is observed to be frequency and mesh stable and can provide correct electric filed at both high and low frequencies.
- The OL-LOGOS algorithm is first extended to factorize the over-determined system matrix (i.e., AEFIE/AEFIE-G). It is observed that the OL-LOGOS factorization provides nearly optimal computational complexity when applied to AEFIE-G system matrix.

6.3 Future Work

There are several areas for additional work related to the new EFIE-hd formulation. These include the possibility of modifying the formulation to obtain a square system matrix rather than the over-determined system used herein. Another issue is the possibility of using the EFIE-hd to treat non-conformal meshes at any frequency. Both of these issues are currently under investigation and some progress has been made in both directions.

The second issue is associated with the discretization. In the current work, it has been observed that when polynomial complete bases are used for rotational current and mixed-order bases are used for irrotational current, a well-conditioned system and an

accurate solution can be obtained. However, a theoretical justification is still on the way, which will serve as the guideline on how to select appropriate discretization.

Though the EFIE-hd system is frequency stable, the version presented herein is still not stable with respect to mesh refinement. This is due to the presence of the hypersingular kernel. It is expected that this can be addressed by including continuity equations and to introduce charge as an additional unknown.

The globally constrained HD is also expected to be useful when applied to the magnetic field integral equation (MFIE) to improve its accuracy when sharp corners are considered. It is similarly expected that the HD framework will be extensible to surface integral equation formulations of electromagnetic scattering from dielectric materials.

Finally, all of these developments on the EFIE-hd are being pursued with the intention of eventually solving large system using the OL-LOGOS factorization algorithm. Due to the structure of the EFIE-hd formulation, this is expected to be straightforward; the EFIE-hd was developed with this integration of the methods in mind.

References

[1] J. R. Mautz and R. F. Harrington, "An E-field solution for a conducting surface small or comparable to the wavelength," *IEEE Transactions on Antennas and Propagation,* vol. 32, pp. 330-339, 1984.

[2] J. M. Rius, E. Ubeda, and J. Parron, "On the testing of the magnetic field integral equation with RWG basis functions in method of moments," *IEEE Transactions on Antennas and Propagation,* vol. 49, pp. 1550-1553, 2001.

[3] A. F. Peterson, S. L. Ray, and R. Mittra, *Computational Methods for Electromagnetics*. Piscataway, NJ: IEEE Press, 1998.

[4] R. J. Adams, Y. Xu, X. Xu, J. S. Choi, S. D. Gedney, and F. X. Canning, "Modular fast direct electromagnetic analysis using local-global solution modes," *Ieee Transactions on Antennas and Propagation,* vol. 56, pp. 2427-2441, Aug 2008.

[5] X. Xu and R. J. Adams, "Sparse Matrix Factorization Using Overlapped Localizing LOGOS Modes on a Shifted Grid," *Ieee Transactions on Antennas and Propagation,* vol. 60, pp. 1414-1424, Mar 2012.

[6] S. D. Gedney, "On Deriving a Locally Corrected Nyström Scheme from a Quadrature Sampled Moment Method," *IEEE Transactions on Antennas and Propagation,* vol. 51, pp. 2402-2412, September 2003.

[7] L. F. Canino, J. J. Ottusch, M. A. Stalzer, J. L. Visher, and S. M. Wandzura, "Numerical solution of the Helmholtz equation in 2D and 3D using a high-order Nyström discretization," *Journal of Computational Physics,* vol. 146, pp. 627-663, Nov 1 1998.

[8] S. D. Gedney, A. M. Zhu, and C. C. Lu, "Study of mixed-order basis functions for the locally corrected Nyström method," *IEEE Transactions on Antennas and Propagation,* vol. 52, pp. 2996-3004, Nov 2004.

[9] A. F. Peterson and M. M. Bibby. (2010). *An introduction to the locally-corrected Nyström method*. Morgan & Claypool Publishers, 2010.

[10] J. S. Zhao and W. C. Chew, "Integral equation solution of Maxwell's equations from zero frequency to microwave frequencies," *IEEE Transactions on Antennas and Propagation,* vol. 48, pp. 1635-1645, Oct 2000.

[11] G. Vecchi, "Loop-star decomposition of basis functions in the discretization of the EFIE," *IEEE Transactions on Antennas and Propagation,* vol. 47, pp. 339-346, Feb 1999.

[12] H. Contopanagos, B. Dembart, M. Epton, J. J. Ottusch, V. Rokhlin, J. L. Visher, *et al.*, "Well-conditioned boundary integral equations for three-dimensional electromagnetic scattering," *IEEE Transactions on Antennas and Propagation,* vol. 50, pp. 1824-1830, Dec 2002.

[13] R. J. Adams, "Physical and analytical properties of a stabilized electric field integral equation," *IEEE Transactions on Antennas and Propagation,* vol. 52, pp. 362-372, Feb 2004.

[14] F. P. Andriulli, K. Cools, H. Bagci, F. Olyslager, A. Buffa, S. Christiansen, *et al.*, "A multiplicative Calderon preconditioner for the electric field integral equation," *IEEE Transactions on Antennas and Propagation,* vol. 56, pp. 2398-2412, Aug 2008.

[15] D. Gope, A. Ruehli, and V. Jandhyala, "Solving low-frequency EM-CKT problems using the PEEC method," *IEEE Transactions on Advanced Packaging,* vol. 30, pp. 313-320, May 2007.
[16] Z. G. Qian and W. C. Chew, "An augmented electric field integral equation for highspeed interconnect analysis," *Microwave and Optical Technology Letters,* vol. 50, pp. 2658-2662, Oct 2008.
[17] M. Taskinen and P. Yla-Oijala, "Current and charge integral equation formulation," *IEEE Transactions on Antennas and Propagation,* vol. 54, pp. 58-67, Jan 2006.
[18] J. C. Young, Y. Xu, R. J. Adams, and S. D. Gedney, "High-order Nyström implementation of an agumented electric field integral equation," *IEEE Antennas and Wireless Propagation Letters,* vol. 11, pp. 846-849, 2012.
[19] J. Cheng and R. J. Adams, "Direct solution method using overlapped localizing LOGOS modes for AEFIE-G at low frequencies," presented at the *28th International Review of Progress in Applied Computational Electromagnetics*, Columbus, OH, 2012.
[20] R. Coifman, V. Rokhlin, and S. Wandzura, "The Fast Multipole Method: A Pedestrian Prescription," *IEEE Antennas and Propagation Magazine,* vol. 35, pp. 7-12, June 1993.
[21] S. M. Rao, D. R. Wilton, and A. W. Glisson, "Electrogmagnetic Scattering by Surfaces of Arbitrary Shape," *IEEE Transactions on Antennas and Propagation,* vol. 30, pp. 409-418, May 1982.
[22] J. Strain, "Locally-corrected multidimensional quadrature rules for singular functions," *SIAM J. Sci. Comput.,* vol. 16, pp. 992-1017, 1995.
[23] S. D. Gedney, "High-order method-of-moments solution of the scattering by three-dimensional PEC bodies using quadrature-based point matching," *Microwave and Optical Technology Letters,* vol. 29, pp. 303-309, Jun 5 2001.
[24] J. A. Stratton, *Electromagnetic theory,* 1st ed. New York, London,: McGraw-Hill book company, inc., 1941.
[25] F. Çaliskan and A. F. Peterson, "The need for mixed-order representations with the locally corrected Nystrom method," *IEEE Antennas and Wireless Propagation Letters,* vol. 2, pp. 72- 73, 2003.
[26] J. Jin, *The Finite Element Method in Electromagnetics* Second ed. New York: Wiley, 2002.
[27] C. A. Balanis, *Advanced Engineering Electromagnetics,* 2nd ed. Hoboken, N.J.: John Wiley & Sons, 2012.
[28] M. G. Duffy, "Quadrature over a pyramid or cube of integrands with a singularity at a vertex," *Siam Journal on Numerical Analysis,* vol. 19, pp. 1260-1262, 1982.
[29] G. C. Hsiao and R. E. Kleinman, "Mathematical foundations for error estimation in numerical solutions of integral equations in electromagnetics," *IEEE Transactions on Antennas and Propagation,* vol. 45, pp. 316-328, Mar 1997.
[30] Z. G. Qian and W. C. Chew, "Enhanced A-EFIE With Perturbation Method," *IEEE Transactions on Antennas and Propagation,* vol. 58, pp. 3256-3264, Oct 2010.

[31] X. Xu, Y. Xu, and R. J. Adams, "Error Analysis for Matrix Factorizations using Non-overlapped Localizing Basis Functions," *IEEE transactions on Antennas and Propagation*, vol. 58, pp. 3081-3086, 2010.
[32] J. Cheng, S. A. Maloney, R. J. Adams, and F. X. Canning, "Efficient Fill of a Nested Representation of the EFIE at Low Frequencies," presented at the IEEE AP-S International Symposium, San Diego, CA, 2008.
[33] X. Xu, "Modular Fast Direct Analysis Using Non-Radiating Local-Global Solution Modes," PHD Dissertation, Electrical and Computer Engineering, University of Kentucky, 2009.
[34] G. H. Golub and C. F. Van Loan, *Matrix Computations*, Third ed.: Johns Hopkins University Press, 1996.

Vita

Jin Cheng was born on January 19, 1982 in Beijing, China. She graduated from Beijing No.12 high school, Beijing in June of 2000. She received the B.S. degree in Electrical Engineering from Beijing Institute of Technology, Beijing in June of 2004. In July of 2006, she received the M.S. degree in Electrical Engineering also from Beijing Institute of Technology. Since August of 2006, she has been working as a graduate research assistant at University of Kentucky, Lexington, KY for her dissertation advisor, Dr. Robert J. Adams.